KIT SCIENTIFIC REPORTS 7563

Studies of the Charged Particle Density Distributions in Extensive Air Showers Observed with KASCADE-Grande

Gabriel Toma

KIT Scientific Publishing

Gabriel Toma

Studies of the Charged Particle Density Distributions in Extensive Air Showers Observed with KASCADE-Grande

Karlsruhe Institute of Technology
KIT SCIENTIFIC REPORTS 7563

Studies of the Charged Particle Density Distributions in Extensive Air Showers Observed with KASCADE-Grande

by
Gabriel Toma

KIT Scientific Publishing

Report-Nr. KIT-SR 7563

Impressum

Karlsruher Institut für Technologie (KIT)
KIT Scientific Publishing
Straße am Forum 2
D-76131 Karlsruhe
www.ksp.kit.edu

KIT – Universität des Landes Baden-Württemberg und nationales
Forschungszentrum in der Helmholtz-Gemeinschaft

KIT Scientific Publishing 2011
Print on Demand

ISSN 1869-9669

Studies of the Charged Particle Density Distributions in Extensive Air Showers Observed with KASCADE-Grande

Toma Gabriel

Submitted for the degree of Doctor of Philosophy
June 2010

Abstract

This work presents an investigation of the **E**xtensive **A**ir **S**hower (EAS) phenomena observed by the KASCADE-Grande experiment. The investigation aims at reconstructing various characteristic properties of extensive air showers which carry information on primary cosmic radiation and to analyze the recorded measurable quantities of the secondary cosmic radiation. The emphasis is put on inferring information on the energy spectrum of the primary cosmic radiation deduced from the lateral distributions of the energy deposits of charged particles in the KASCADE-Grande detectors. In the case of the KASCADE-Grande experiment, the charged particle density of EAS at 500 m distance from shower core, $S(500)$, had been proven by simulation studies to map the primary energy nearly independent of the primary mass. The conversion of $S(500)$ to the value of the primary energy has been derived from simulations and is used to reconstruct the primary energy spectrum of cosmic rays (in the 10^{16} - 10^{18} eV energy range). The results show that the shape of the cosmic ray spectrum in this range follows a power a law with a spectral index of γ=-3.05$\pm$0.01. The spectrum exhibits no significant structure. As compared to other methods of energy determination, which are based on the sizes of the observed EAS, the present procedure invokes explicitly the shape of the lateral distributions and is sensitive to deviations of the observed distributions from the predictions by simulations. Since the actual hadronic interaction models show such deficiencies, they prove to be a limitation of accuracy of the method. On the other hand the features may also serve as test of the hadronic interaction model.

Contents

Chapter 1

Introduction

During 1911 and 1912, when measuring the variation of the ionization of air with altitude by a series of balloon flights, the Austrian physicist Victor Hess discovered the cosmic radiation [1]. He noticed that instead of decreasing, as previously expected, the ionization was becoming stronger with the increase in altitude leading to the conclusion that some kind of radiation is bombarding the Earth from the outer space. The discovery itself was acknowledged in 1936 with the award of the Nobel Prize in Physics. In the years after discovery many cosmic ray investigations have worked out a complex picture of the cosmic ray phenomena, but in detail with many unanswered questions about the origin, the sources and the propagation of the cosmic radiation. Such investigations rely on direct observations for energies up to 10^{14} eV, or on Extensive Air Showers (EAS) [2,3] investigations for the energy range above 10^{14} eV where the cosmic radiation flux is too low for direct observations.

In the vastness of space, a great number of objects, be they supernovae, gas clouds, active galactic nuclei or other space objects act as sources of radiation emanating into space streams of high energy particles. Some of these particles begin a voyage of many light years (in the order of 10^8 light years) during which they interact with numerous gravitational and magnetic fields of other space objects. Some are gradually accelerated and can reach ultra-high energies of the order 10^{20} eV thus becoming microscopic carriers of macroscopic energies. This radiation consists mainly of high-energy protons (85%), α-particles (12.5%), heavier nuclei (1.5%) and electrons (1%), but it includes also other more exotic species of particles [4, 5]. The sum of such particles that reaches the top of the Earth's atmosphere is the primary cosmic radiation and arrives at the outskirts of the Earth's atmosphere isotropically, carrying practically no information regarding its original direction of propagation (that is on one hand due to the highly randomized position and emission direction of the sources and then on the other hand due to the randomized configuration of the accelerating fields). It is just lately and only at the highest energies that present day experiments are hoping to find a correlation between the arrival direction of particles and the positioning of some celestial objects [6].

The very high energy of the cosmic radiation triggers subsequent questions regarding its sources and mechanisms of acceleration and propagation. There are several possible models explaining the mechanisms of cosmic particles acceleration and implicitly some of the spectral features. Thus three models are presently probed:

- Stochastic acceleration models. In this kind of models, cosmic rays originate from galactic sources and gain their energy during numerous interactions, each adding a small contribution to the particle energy. The acceleration occurs as a result of a process called Fermi acceleration [7] of first order. It describes the diffusive acceleration of particles in shock waves. The particle is accelerated while repeatedly crossing the shock wave front. This means that the maximum attainable energy is limited by the shock wave life-time and it leads to an energy spectrum with a power law index of $\gamma \approx$-2 (independent of the shock wave configuration) [8]. Among possible shock waves generators are: supernova explosions, termination shock of stellar [9] or galactic [10] winds, pulsar winds [11]. Such sources can accelerate particles up to an energy of 10^{19} eV.

- Direct acceleration models. These models describes the particle acceleration as a very efficient process in which particles gain their entire energy in just a few acceleration steps (possibly just one step). The model relies on very strong magnetic and electric fields and allows also for extragalactic sources. Such sources may be jet emitting supernovae [12], active galactic nuclei (AGN) emitting relativistic jets, or polar caps of rapidly rotating pulsars [13]. This models allows for particles to be accelerated above 10^{16} eV.

- Top-down models. Finally, the top-down models [14] describe the high energies as the result of a yet undiscovered phenomenon, possibly the disintegration of an ultra-heavy particle that leads to the creation of very high energy particles. As in the previous model, this model allows particles around and above 10^{20} eV.

It is widely accepted that particles with energies up to 10^{16} eV originate in the confines of our galaxy and reach Earth diffusively after being deflected in various magnetic and electric fields (the diffuse character of the propagation causes the particles to loose the information regarding their sources). Due to leaking particles (outside our galaxy) and energy loss (by collisions, decay or ionization) a steepening of the predicted spectrum is expected, from $\gamma \approx$-2 to $\gamma \approx$-2.7.

Direct measurements of the primary cosmic radiation energy spectrum by balloon or satellite borne detectors are efficient up to primary energies of around 10^{14} eV. At higher energies however, direct observation becomes impractical due to the very low number of high energy particles. At highest energies in the primary energy spectrum, the flux of primary particles is as low as one particle per century per square kilometer. Hence other techniques have to be used for obtaining a reasonable number of recorded events in an equally reasonable amount of time. A possibility is to study the interaction of the primary cosmic radiation with the Earth's atmosphere, effectively using the atmosphere as interacting medium for a detector. The particles of the primary cosmic radiation penetrate the Earth's atmosphere to an extent depending on their nature (type) and also on their energies. At some point however, they will interact with nuclei (N,O) of the atmosphere and a first interaction will take place, producing a lot of secondary particles. Similarly, other interactions will follow and the primary particle will gradually loose all its energy during a dozen of such interactions steps producing projectiles that propagate only a fraction of the primary energy. The entire chain of interactions comprises

millions of particles which will propagate at some point downwards in the form of a cascade. The cascade is centered on and propagates along the initial direction of propagation of the primary particle, an axis referred to as shower axis. The sum of these secondary particles is the secondary cosmic radiation, in fact the radiation that is born in the Earths atmosphere under the flux of primary radiation. The cascades of particles are called Extensive Air Showers (EAS) discovered in 1938 by P. Auger, R. Maze and T. Grivet Mayer [2] and independently by W. Kohlhörster, I. Matthes and E.Weber [3].

Certain features of the cosmic ray energy spectrum give rise to even more questions. The primary energy spectrum exhibits a decreasing power law behavior (eq. 1.1) with an index γ that suddenly changes for energies higher than $\approx 4 \cdot 10^{15}$ eV from a value of ≈ 2.7 to ≈ 3.1 (a feature called the *"knee"* due to the resemblance in shape with a bent human leg, see Figure 1.1) [15].

$$\frac{dN}{dE} \propto E^{-\gamma} \tag{1.1}$$

Since its discovery in 1958 when registering the total intensity (*"size"*) of observed EAS, the knee has been described in numerous theoretical and experimental investigations. There are a number of models [16] giving a possible explanation for the presence of the knee in the spectrum, but its origin remains still a subject of debate. Among possible sources of the change of power law index there could be:

- The acceleration mechanism. Models of this kind are related to the diffusive shock acceleration phenomenon. It is assumed that the cosmic ray particle originates from within our galaxy and that it can achieve a maximum energy that is function of the number of crossings of the shock front. As this number depends on the charge of the particle, the position of the knee changes with the Z of the particle [17–19].

- Features of propagation mechanisms. Such models describe the probability of cosmic ray particles to escape the confinement (by magnetic fields) of our galaxy. The effect is caused by drifts of particle trajectory induced by irregular magnetic fields. The probability of this effect increases with particle energy per charge unit and leads to a steepening of the spectrum for energies above 3 PeV. As the effect is charge dependent, the position of the knee will change with the Z of particles as in the case of the previous model [20, 21].

- Space objects in close proximity to Earth. This model was suggested by the sharpness of the spectral index change, a feature that can not be explained only by glactic diffusion/escape of cosmic radiation. The idea explains how the radiation of a near young supernova remnant is modulating the cosmic ray background with its own shock waves-accelerated particles [22].

- Exotic reactions. This model describes how heavy neutrinos (m_ν=0.4 eV) might be involved in reactions such as 1.2 with an energy threshold of 3 PeV [23] (leading to the disappearance of the protons).

$$p + \bar{\nu}_e \rightarrow n + e^+ \tag{1.2}$$

- Finally there is also under debate that there exists no knee in the energy spectrum of primary cosmic rays and that in fact the knee is a mis-interpreted feature of air shower development. The knee observed in extensive air showers might be induced by the production of heavy undetectable exotic particles with exotic interactions. [24]

A *"second knee"* (a discontinuity in the spectrum) has been predicted at energies of about $4{\cdot}10^{17}$ eV. Though suggested by the measurements of some experiments (Yakutsk [106], Haverah Park [26], Fly's Eye [27], HiRes-MIA [28]), the existence of this feature is still not proven, as other detectors did not see it (AKENO [29], AGASA [32]). Further structures of energy spectrum are visible at even higher energies. It is the case of *"ankle"* at around $5{\cdot}10^{18}$ eV. There are several models describing the second knee and the ankle:

- In the first model [33], the galactic component brakes down at energies few times 10^{17} eV. The extinction of the galactic component (made mostly of iron at these energies) and the transition to the extragalactic one leads to a knee-like feature, the second knee. The extragalactic background is mostly protons and the ankle is regarded as purely a feature of the extragalactic radiation and is due to the *"cooling"* of the high-energy protons in a reaction producing electrons and positrons. This model predicts a predominantly proton composition for the cosmic rays at ankle energies.

- The second model [34] describes how an additional source of radiation extends the galactic spectrum up to energies close to the ankle. In that energy range ($\approx 10^{19}$ eV) the extragalactic proton component is mixed with the extended galactic spectrum and the ankle is a feature of the superposition of the two (a transition effect). The second knee is the result of the extinction of the galactic iron component. This model predicts a mixed composition at $\sim 10^{18}$ eV.

Finally another feature is the GZK cut-off, predicted by Greisen, Zatsepin and Kuzmin [35, 36]. They showed that for energies of $5{\cdot}10^{19}$ eV the photons of the cosmic microwave background reach an energy of 200 MeV (in the center of mass frame) thus exceeding the energy threshold for pion production with nuclei. As a result, the ultra-high energy particles exceeding the threshold energy will quickly loose energy and since they are predominantly extragalactic the cut-off should be visible in the spectrum. The existence of this feature is a matter of controversial current debates.

Observing the extensive air showers generated by primary particles in the Earth's atmosphere is a powerful observation possibility of high-energy cosmic rays. The following chapter will give a more detailed description of the structure, composition and detection techniques of EAS. An air shower composed of millions of particles will always be much easier to detect due to its high particle content and also due to its size (even at lower energies, the shower front of the EAS can easily cover thousands of square meters and some of its components can even be measured from far distances, e.g. by UV-fluorescence). Birth and development of an EAS are greatly influenced by the nature of the primary particle, the primary mass and energy. A shower born later in the atmosphere will evolve differently and, similarly,

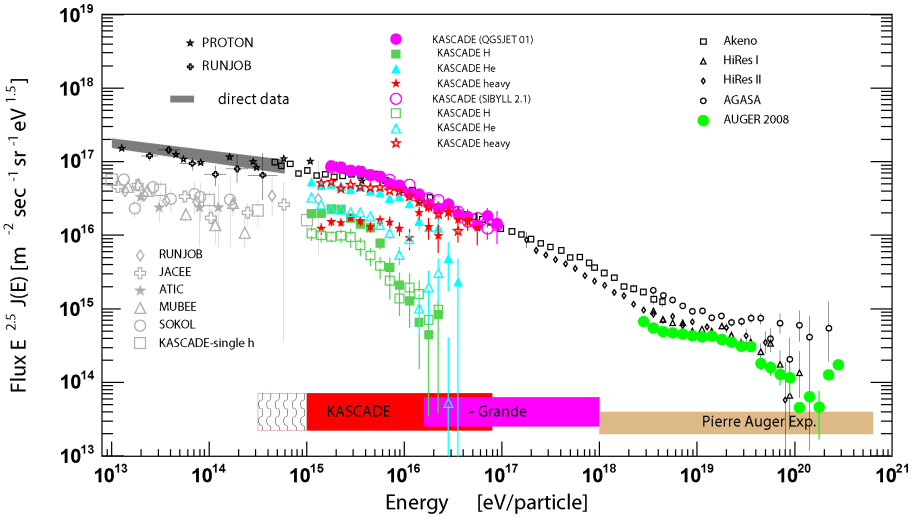

Figure 1.1: The primary cosmic radiation energy spectrum showing the knee region (the ranges *KASCADE*, *Grande* and *Pierre Auger Experiment* show the detection range for the respective detector arrays); the Kascade-Grande experiment will be presented in more detail in Chapter 3; for more information on other experiments check Appendix A for a list of relevant properties and references (from [37]).

different primary particles will suffer different primary interactions generating a different mass distribution of secondaries. Since such differences between two EAS phenomena are measurable, arises here the possibility of gaining information on the primary particle by studying the measurable properties of the extensive air showers (such measurable properties of the EAS are commonly named observables). However, due to the great number of interactions in the atmosphere, the information carried by the primary particle is greatly diluted. It is just the task of the analysis of the observations to disentangle the information carried by the EAS in order to retrieve information on the primary particle.

The studies presented in this thesis are performed in the context of the KASCADE-Grande [38] experiment set up at Karlsruhe Institute for Technology, Campus Nord, Germany and designed to operate in the 10^{16}-10^{18} eV energy range. It aims to reconstruct the primary energy spectrum from measurements of EAS observables. The investigated observable is the particle density at 500 m distance from shower core (referred as $S(500)$). It has been shown that, for a given experimental setup, at a given distance from the shower core, the charged particle density becomes independent of the primary mass and thus could be used as a primary energy estimator [39]. The particular distance at which this effect takes place is detector-specific and in the case of the KASCADE-Grande detector array it was shown to be ≈500 m [40]. A similar investigation technique has been applied in the case of other experiments aiming at reconstructing the primary energy spectrum. Thus, the AGASA [45, 46] experiment and later the Auger experiment [46] used particle densities to infer information on the primary spectrum. Due to the different features of the two experiments their observables of interest were $S(600)$ [47] and $S(1000)$ [48], designating particle densities at 600 m distance from shower core (AGASA) and at 1000 m distance (Auger

experiment) respectively. For the purpose of this study a software reconstruction tool (SHOWREC) [41] has been developed and used for reconstructing the EAS observables. This tool is used in parallel with the standard reconstruction tool employed at the site of the KASCADE-Grande experiment [42, 43]. With SHOWREC, starting from the energy deposits of particles in detectors and using a Linsley [44] function as mathematical approximation for the lateral particle density distribution, the charged particle density at 500 m distance from shower core is reconstructed. In order to reconstruct the experimental energy spectrum of the primary radiation, the Constant Intensity Cut Method [45] is employed along with a simulation-derived E_0 - $S(500)$ calibration.

Chapter 2

Extensive Air Showers

The secondary component of the cosmic radiation which we usually observe on ground is a stream of particles generated in the Earth's atmosphere by the primary cosmic radiation from outermost space colliding with the air molecules. An incoming primary particle of sufficiently high energy develops by multiple interactions into an avalanche of particles, commonly called Extensive Air Shower (EAS). Extensive air showers have been discovered in 1938 by P. Auger et al. [2,49] and independently by W. Kohlhörster et al. [3]. An EAS is usually initiated high in the atmosphere when the primary particle hits a molecule of the Earth's atmosphere (the phenomenon appears only for higher primary energies, lower energy primaries producing the uncorrelated muons of the secondary cosmic radiation). The resulting fragments and secondary products of such a collision continue to propagate downwards, colliding repeatedly until the EAS evolves into a *"pancake"* which, depending on the primary energy, may contain billions of high energy particles. The EAS form is usually a curved surface with a thickness increasing with the distance from the shower axis (represented by the incident direction of the primary). That means there is a distribution of arrival times of the EAS particles on ground, a feature which has been occasionally studied [50].

As the energy of the primary dissipates by secondary interactions, the EAS particles eventually decay and are absorbed. The dominating electromagnetic component (photons and electrons) is usually the one absorbed faster in both time and with distance to shower core. Other components are more penetrating like the muon component.

A graphical representation of the downwards EAS development towards a detection array is displayed in figure 2.1. Since the shower particles are spreading more and more in lateral direction while crossing the atmosphere (as a result of transverse momenta gained during collisions or particle production), we may intuitively understand the shower shape gradually taking the form of a slightly curved disk with a diameter of the order of 1 km and a thickness of about 1 m near the shower axis, slowly increasing to the order of 100 m at a distance of about 1 km. When performing an arrival time analysis as reference time value the moment of shower core reaching the detector level may be used. All arrival times that are counted in relation to this moment are called global arrival times.

There are three main components of particles in EAS: electromagnetic component (electrons/positrons and photons), muons, and hadrons (near shower axis).

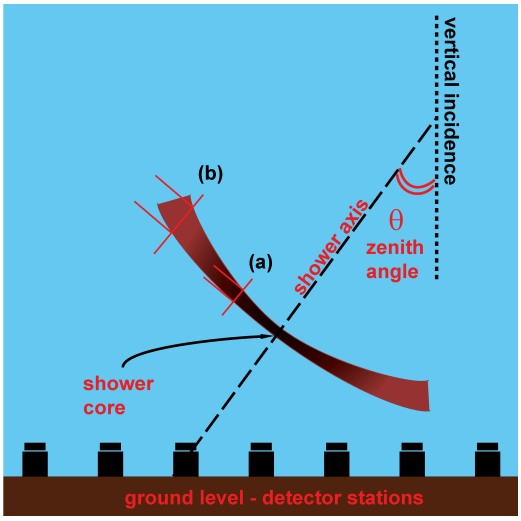

Figure 2.1: The geometrical structure of an EAS as seen in relation with the detector plane; the two transversal markings (a) and (b) give an idea on how the shower front thickness increases with the distance from shower core, thickness(a) <thickness(b).

For example, an EAS initiated by a 10^{15} eV proton contains approximately half a million secondaries at sea level, of which about 80% are γ-rays, about 15% electrons and positrons, about 2% muons, and about 0.2% hadrons. Most secondary particles produced by primary strong interactions are π mesons. The neutral π_0 mesons decay almost immediately into γ-rays:

$$\pi_0 \rightarrow \gamma + \gamma \tag{2.1}$$

These γ-rays start electromagnetic avalanches by pair production (e^+e^-) and by bremsstrahlung processes. When the electrons and positrons reach an energy level of about 100 MeV, energy loss by ionization starts to become important and the particles are stopped quickly. After reaching its maximum size, the particle number in the EAS decreases approximately in an exponential way. The charged $\pi^{\pm}$ mesons either interact with atoms of the atmosphere or decay into muons. The muon component originates from the decay of charged pions and also kaons:

$$\pi^{\pm} \rightarrow \mu^{\pm} + \nu_{\mu}(\overline{\nu}) \tag{2.2}$$

$$K^{\pm} \rightarrow \mu^{\pm} + \nu_{\mu}(\overline{\nu}) \tag{2.3}$$

Muons form the penetrating EAS component since they get less absorbed and reach the ground with high probability (the higher energy muons penetrating also in deep underground). This is also due to their comparatively long lifetime, which is enlarged by relativistic time dilatation. In-flight decays of muons lead to generation of decay electrons that add to the electromagnetic component. Together with the electron component, the muon component forms the charged particle component with the integrated intensity (*"size"*) Nch. In EAS studies at high altitudes, the shower size is sometimes considered more or less equivalent to the electron size: Ne $\approx$ Nch.

Finally, the backbone of an air shower is situated around the shower axis and consists of the hadronic component containing mostly pions but also nucleons, anti-nucleons, K-mesons and more exotic particles.

In order to measure the sizes of the different components, a typical EAS experiment uses an array of detector stations covering a large area in the 10^3 m^2 range and records the lateral particle densities distributions by sampling the area by various kinds of detectors . Then, using an a-priori assumed form for the lateral distribution (lateral distribution function) the distribution of the particles is adjusted and the size is determined.

The three main EAS components, whose development is sketched in Figure 2.2 are accompanied by Cherenkov, nitrogen fluorescence and radio emission [37] in the atmosphere. Each component provides specific observables that carry information on the primary particles. Depending on the kind of observable one wants to record, different types of detector systems have been used leading in many cases to the installation of complex detector systems capable of detecting different components of the same EAS simultaneously. By such a detection system correlated studies among different observables become possible. The KASCADE-Grande detector array that is used for the experimental studies of this work is just such a device.

In order to give some impression about the structure and of the differences of various EAS components, figures 2.3 and 2.4 show some threedimensional representations of simulated EAS on ground (in figure 2.4 separately the shower components of gammas, electrons, muons and protons). Note the significant change of particle density distribution and arrival times for different species of particles at the same radial range.

The investigation of EAS which has been in former times directed to explore the inherent features, the development and the structure of the phenomenon, is nowadays mainly focused to the understanding, in which way some features can be related to the energy and the mass of the primary and can be used as signatures for these primary properties. Simulation studies have demonstrated that, in average, heavy ion induced air showers develop differently from proton induced showers due to a smaller interaction length and due to a larger number of nucleons in the projectile. This is corroborated by the effect that the multiplicity of secondary particle production per nucleon varies only slowly with the energy. Thus the muon content of an iron induced EAS e.g. appears to be larger than for the proton induced one. Simultaneously the number of electromagnetic particles (e/γ) gets larger in the proton EAS because their energies reflect the energies of the neutral pions they originate from. As electrons and positrons are rapidly absorbed when their energies drop below ca. 100 MeV, an A-nucleon shower (with each nucleon carrying the energy E/A) reaches earlier the maximum of its longitudinal development, i.e. higher in atmospheric altitude. That means for the same primary energy E the shower sizes (N_e) are different for different kind of primaries observed at the observation level . Since we neither know a-priori the energy nor the mass of the primary, energy determination and mass discrimination is an entangled problem. Therefore many attempts are focused to minimize the influence of the mass on the observable which serves as energy estimator, e.g..

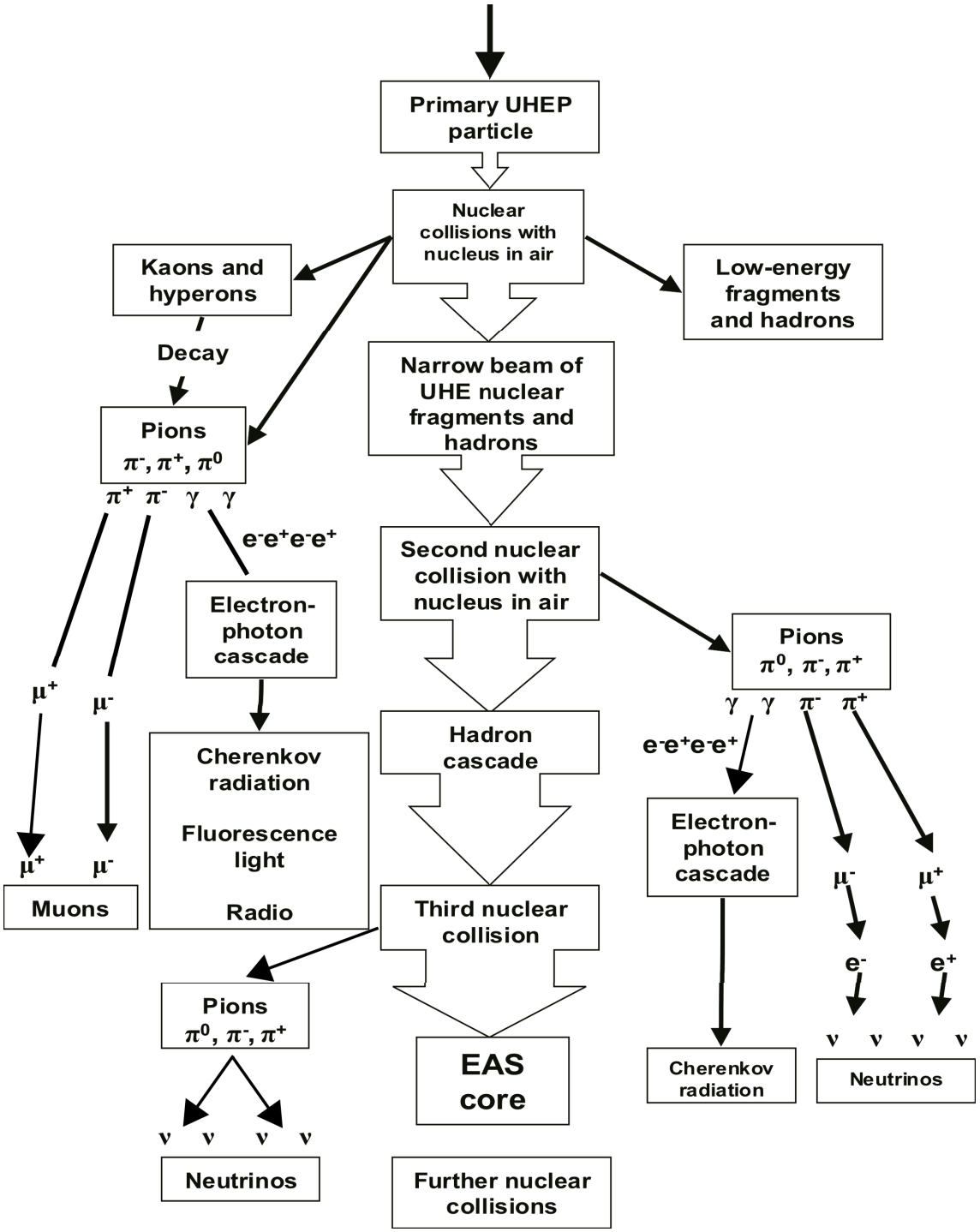

Figure 2.2: Sketch of EAS development.

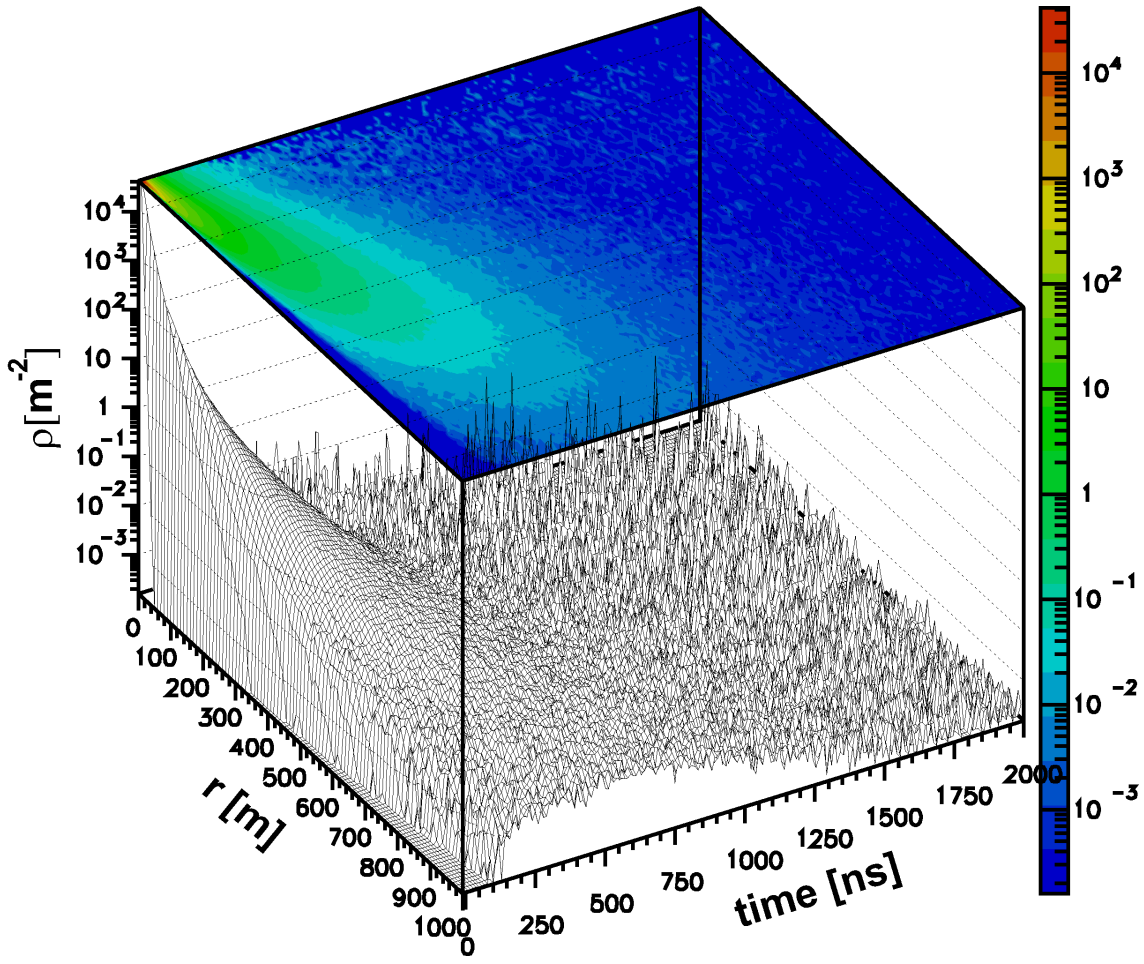

Figure 2.3: 3-dimensional representation (axes: r[m], ρ[m^{-2}], time[ns]) of an EAS initiated by a vertical proton primary (θ=0°) with an energy of 10^{15} eV; the vertical axis (ρ[m^{-2}]) displays the all-particle density in the event for a given distance (axis r[m]) to shower core (the shower core is positioned in r=0 m); the arrival delay of particles at ground level is visible in the increasing thickness of the shower front (along the time[ns] axis); the lateral particle density distribution and global arrival time are presented here for gammas and all charged particles; note the dramatic decrease of particle density with the increasing distance from shower core; a contour plot is given on top of the 3D surface as an alternative representation; also note the scale associated to the contour plot. (G. Toma, National Physics Conference, 2004, Pitesti, Romania).

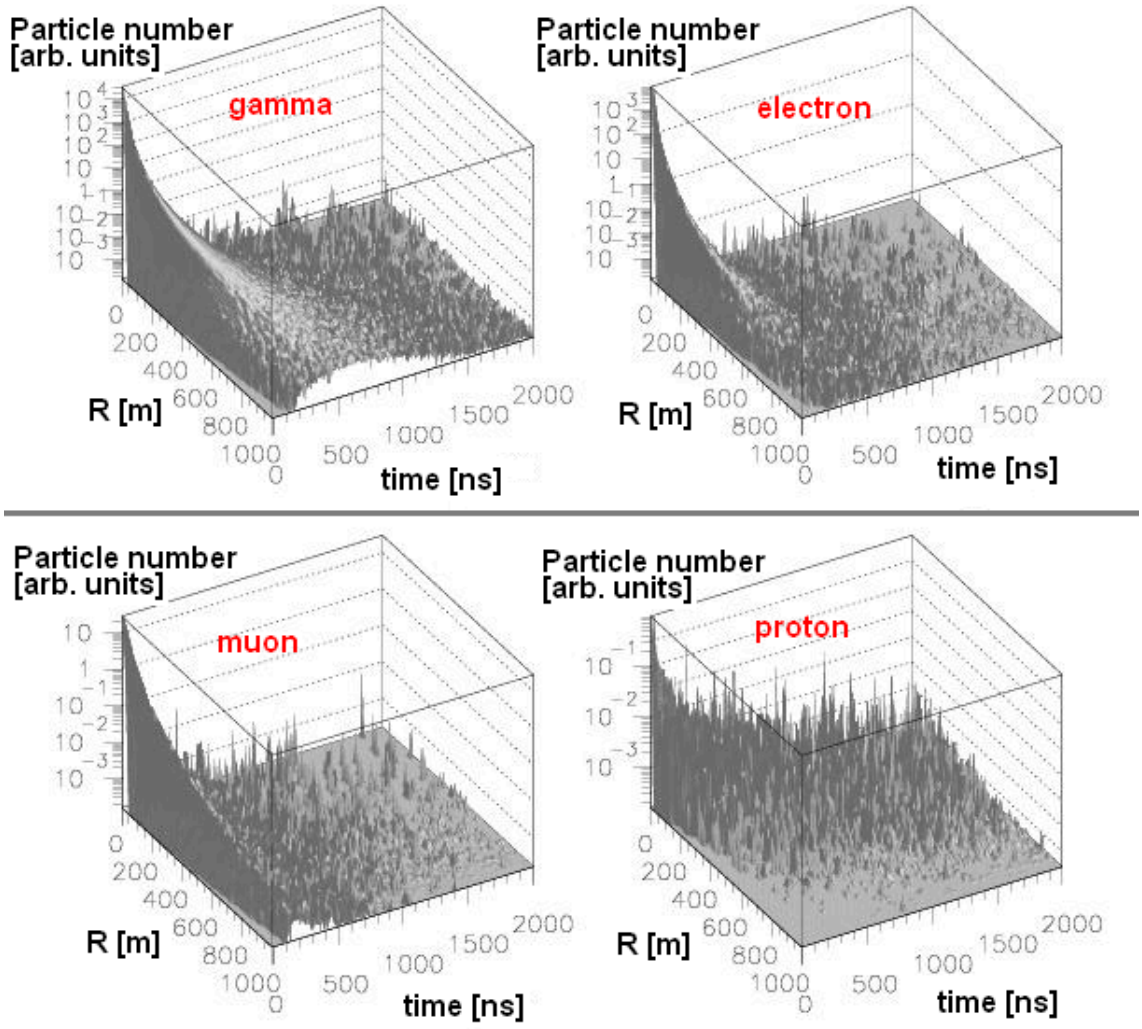

Figure 2.4: Shower structure for different components: the most abundant constituents of an EAS are the photon and electron components (with the muon component considerably more flat than the two); it is also visible that the proton component propagates close to the shower axis.

The KASCADE experiment which has successfully studied the mass composition of cosmic rays around the knee [51] has developed the N_e-N_μ correlation method to a practical procedure by introducing the so called truncated muon number [52]:

$$N_\mu^{tr} = \int_{40m}^{200m} \rho_\mu(r) r dr \tag{2.4}$$

This quantity is not only experimentally accessible, it proves to map the primary energy due to various fortunate features [53].

For many arrays the information about the muon component is rather scarce and biased by extrapolations. This is the case with KASCADE-Grande as the Grande detectors register only charged particles without electron-muon separation. This has triggered the topic of this thesis to infer information on the primary energy from the lateral distribution of the charged particles.

The charged particle density at detector specific distances from EAS core

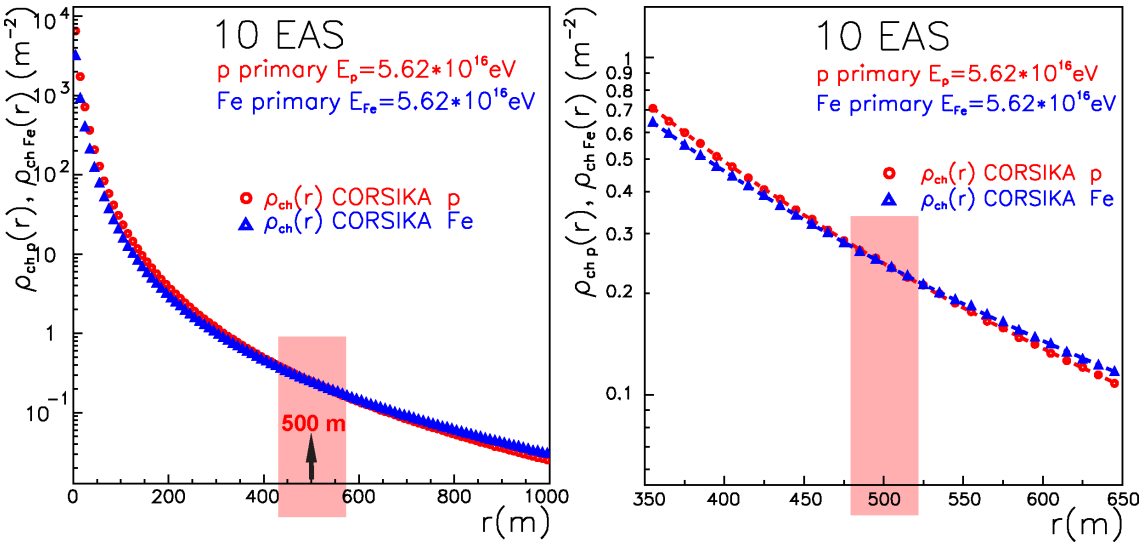

Figure 2.5: The plot shows averaged CORSIKA simulated lateral particle density distributions for p and Fe induced showers with E_0=5.62·10^{16} eV (CORSIKA is a simulation code used for the simulation of air showers development and it will be presented in more detail in chapter 4). The plot on the right presents the extended radial range 350 m - 650 m and the Linsley fits with dotted lines. *(G. Toma et al. - KASCADE-Grande collaboration, ISVHECRI 1-6 September 2008, Paris, France)*

has been shown [39] to become nearly independent of the primary mass (within the fluctuations). It may be used as a primary energy estimator. The specific radial range where this effect takes place is a characteristic of the detector array and so it changes from one detector system to another:

- charged particle density at 600 m distance from shower core - $S(600)$ [47] - for the Haverah Park [26] and AGASA [32];

- charged particle density at 1000 m distance from shower core - $S(1000)$ [48] - for the Pierre Auger observatory [54, 55];
- charged particle density at 500 m distance from shower core - $S(500)$ [40,56,57] - for the KASCADE-Grande (figure 2.5)

We follow this concept for the KASCADE-Grande data. There is a number of alternative approaches to deduce the cosmic ray spectrum from observations of KASCADE-Grande whose actual results have been nicely compared at the 31st ICRC 2009, Łódź, Poland [58].

Chapter 3

KASCADE-Grande

The studies of this thesis are based on experimental observations of EAS with the KASCADE-Grande [38, 59] detector array, in particular on measurements of the lateral distribution of charged EAS particles. In its general structure and operation, the KASCADE-Grande array resembles other cosmic ray experiments. It is composed of many detector stations that are distributed over a wide area and have been designed to record particle densities. The lateral particle density distribution is subsequently inferred by adjusting the data registered with the detector stations to an a-priori assumed lateral distribution function. In a further step and by following some knowledge derived from Monte-Carlo simulation studies, the analysis of the lateral distribution is focused to reconstruct the properties of the primary particles. The array is situated at the site of the Forschungszentrum Karlsruhe (since 1.10.2009 renamed to Karlsruhe Institute for Technology -KIT, Campus North), Germany (49° N, 8° E) at 110 m a.s.l. It has a roughly rectangular shape with a length of 700 m. A complex multi detector system of various types of detectors enables the registration of different EAS observables.

Historically, the KASCADE-Grande detector array is an extension of a smaller array, the KASCADE array, operated since 1996 [60]. KASCADE was designed to record air showers initiated by primaries with energies in the 10^{14}-10^{16} eV range (including the knee range whose origin to clarify was one of the goals). The KASCADE detector is a complex detector array (Figure 3.1) providing information on a considerable number of observables associated with the electromagnetic, muonic and hadronic component. It is composed of the Field Array, a complex Central Detector (presently no more operated) and a Muon Tracking Detector underground. Each of these components have been designed to measure specific observables. Thus, the Field Array of scintillation detectors measures the electromagnetic and muon components with electron and muon energy thresholds of 5 MeV and 230 MeV. It is used to reconstruct the EAS core position, arrival direction and particle numbers. The Muon Tracking Detector is used to detect the arrival direction of muons with 800 MeV threshold. The Central Detector consisted mainly of a hadron calorimeter complemented by a trigger and timing detector plane, of Multi-Wire Proportional Chambers and Limited Streamer Tubes. The Central Detector and Muon Tracking Detector (MTD) had provided or do currently provide measurements of data of the hadronic component and the high energy muons (with a 490 MeV and 2.4 GeV energy threshold for the muonic component and 800 MeV for the MTD).

The extension of the original smaller but rather detailed KASCADE array

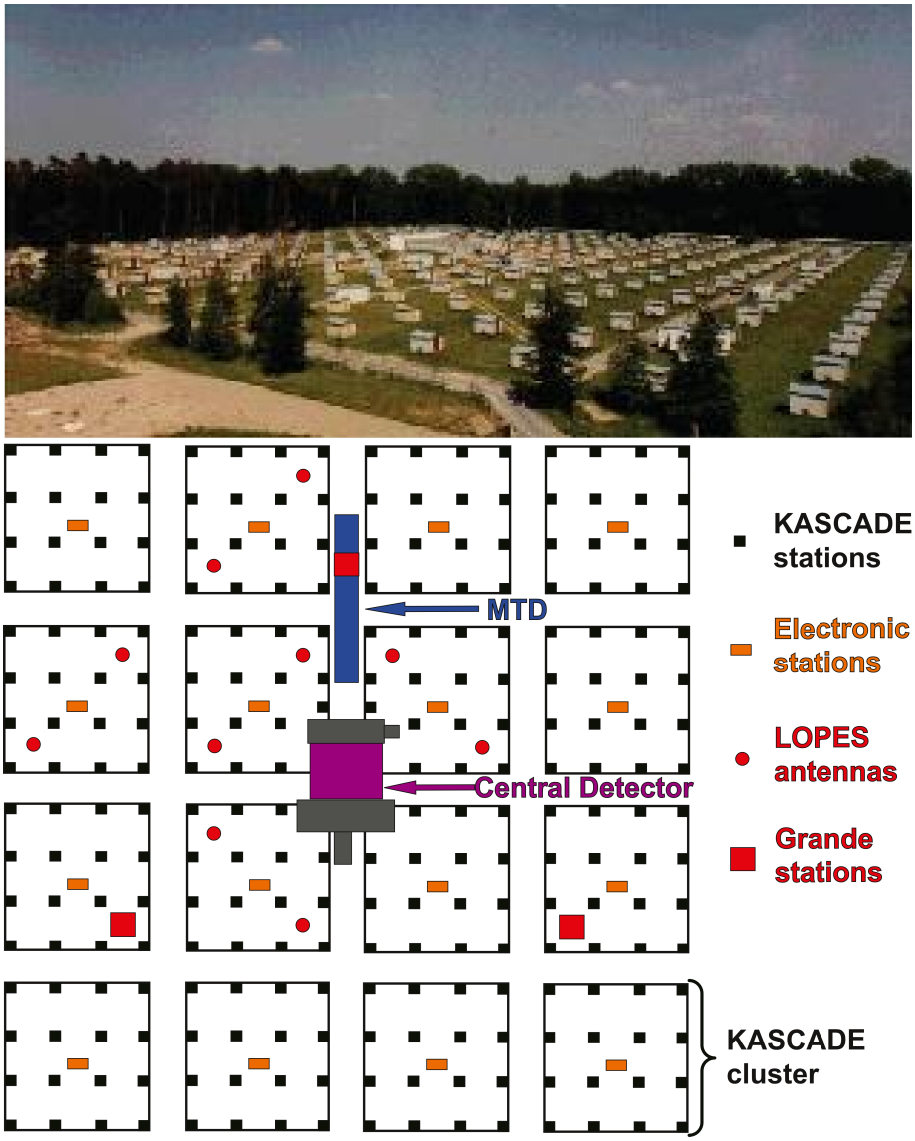

Figure 3.1: Schematic layout (below) with a photo of the KASCADE experiment (the Muon Tracking Detector (MTD) and the Central Detector are seen along with three Grande stations that fall inside the area of KASCADE array and the LOPES-10 radio antenna configuration).

was guided by the intention to extend the energy range for efficient EAS detection to the energy range of 10^{16}-10^{18} eV. This energy range provides various interesting aspects: the expected transition from galactic to extragalactic origin of cosmic rays and, in particular the question whether there exists a further "knee" in the energy spectrum. The actual layout of the extension of KASCADE to KASCADE -Grande was governed by following basic considerations. Higher energy showers appear with smaller frequency. Thus, in order to record a reasonable amount of events in a reasonable amount of time, a larger size of the array is necessary. The other aspect arises from the functionality of detectors themselves. High energy primaries generate

particle - rich showers that tend to saturate the detectors stations close to shower core (where the particle density is very high). Consequently for a small array, data recorded close to shower core is not reliable. It appears necessary to extract data from the EAS at greater radial distances in order to specify the observed EAS.

The Grande array is set up in the area of Karlsruhe Institute for Technology (see Figure 3.2) by 37 detector stations (formerly installed in the EAS TOP array [61]), arranged in a roughly hexagonal grid with a spacing of about 140 m. Each station houses plastic scintillation detectors (NE102A) organized in 16 units with a total effective area of 10 m^2 per station. The station hut itself is made of metal and is placed above a concrete base. Figure 3.3 presents a schematic 3-dimensional view of the inside of a Grande station. The scintillator plates (80 $\times$ 80 $\times$ 4 cm) are arranged in a 4 $\times$ 4 pattern inside each hut. Each plate is enclosed in a steel casing of pyramidal shape. The plate is viewed from below by a high gain photomultiplier (HG, $\sim$ 1.6 pC/m.i.p.; Philips XP3462B), as shown in figure 3.4 (this image presents a schematic cut-away through one scintillator module, showing the scintillator plate inside and the photomultiplier below). Additionally, the 4 central modules are equipped also with low gain photomultiplier (HG, $\sim$ 0.08 pC/m.i.p.).

A smaller trigger array, Piccolo was considered to be necessary for triggering of the high-energy muon devices of KASCADE (fig. 3.2). The Piccolo array consists of 8 stations of 10 m^2 with plastic scintillators placed on an octagon at 20 m distance from each other. The Piccolo array, positioned between KASCADE and the Grande center aims to provide a fast trigger to the muon detection systems in the KASCADE central detector and the muon tunnel.

As a specific component a system of 30 radio antennas (LOPES [62]) has been installed inside the KASCADE-Grande area. Since the phenomenon of radioemission from EAS has been rediscovered [62] there is a lively activity to record radio emission correlated with showers detected with the KASACADE-Grande array [63]. The radio antennas are arranged in various geometrical layouts: LOPES-10, LOPES-30 and LOPES^{STAR} (as indicated in figure 3.2).

The KASCADE reference coordinate system has been defined with origin in the center of the KASCADE array and the orthogonal axes oriented parallel to the border of the array. After the extension to KASCDE-Grande and integrating the KASCADE field the same reference system is in use.

Table 3.1 compiles the detection parameters of different components of the experiment. While the KASCADE detector stations were capable (by design) to measure separately the e/γ and the muon component, the 37 Grande scintillator stations are not able to do so. The registered energy deposit is the summed contribution of all charged particles and photons that interact in the sensitive volume. This feature goes well in accordance with the case of this study in which we are concerned with the investigation of the summed EAS charged component.

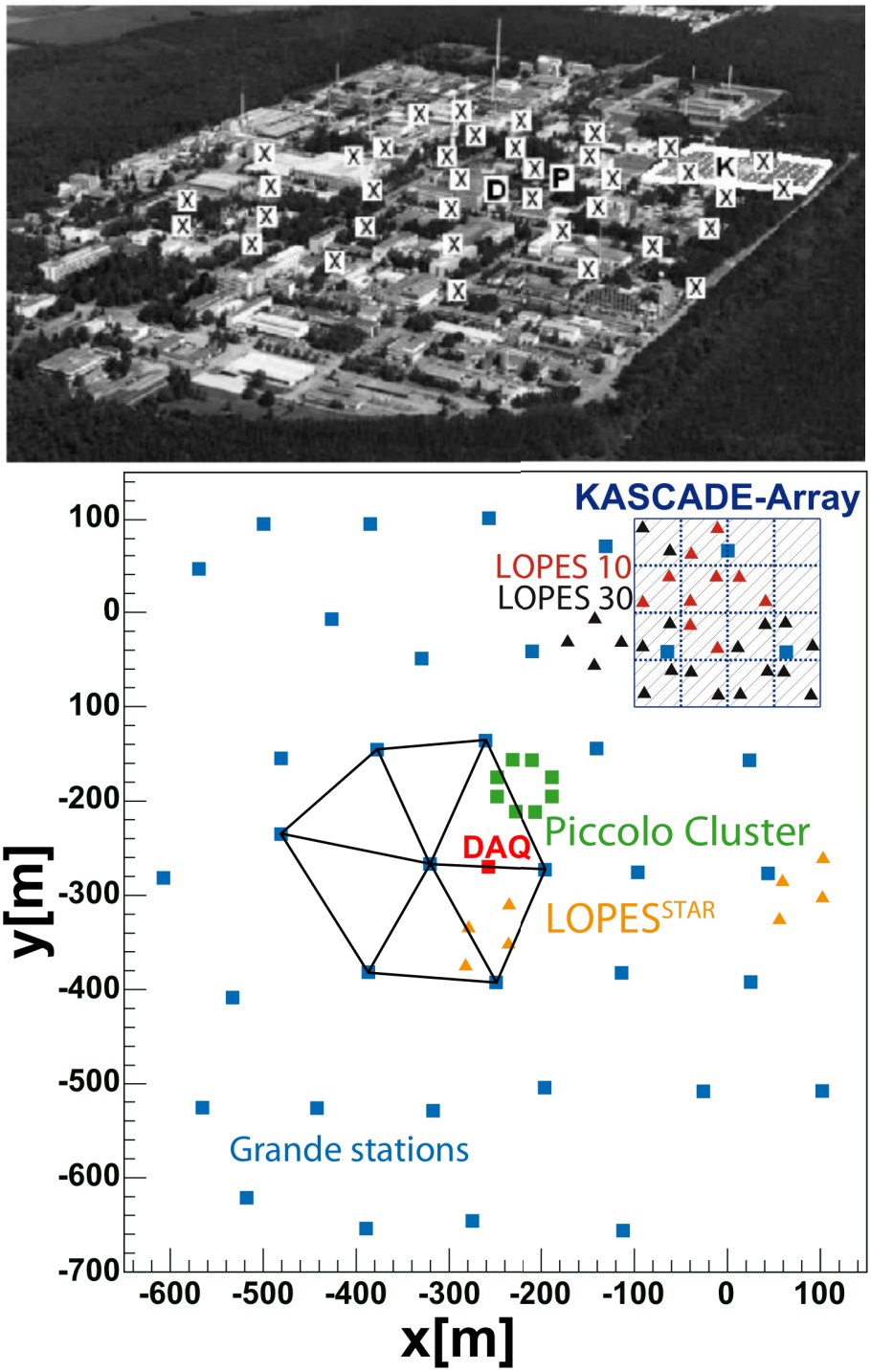

Figure 3.2: Photo of the Grande (X marks) and Piccolo (P mark) arrays in the Karlsruhe Institute for Technology, Campus Nord (the KASCADE array is visible at the upper right side of the picture - K mark). The lower part of the figure shows a schematic top-view of the KASCADE-Grande detector array (cluster number 10 of the total 18 is indicated with connecting lines between); the Piccolo and LOPES arrays, **D**igital **Acq**uisition (DAQ) station and KASCADE array are also indicated.

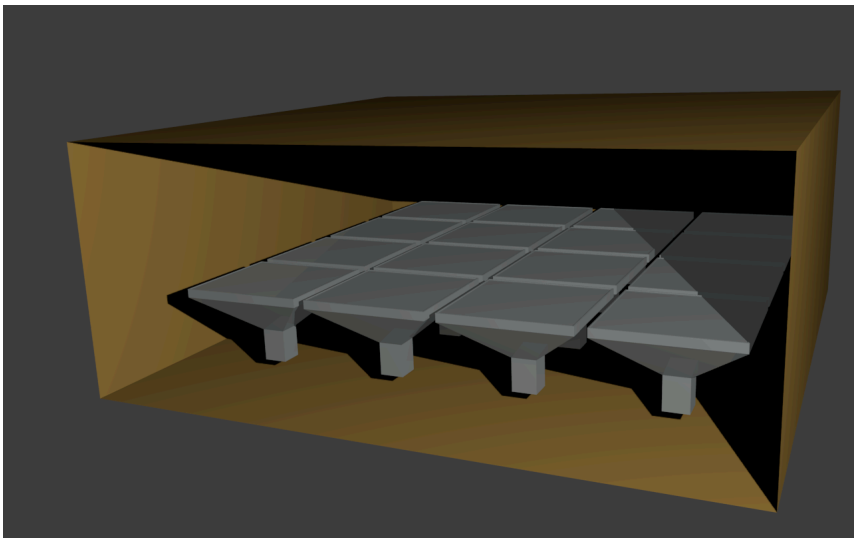

Figure 3.3: Schematic 3-dimensional view of the inside of a Grande station.

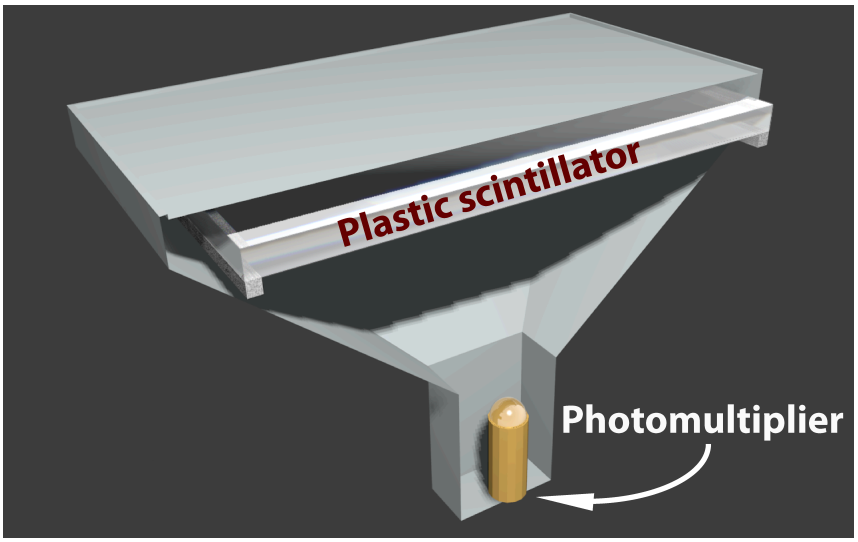

Figure 3.4: Cut-away through one scintillator module, showing the scintillator plate inside and the photomultiplier below.

Detector	**Particle**	**Area [m^2]**	**Threshold**
Grande array (plastic scintillators)	charged	370	5 MeV
Piccolo array (plastic scintillators)	charged	80	5 MeV
KASCADE array (liquid scintillators)	$e^{+/-}$	490	5 MeV
KASCADE array (shielded pl. scint.)	μ	622	230 MeV
Muon tracking det. (streamer tubes)	μ	3×128	800 MeV
Multi wire proportional chambers	μ	2×129	2.4 GeV
Limited streamer tubes	μ	250	2.4 GeV
KASCADE Central Detector (liquid ionization chambers)	hadrons	320	20 GeV
LOPES antenna array	radio signals	-	-

Table 3.1: Components of the KASCADE-Grande detector array with their detecting capabilities.

Chapter 4

EAS reconstruction

An EAS reconstruction is a chain of operations performed with the direct detector information in order to obtain certain quantitative and qualitative information by specific quantities characterizing the observed EAS event. The most simple observables are the location of the EAS core and the arrival direction, expressed by adequate array coordinates and the polar and azimuthal angles of the axis of incidence, respectively. Thus a very illustrative technique to reconstruct a shower core is to calculate simply the "center of gravity" of energy deposits in the detector stations of an array. This procedure is used in many reconstruction codes to define a first estimate of a shower core location, before more elaborate operations are performed. Similarly is the use of time information in order to obtain an estimate of the arrival direction. The distribution of global arrival times is the direct result of shower front shape and shower front arrival direction. For a small array (up to ranges where the shower front curvature remains negligible), the shower front can be approximated with a plane surface. A simple fit of the arrival time distribution will give a first estimate of the EAS arrival direction. Physically more essential quantities on which the interest of this thesis is focused are the lateral charged particles distributions of different kind of EAS particles. From these distributions the total intensities (*"sizes"*) of the EAS and related quantities are deduced.

Before advancing to more detailed procedures one has to understand some principal differences between the reconstruction of EAS generated by a simulation code and the reconstruction of actually experimentally observed showers. EAS simulation codes deliver usually the particles of the various EAS components distributed over the full area of the considered array. To prepare useful predictions for the experiment, these information has to be "distorted" according to the response (efficiency and detection thresholds) of the actual detectors and the array layout. In case of experimentally observed EAS the information is already distorted. In particular, with detectors like in KASCADE-Grande we do not observe "particles", but the energy deposits in the detectors. Hence the first task is to translate these deposits efficiently and as reliably as possible to particle densities for further manipulations [64–66]. The essential part of this chapter is concerned with this task.

This chapter will detail the simulation procedures involved in the simulated EAS studies, it will then sketch the standard reconstruction procedure that is applied in KASCADE-Grande experiment, followed by a more detailed presentation of the SHOWREC reconstruction procedure applied in the course of these studies.

The features of the applied lateral distribution function used to the data are studied. Emphasis will be put on reconstructing relevant EAS observables starting from detector information, especially on the reconstruction of $S(500)$ (Chapter 5).

4.1 Simulation strategies

The investigations presented in this thesis rely heavily on the use of Monte Carlo simulations. Several aspects have been investigated through simulated means: the EAS phenomenon itself (development and structure), the EAS interaction with detector systems and the $S(500)$ reconstruction quality. Two types of simulations have been performed for the purpose of the study (presented in more detail in the following subsections):

- A full Monte Carlo simulation of the EAS development and also of the EAS interaction with the KASCADE-Grande detector stations. Technically, the simulation procedure is implemented in the CORSIKA [67] and CRES (based on GEANT [68]) codes. As it will be shown later, the main purpose of this simulation is to bring the simulated data to the same level of consistency of the recorded experimental data. From now on, when referring to simulated results, full Monte Carlo simulations are meant by default.
- A purely mathematical and geometrical toy Monte Carlo investigation of the EAS reconstruction aimed at characterizing the $S(500)$ reconstruction quality and finding a set of relevant quality cuts. The simulation routines are developed by the author. When discussing results of the toy Monte Carlo simulations this will be mentioned explicitly.

4.1.1 Full Monte Carlo simulations

The full Monte Carlo simulations strive to give an "as accurate as possible" description of the EAS phenomenon starting from the first interaction of the primary particle, passing through EAS development down to detection level and followed by the interaction of EAS secondary particles with the detector stations.

The birth and development of the EAS are described by the widely used Monte Carlo simulation tool CORSIKA [67] (COsmic Rays SImulations for KAscade). Originally developed to perform simulations for the KASCADE experiment, CORSIKA is now widely used by many research groups involved in EAS investigations. The CORSIKA program allows for the simulations EAS events initiated by nuclei, hadrons, muons, electrons, and photons with energies up to $2{\times}10^{20}$ eV. For a selected observation level, the program output gives the type, energy, location, direction and arrival times of all secondary particles that are created in an air shower. The CORSIKA program consists basically of four parts, each of them responsible with handling of different aspects of air shower development (several models are available for describing the particle interactions and can be activated optionally):

- Besides handling the input and output of the program, the first part is concerned also with the decay of unstable particles, and tracking of the particles taking into account ionization energy loss and deflection by multiple scattering and the Earth's magnetic field.

- The second part treats the hadronic interactions between the nuclei and hadrons with the air nuclei at high energies. The available models for describing these interactions are: The Dual Parton Model DPMJET [69], the simple Monte Carlo generator HDPM [70] which is inspired by the Dual Parton Model, the quarkgluon-string model QGSJET [71,72], the mini-jet model SIBYLL [73,74], the VENUS [75] model or the NEXUS model [76] (NEXUS combines algorithms of VENUS and QGSJET with new ideas, based on H1 [77] and Zeus [78] data). The last added model is the EPOS [79] (based on the NEXUS framework, but with important improvements).

- The third part describes the hadronic interactions at lower energies with one of the codes: FLUKA [80], GHEISHA [81], or UrQMD [82].

- The fourth part describes the transport and interaction of electrons, positrons and photons by using the EGS4 [83] code (for following each particle explicitly) or by using the NKG [84] parameterizations in order to obtain electron densities at selected locations and the total number of electrons at up to 10 observation levels.

Additionally it is also possible to explicitly generate Cherenkov radiation in the atmosphere or to include the description of electronic and muonic neutrinos and antineutrinos, primary neutrinos [85, 86], and to simulate showers with flat incidence. Also in order to reduce the computation time for primary energies E_0>10^{16} eV the thinning option exists (with which only a fraction of the particles are followed explicitly during the shower development).

The GEANT3 based code CRES (cosmic ray event simulation) is used to simulate the detector response. It uses the EAS particles at detector level from CORSIKA in order to simulate the energy deposits in detectors and the detector response. After applying CRES, the simulated events have the same significance as the experimentally recorded ones and the same reconstruction procedure may be applied to both cases.

For the purpose of this study, EAS events have been generated using the CORSIKA (v. 6.307) simulation tool and their interaction with the detector stations was simulated using the CRES tool. Different primaries have been considered for the simulated events as follows: H, He, C, Si, Fe. The primary energy range $1.0{\cdot}10^{13}$ - $1.0{\cdot}10^{18}$ was used in the CORSIKA input with the QGSJET II model embedded for simulating high energy interactions. The input primary energy spectrum had a power law shape with a spectral index of γ=-2 (this particular shape has been chosen for computing time and storage space reasons). EAS events have been simulated up to 42° zenith angle. In order to save considerable computer time, the same CORSIKA simulated events have been used multiple times as input for CRES by shifting their core randomly around the array surface. In total, a number of 1 764 950 simulated events were available for reconstruction.

4.1.2 Toy Monte Carlo simulations

The toy Monte Carlo test is a simplified, much faster version of the full simulation test, in which only the geometrical properties of the detector array are simulated. The only simulated EAS properties are the shower core position (distributed randomly over the surface of the array) and the lateral particle density distribution. The latter is generated as a purely mathematical Linsley [44] shape for different radial range values, emulating the particle density in different detector stations. The Linsley parameters are chosen to be free so that they resemble in value those characterizing real EAS events. The reason for choosing the Linsley functional form for this type of simulations is described in section 4.3.3 of this chapter (the Linsley analytical form is described in more detail in section 4.3.4). Noise is added to the Linsley density values in order to simulate fluctuations of real data. The EAS interaction with the detector stations is simulated only geometrically and the decision to register an interaction is taken randomly, according to pre-established conditions (for example it is possible to forbid interaction in certain detector stations). With this type of simulation it is possible to investigate the ability of the Linsley parameterization itself, since in this case it would have to reproduce (by fit) lateral particle density distributions that are distorted randomly starting from Lisley shapes. The purpose of this study is to understand the importance of different geometrical factors and to better tune the reconstruction procedure for full simulated and experimental showers. Therefore we shall refer to this particular investigation only to justify certain actions and decisions affecting the reconstruction of fully simulated and experimental showers. The detailed list of options available for running the toy Monte Carlo simulation program is revealed in the program input file which is presented in Appendix B.

4.2 Standard reconstruction strategy of KASCADE-Grande

In the standard reconstruction procedure that is performed for the KASCADE-Grande experiment, the general shower parameters are reconstructed from the array data following a procedure with three iterations:

1. In the first level of reconstruction the center of gravity of the registered energy deposits of the detectors first defines the shower core position (see Figure 4.1). The shower core coordinates at this stage are given by eq. 4.1:

$$X_{core} = \frac{\sum_{i=1}^{N} X_i E_i}{\sum_{i=1}^{N} E_i} \quad , \quad Y_{core} = \frac{\sum_{i=1}^{N} Y_i E_i}{\sum_{i=1}^{N} E_i} \tag{4.1}$$

where:
- X_{core}, Y_{core} are the coordinates of shower core in KASCADE-Grande coordinates;
- N is the number of triggered stations during the particular EAS event;
- X_i, Y_i are the KASCADE-Grande coordinates of the detector station i;
- E_i is the energy deposit registered in the detector station i.

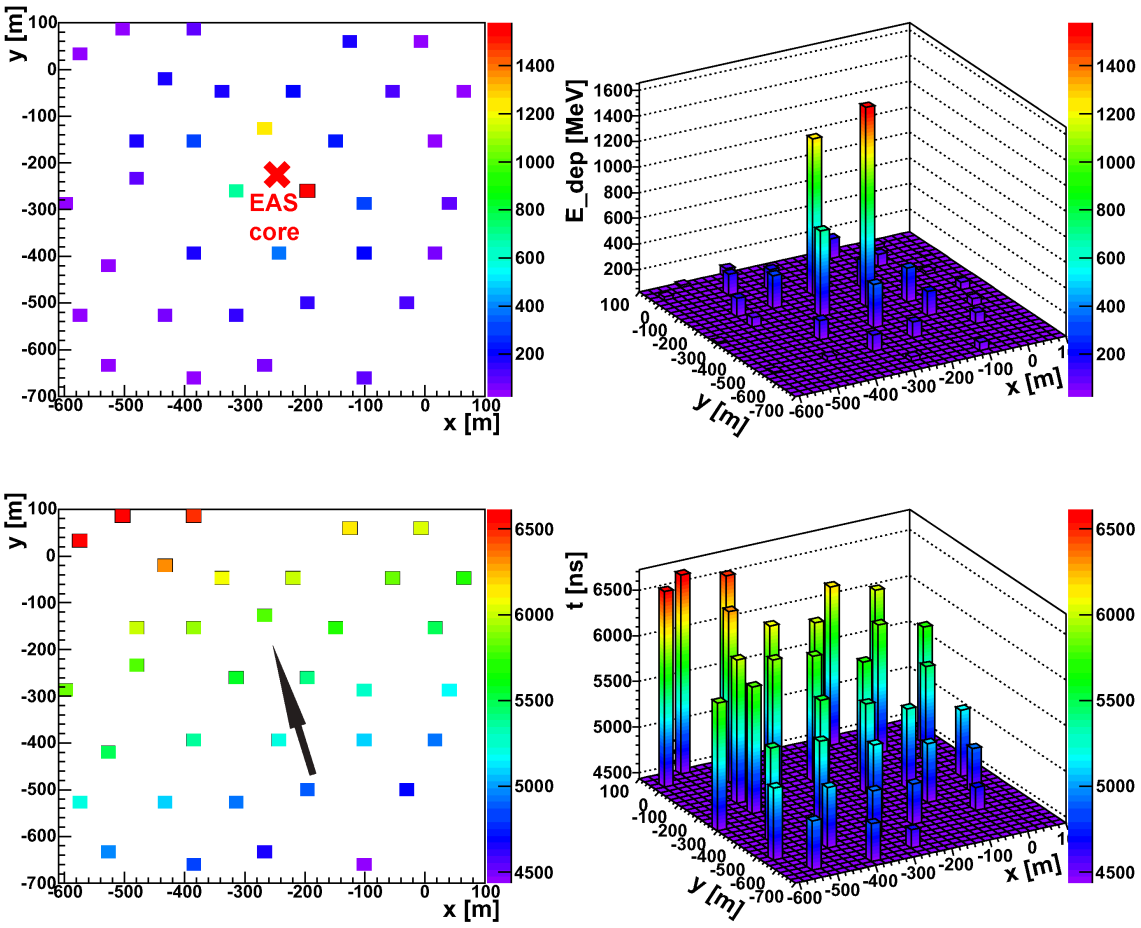

Figure 4.1: These diagrams represent the energy deposits of particles and the arrival times in each of the Grande stations for an experimentally recorded event: the energy deposits in detectors from a top-view perspective with the reconstructed shower core marked as the thick "X" (*upper left*), a 3D perspective representation of the value of energy deposits in stations (*upper right*), arrival times of particles in the Grande stations with the approximative arrival direction of the shower marked as the black arrow from a top-view perspective (*lower left*) and a 3D perspective representation of the value of arrival times in stations (*lower-right*, note in this case that the inclined shower front is visible in the sloped surface defined by the arrival times).

The direction of the shower is calculated from the arrival time distribution by assuming a plane shower front [87]. It should be noted here that the flat shower front is in fact a good approximation for smaller detector arrays where the curvature of the shower front (Figure 4.1) is not so obvious (a relevant example is the former top cluster array [60] installed on top of the KASCADE central detector). In the case of the KASCADE-Grande detector array however, the flat front approximation is only a preliminary result that serves as steering for further approximations in the subsequent iteration steps of the reconstruction. Assuming we have an air shower incident on a detector array triggering N_t detector stations, with known coordinates r_i=(x_i,y_i,z_i) and known arrival times of the first particle at each station t_i, the director cosines n=(n_x,n_y,n_z) of the vector normal to the plane passing through the corresponding detectors at corresponding times are calculated by imposing Gauss′s condition of minimum total distance from all points to the plane. When analyzing the time information the procedure ignores the stations with very early or very late arrival times and considers them uncorrelated with the event.

N_e and N_μ (the numbers of electrons and muons) are determined by summing up the relevant signals of $e^{+/-}$ and muon detectors. These signals are weighted with a geometrical dependent factor.

2. The approximations performed in this reconstruction step use the output of the previous level for steering purposes. Starting from iteration level 2 the reconstruction of the shower parameters is done in the shower coordinate system (in which the shower axis is parallel to the z axis). The lateral distribution of electrons in air showers up to 800 m radial range is approximated with a slightly modified NKG-function [88]:

$$\rho(r) = \frac{N_e}{2\pi \cdot r_0^2} \left(\frac{r}{r_0}\right)^{s-\alpha} \left(1+\frac{r}{r_0}\right)^{s-\beta} \frac{\Gamma(\beta-s)}{\Gamma(s-\alpha+2)\Gamma(\alpha+\beta-2-2s)} \quad (4.2)$$

where
N_e - the number of electrons;
s - the age parameter which describes the shape of the particle distribution and is theoretically related to the status of the longitudinal development (the age is a function of primary energy E_0, of atmospheric depth t, and of the critical energy E_c at which decays and energy loss processes become more probable than the production of secondary particles, eq. 4.3, [88]).

$$s = \frac{3t}{t + 2 \cdot log(E_0/E_c)} \quad (4.3)$$

r_0 - the Molière radius, defined within the multiple scattering theory (r_0=30);
r - distance(radius) from the EAS center [m];
α and β - two parameters (α=1.6 and β=3.4).
The shower arrival direction, core coordinates and electron number are all reevaluated and the improved results are used in the same reconstruction level for a better estimation of the muon number.

3. In this level the muon number reconstructed at level 2 is used in order to get a better estimate of the shower arrival direction, core coordinates and electron

number. With these, the muon number is again re-evaluated. Level 3 is the last iteration step of the standard reconstruction chain and from this moment the reconstructed observables are passed to further analyses.

For KASCADE the reconstruction of the EAS event included also the observables formerly measured by the central detector: lateral energy and angular distributions for hadrons and lateral, angular and temporal distributions for muons (with 490 MeV and 2.4 GeV energy thresholds, during the operational time of this particular detector).

The standard shower reconstruction is technically implemented in the KRETA code (**K**ASCADE **R**econstruction of **E**x**T**ensive **A**irshowers). The KRETA code includes also the calibration of the detectors. Simulated and experimental data are treated identically by this code. To bring both simulated and experimentally recorded EAS events to the same level of consistency, the CRES code (**C**osmic **R**ay **E**vent **S**imulation) is used for complex detector simulation, generating the detector response to the CORSIKA simulated EAS events. Shower data from CORSIKA (energy, position and incident angle of each particle hitting the detectors) are used as input of CRES. In principle, after the CRES treatment, the simulated data are on the same level of consistency as measured data, able to be compared. A schematic representation of the EAS analysis is shown in Figure 4.2.

In the case of the Grande detectors there is no information by the detector signals on the type of registered particle. In order to separate the information of the electron and muon components, an extrapolation of the two components, based on adequate anticipated lateral distribution functions, is performed from the radial ranges within the KASCADE array (where this information is separately available) to the radial ranges comparable to the Grande array [90]. This feature is one of the main differences between the standard procedure and the reconstruction by the SHOWREC code; SHOWREC does not disentangle the muon and electron components in Grande ranges and does not reconstruct muon information.

4.3 Reconstruction by SHOWREC

We stress here again that the KASCADE-Grande detector stations record the energy deposits of particles and the associated temporal information (arrival times of particles). The arrival direction, defined by the zenithal and azimuthal angles of the shower axis, is adopted from reconstruction by KRETA. As an auxiliary quantity for converting the energy deposits into particle densities **L**ateral **E**nergy **C**orrection **F**unctions (**LECF**) are introduced.

SHOWREC is reconstructing particle densities in the plane normal to the shower axis. For both experimental and simulated events, the information of particle density is given in the detector plane α (see fig. 4.3, from [91], [41]). The shower properties however are better revealed in the plane normal to shower axis, plane β (fig. 4.3). In order to map the shower properties from the detector plane α onto the plane β, special care must be taken in order to avoid distorting the information.

For an inclined shower, the particle density around the shower core at a given radial range can vary due to different particle absorption and scattering in the atmosphere. A relevant example is the case of particles propagating directly below the

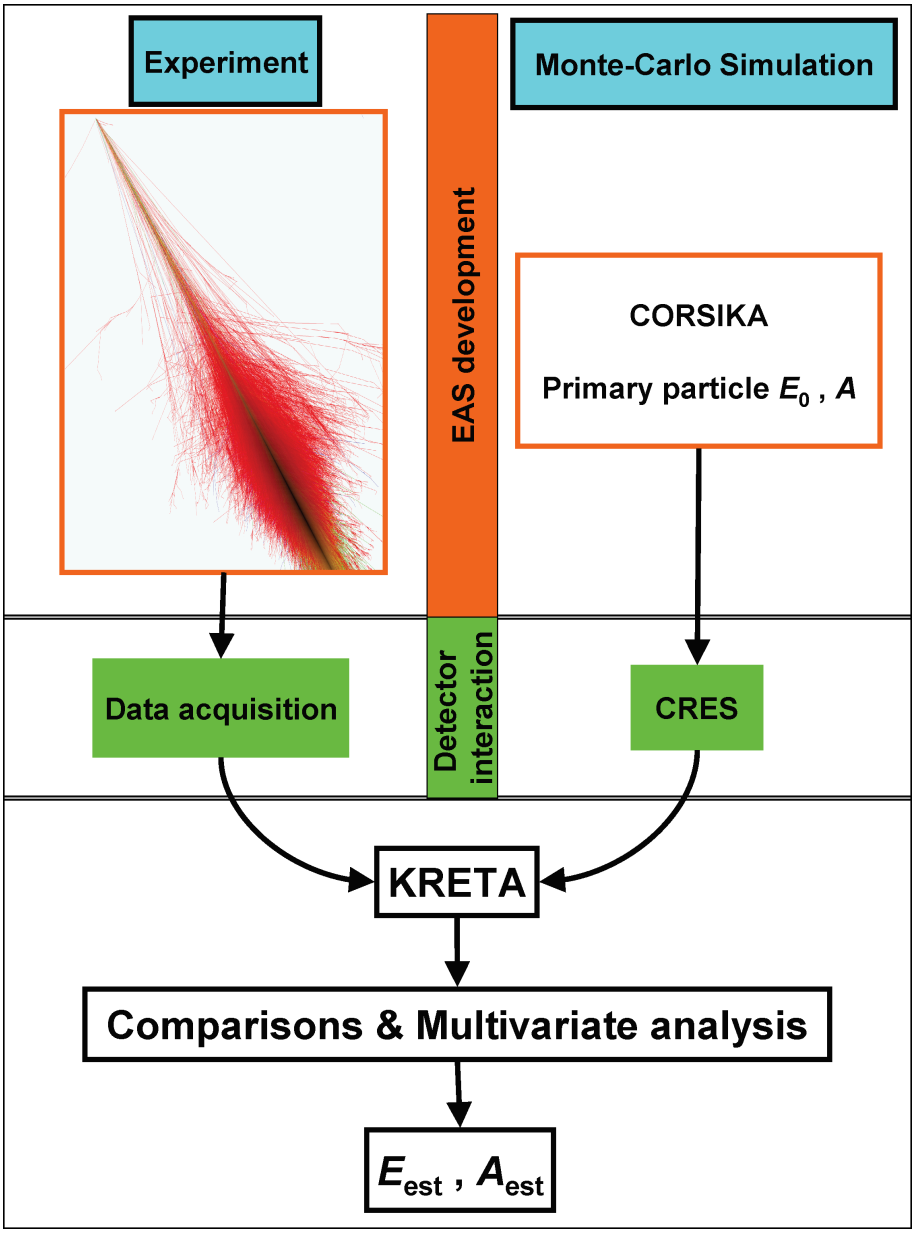

Figure 4.2: General analysis scheme of simulated and experimental EAS observables measured in the KASCADE-Grande experiment. Starting from KRETA, the processing is the same for both experimental and simulated events. On the experimental branch (*left*), the development of the EAS is presented as a vertical section through the EAS (from [89]).

shower axis, as opposed to those directly above the shower axis. Since the shower is inclined, the particles below the axis will travel a shorter distance through atmosphere before hitting the detectors (in position C for example as opposed to those hitting in position A, fig. 4.3). Furthermore, the angle of incidence of particles in detectors will be different in the two positions C and A which translates directly into different values for energy deposits (this is because the particles have a transversal momentum and do not propagate parallel to each other or to the shower axis). If the

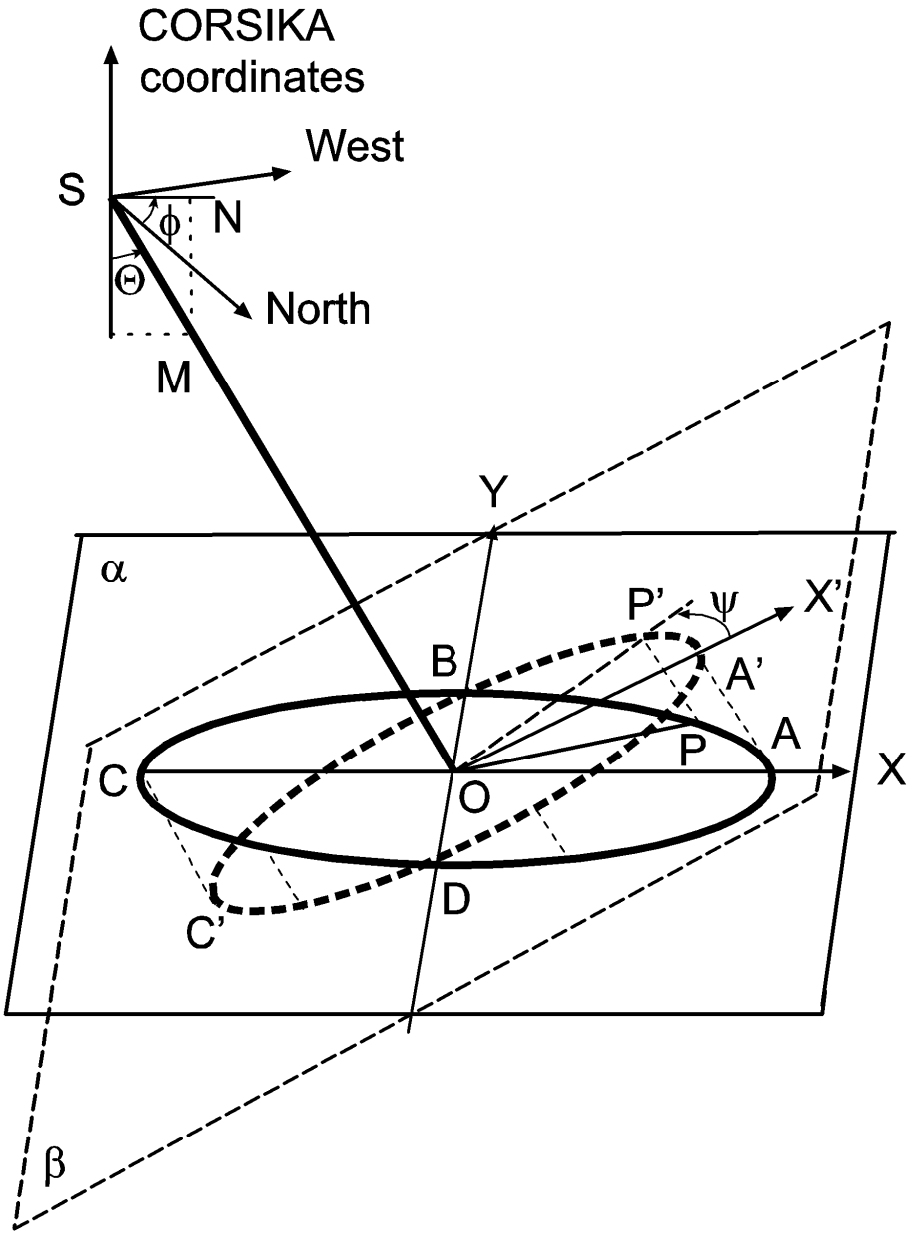

Figure 4.3: The coordinate system in the observation level (plane α) and in the shower coordinate system (plane β) (from [91], [41]).

information in plane α is simply projected onto the plane β, the resulting particle density distribution will be asymmetrical around the shower core (the density along

the path DC'B will be greater than the one on the path DA'B). If detectors are placed predominantly under the shower axis, the particle density would be overestimated (following that in the opposite case the density would be underestimated). The error in the density influences both the reconstructed shower size and the accuracy of shower core reconstruction. A procedure for attenuation correction has therefore been introduced in order to compensate for the effects induced by inclined showers. Furthermore, the dependence of energy deposits with the angle of incidence of particles is also taken into account (as it will be shown in the following subsection).

Therefore in the CRES code a complex detector simulation (using GEANT) calculates first the energy deposits of EAS particles registered in the detectors and defines the LECF functions. The calculation of the LECF with various steps of necessary refinements is a most important step in the reconstruction procedure. The LECF functions are dependent on the shower zenith angle as they take into account the fact that more inclined particles will deposit more energy in detectors due to their longer cross path.

As in the case of the standard reconstruction, the SHOWREC reconstruction functions as a standalone program in an identical fashion for both simulated and experimental events. SHOWREC uses also collected data from the output files of KRETA in order to make comparisons between own results and the results of the standard reconstruction. In fact, in the output of SHOWREC is stored more data than that used in this study. The variable flow in SHOWREC is intuitively depicted in Appendix C.

4.3.1 LECF functions

LECF functions provide the mean energy deposit of charged particles as a function of EAS incidence angle and of different radial distances from the shower core. Therefore, to obtain the LECF, one has to have a very clear understanding how different particle types are interacting with the detector in different situations (incidence angles and energies). For this, the energy deposits of particles in detectors are simulated, and with these deposits a mean energy deposit per particle is subsequently calculated (also by use of adequately defined detector sensitivity functions to various particles). Thus by dividing the total (experimental or simulated) energy deposit with the mean energy deposit per particle one can deduce the number of particles impinging on the detector. For the case of a Grande station, calculating particle density is achieved by dividing by the sensitive area (10 m^2) of the detector.

The detailed simulation of particle interactions in the detector medium is performed with the GEANT package from CERN. In the standard procedure the EAS particles simulated with CORSIKA are fed into the GEANT program and the energy deposited in the detectors is simulated for each event. That is, in the standard procedure for each shower and for each secondary particle reaching the detectors the GEANT simulation is repeated. Such GEANT simulations are time consuming and contribute significantly to the total analysis time. Because the energy deposit of a given registered particle in the detector depends only on the particle properties (type, energy, trajectory through the detector) and not on primary shower properties, it is obviously not necessary to repeat the GEANT simulations again for each

single shower, if the energy deposit can be parameterized as a function of EAS particle type, energy, angle of incidence in the detector.

Hence parameterized functions which adequately represent the realistic simulations by GEANT of the energy deposit in the detectors by various particle types (e, γ, μ, p and n) as a function of energy and incidence angle, are consequently constructed. Using these functions, a very fast simulation of the energy deposit can be achieved [93]. For this study, only the scintillator plate of the Grande stations is considered for simulation with GEANT, while the metal hut and the concrete base are momentarily ignored.

The energy deposits are calculated using the GEANT code for the layout and structure of the KASCADE-Grande stations (plastic scintillator detectors). The particles that are studied are photons, electrons, muons, protons and neutrons with incidence angles between 0° and 80° degrees and energies up to $5{\cdot}10^4$ GeV, (the contribution of particles with higher energy, not very close to the core, is very small and moreover, the distribution of the energy deposit in the detectors changes very slowly with incident energy above this limit). All the distributions are obtained from a sample of 200.000 to 1.000.000 particles. The incident energy and angle play a crucial role in the shape of the energy deposit distribution and this can also be observed in the selection of comparative plots presented below. The simulated energy deposit spectra are parameterized for different particle species, energies and angles of incidence, as will be described in the following subsection.

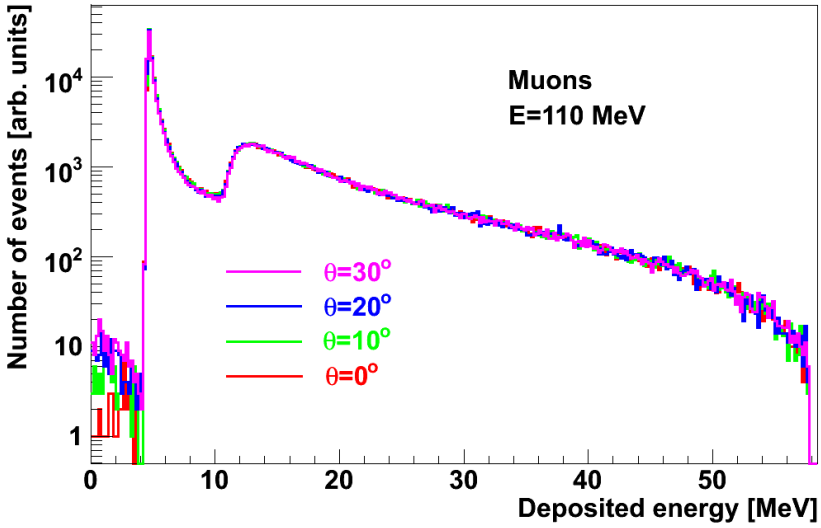

Figure 4.4: Energy deposit distribution for muons at the same incident energy and various low angles of incidence. *(G. Toma et al. - KASCADE-Grande Collaboration, Proc. 26th ECRS 2006, Lisbon, so-134)*

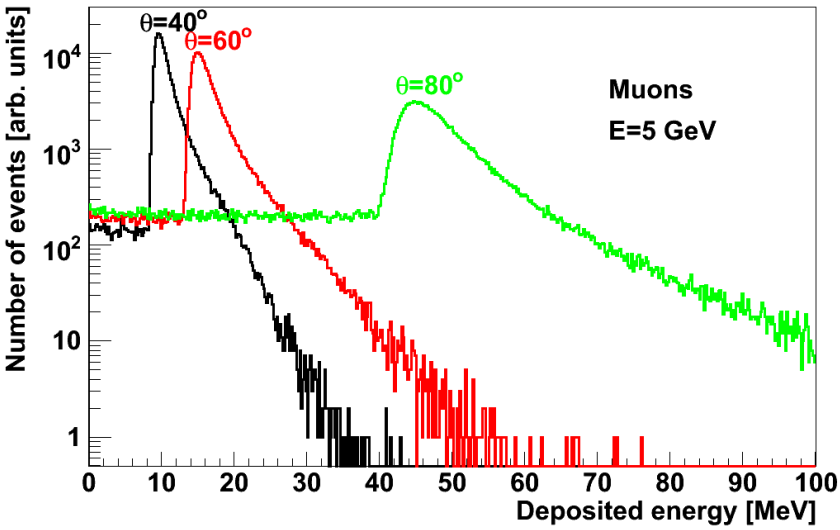

Figure 4.5: Energy deposit distribution for muons (same incident energy, various high angles of incidence).

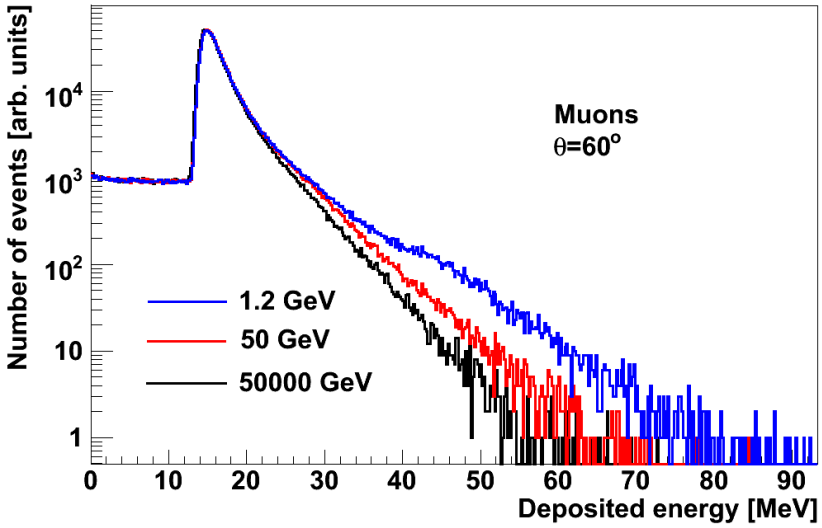

Figure 4.6: Energy deposit distribution for muons (same angle of incidence, various incident energies); in the case of muons, the shape of the energy deposit distribution changes only very slowly with the increase of incident energy.

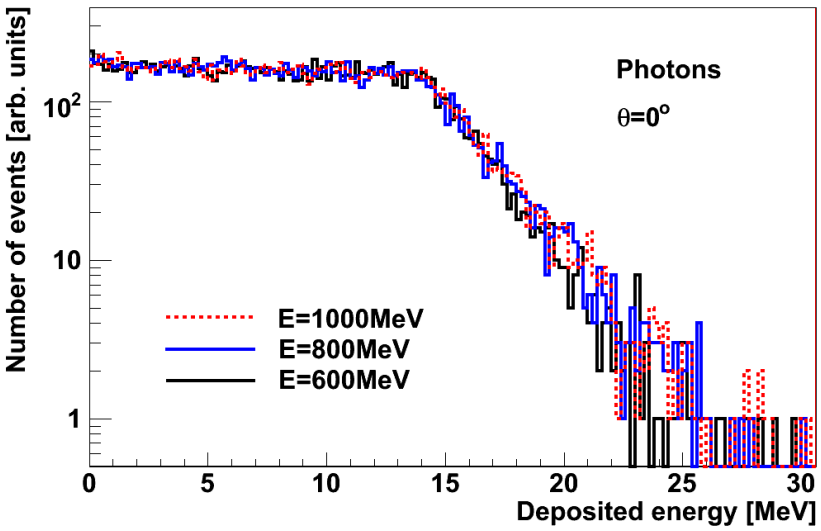

Figure 4.7: Energy deposit distributions for photons; there is little energy dependence for very high incident energies.

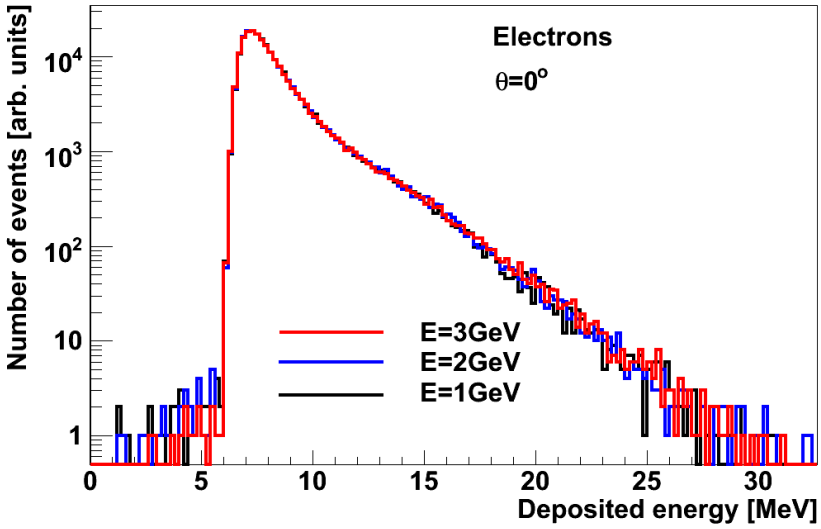

Figure 4.8: Energy deposit distribution for electrons; at high incident energies there is little energy dependence.

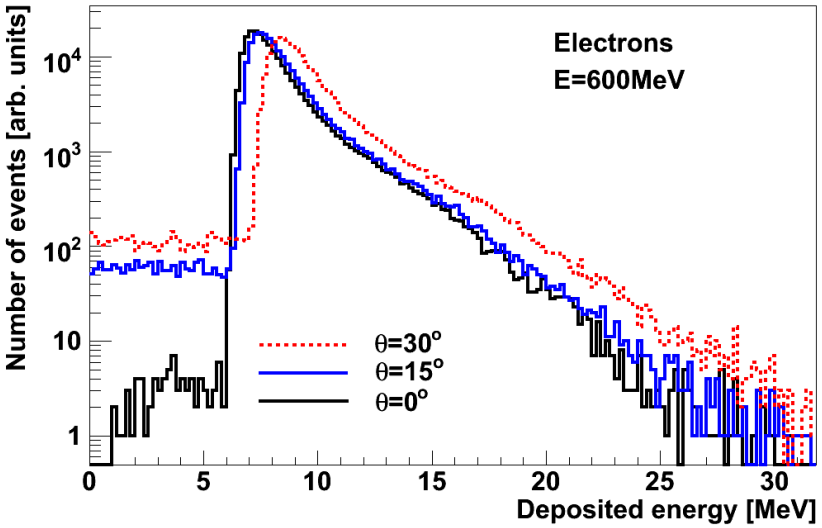

Figure 4.9: Energy deposit distribution for electrons (different incident angles); at high incident energies the dependence on the angle of incidence is still noticeable.

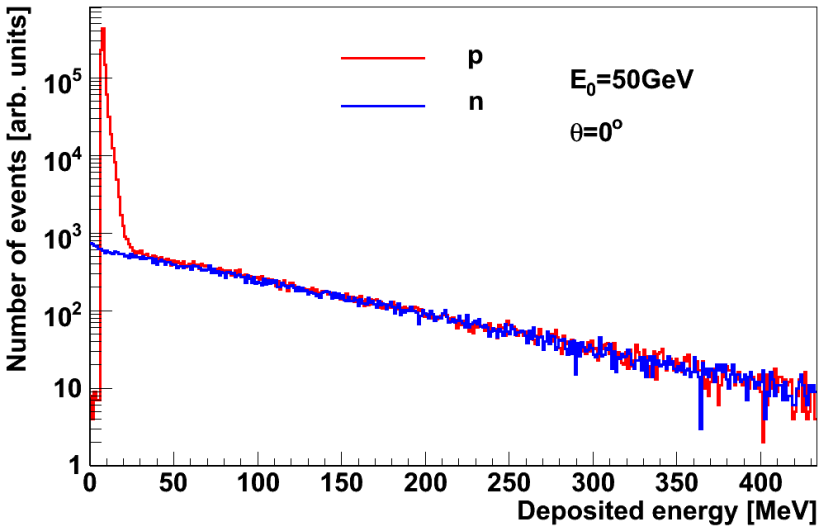

Figure 4.10: Energy deposit distributions for neutrons and protons at the same energy and angle of incidence (note that the only difference between the two is the ionization peak of protons, since they are charged particles).

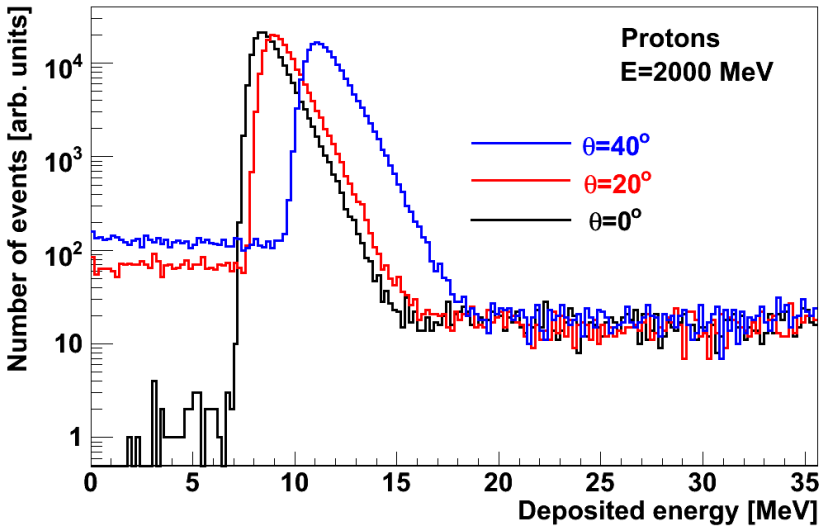

Figure 4.11: Energy deposit distribution for protons (different incident angles).

The interaction of relativistic EAS particles with the detector medium (plastic scintillator) presents several features of interest (visible also in plots 4.4-4.11) [94]:

- All charged relativistic particles will interact with the detector medium in a similar fashion (their type or energy play a limited role in changing the shape of the main spectral features of the energy deposit). When crossing the detector they lose a minimum amount of energy by ionization (they are **m**inimum **i**onization **p**articles, **mip**'s). This energy loss amounts for few MeV for every cm of particle track length in the material (the total energy loss is therefore dependent on the particle track length). In the energy deposit spectrum this effect is visible as a Landau-shaped minimum ionization peak. For charged incident particles the mip peaks are the most prominent features of the spectra and have a maximum in the ∼10 MeV range (see plots 4.5, 4.6, 4.8, 4.9 and 4.11). For a given particle type, the position of the mip peak remains practically unchanged when changing the incident energy (see plots 4.6 and 4.8).

- For higher angles of incidence the particle track length in the scintillator material is increased and therefore the energy loss of charged particles by ionization is greater along the entire track. We observe this in the shifting of the mip peaks towards higher energies (i.e. larger energy deposits) for increasing angles of incidence at the same incident energy (see plots 4.5, 4.9 and 4.11).

- In the case of protons, the interactions can lead to nuclear reactions and the creation of various secondaries that will in turn deposit energy in the scintillator. This leads to the extension of the proton energy deposit spectrum to much higher energies (figures 4.16 and 4.10) when compared to the spectra of other charged particles (figures 4.6 and 4.8).

- Neutral particles do not produce direct ionizations and therefore the shapes of their spectra differ from those of charged particles. Photons interact predominantly by Compton scattering and pair production. Secondary electrons are produced and get attenuated (visible as an exponential tail extending the photon spectra towards higher energies - see figure 4.7). In fact secondary electrons are produced also by charged incident particles (note the exponential tails of spectra in figures 4.6 and 4.8).

- Neutrons will interact similarly with protons, but will not produce direct ionizations since they are neutral. This means that the spectrum of deposited energy for neutrons will be similar to the one for protons but will miss the mip peak (figure 4.10).

4.3.2 Parameterization of energy deposits

By just inspecting the shape of the simulated energy deposit distributions one can guess that in fact each complex distribution is approximately composed of some more simply shaped distributions such as uniform, linear, exponential, Landau or Gauss. Thus it appears to be possible to develop a procedure that would generate random variables by a complex distribution not by simulating every interaction by the GEANT code, but by simply generating random variables distributed by some simpler random distributions with given parameters and specific weights and then adding them to create the complex distribution. The weighting of a certain spectrum region or feature is done through integration of the respective simulated spectral feature so that the resulting parameter-generated spectrum has not only the same features but also every parameterized feature has the same weight as in the GEANT simulated spectrum. This procedure (that is in fact often applied in Monte Carlo investigations) is known as the method of decomposition for the simulation of a random variable [95]. Figure 4.12 shows how a complex energy deposit distribution is split into simpler distributions to get easily parameterized.

In order to develop a procedure useful for any given incident particle with any given incident energy and incidence angle, all the relevant cases have to be simulated. Then the energy deposit distributions must be split into simpler distributions that are then parameterized by the incidence angle and energy. A simple procedure would then interpolate the parameter values for any angle of incidence and energy making it possible to generate energy deposits with the same complex distribution as the simulated one, with negligible decrease of reconstruction quality.

This procedure is tremendously faster than using GEANT simulations. Instead of repeatedly invoking the GEANT procedure, in this case simulations are performed only once. The distributions are parameterized and parameter tables are obtained for all particles, for the studied incident angles and energies. Subsequently, only simple interpolations and basic distributions have to be generated for each event. This procedure results in an increase of speed by a factor of 100 to 1000 depending on the particle type (for example, charged particles electrons, protons - take much longer to simulate by GEANT while as the speed of the new procedure is not affected by the particle type).

We shortly compare the simulated energy deposit distributions with that

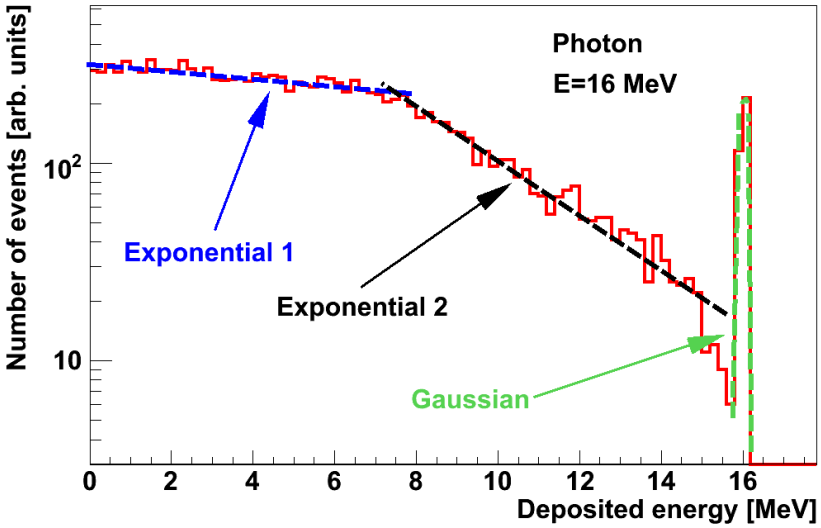

Figure 4.12: Complex energy deposit distribution for photons decomposed into regions with simpler distributions that are easily parameterized.

ones obtained from the parameterizations by simpler distributions. Some graphical examples are displayed for different particle types, angles of incidence and energies just showing the superimposed parameterized distribution with the simulated ones (Figures 4.13 - 4.16). After the parameterization of energy deposit distributions, energy deposits of particles are randomly generated event by event accordingly to the parameterization and the resulting spectrum of the deposited energy is presented with continuous lines. GEANT simulations are presented in dotted lines.

The technique of parameterized energy deposit distributions is able to replicate the energy deposit distributions with a satisfying accuracy for randomly given energies and angles of incidence, at the same time providing a considerable boost to the speed of the procedure.

4.3.3 Parameterizations of the lateral particle density distribution

For the case of a simple EAS simulation, when no detector simulation is performed, all particles in the EAS are known along with their incidence position and momentum. In this case, calculating the particle density at any given radial range can be done easily by simply counting the particle number in a given area (provided that atmospheric absorption and azimuthal corrections for inclined showers are performed). When performing a full detector simulation however, or similarly in the case of experimental events, the reconstruction will have only a limited number of radial ranges at disposal where particle densities are known. These ranges correspond to the radial distance of detector stations to shower core. In the case of KASCADE-Grande we will always have at best 37 positions corresponding to the

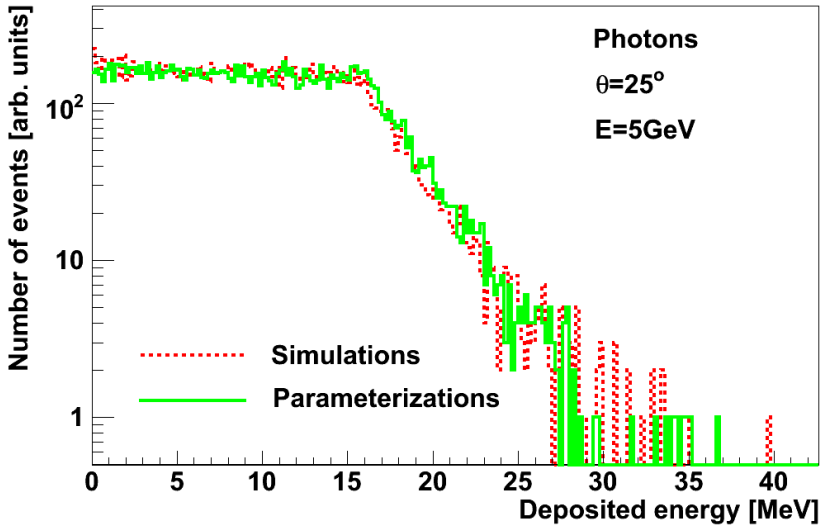

Figure 4.13: Energy deposit distributions for photons.*(G. Toma et al. - KASCADE-Grande Collaboration, 26th ECRS 2006, Lisbon, Portugal)*

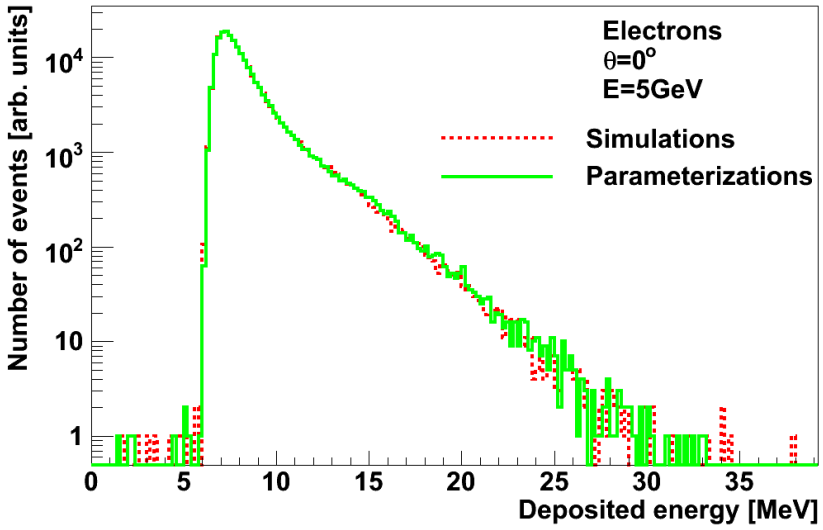

Figure 4.14: Energy deposit distributions for electron.

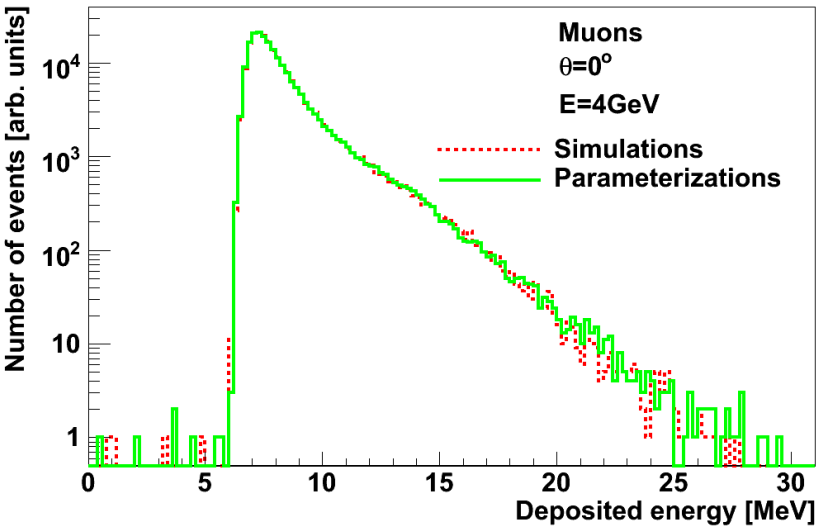

Figure 4.15: Energy deposit distributions for muons.

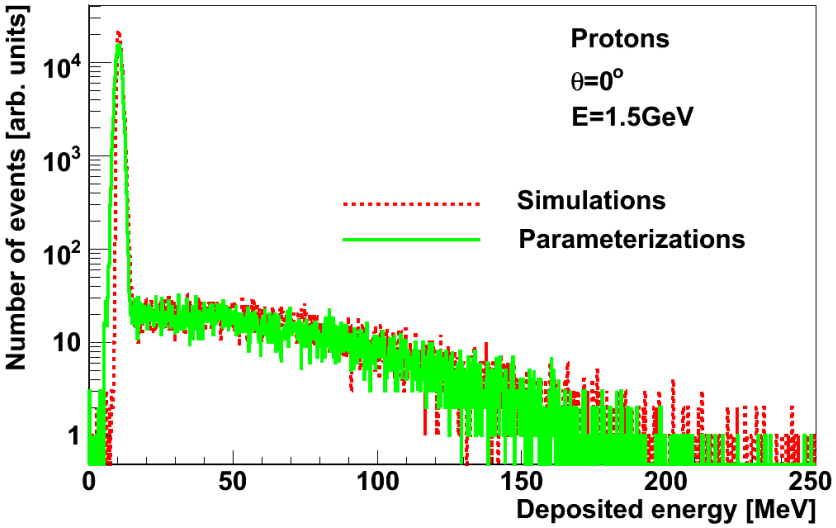

Figure 4.16: Energy deposit distributions for protons.

37 detector stations. Therefore, to reconstruct the particle density at an arbitrary range, one has to approximate the lateral particle density distribution with an anticipated parameterization. In the developing stages of SHOWREC, four candidates were considered for a Lateral Density Function (LDF): the NKG [96], the Lagutin form [97], a polynomial parametrization [98] and a parameterization introduced by Linsley [44]. All four parameterizations are subjected to quality tests in order to establish which one may be best suited to describe the lateral particle density distribution in the framework of this study [40, 41]. These parameterizations are briefly presented below, with emphasis (subsection 4.3.4) on the description of the Linsley form which ultimately was considered as the most appropriate for the purpose of this study:

- The Nishimura-Kamata-Greisen (NKG) form [84]:

$$\rho_{ch}(r) = \frac{N}{2\pi r_0^2} \cdot C \cdot \left(\frac{r}{r_0}\right)^{s-2} \cdot \left(1 + \frac{r}{r_0}\right)^{s-4.5} \tag{4.4}$$

  where

$$C = \Gamma(4.5 - s)/\Gamma(s)\Gamma(4.5 - 2s) \tag{4.5}$$

  and
  ρ_{ch}(r) - charged particle density at distance r[m] from shower core;
  N - the total number of charged EAS particles;
  s - the age parameter which describes the shape of the particle distribution and is theoretically related to the status of the longitudinal development;
  r_0 - the Molière radius, defined within the multiple scattering theory, ≈79 m at sea level (atmospheric thickness of 1033 g·cm^{-2});
  r - distance(radius) from the EAS center [m].

  This parameterization has been widely used in many experiments in order to describe electron and charged particle lateral distributions and was adopted from theoretical assumptions for a purely electromagnetic shower. Therefore NKG is only approximately appropriate for hadronic showers. The NKG function is implemented in the standard reconstruction chain at KASCADE-Grande.

- The Lagutin form [97]:

$$\rho_{ch}(r) = \frac{0.28 \cdot N}{r_0^2} \left(\frac{r}{r_0}\right)^{p1} \left(1 + \frac{r}{r_0}\right)^{p2} \left[1 + \left(\frac{r}{10 \cdot r_0}\right)^2\right]^{p3} \tag{4.6}$$

  where:
  ρ_{ch}(r) - charged particle density at distance r[m] from shower core;
  N - shower size (in this case the total number of charged particles);
  r_0 - Molière type radius [m];
  r - radius [m];
  p_1, p_2, p_3 - three fit parameters.

- The Polynomial form [98]:

$$\rho_{ch}(r) = \frac{N}{2\pi \cdot r_0^2} \cdot 10^{(C_0 + C_1 \cdot X + C_2 \cdot X^2 + C_3 \cdot X^3)} \tag{4.7}$$

where:

$$X = lg\left(\frac{r}{r_0}\right) \tag{4.8}$$

and
ρ_{ch}(r) - charged particle density at distance r[m] from shower core;
N - shower size (in this case the total number of charged particles);
r_0 - Molière type radius [m];
r - radius [m];
C_0, C_1, C_2, C_3 - four fit parameters.

- The Linsley form [44]:

$$\rho_{ch}(r) = \frac{N}{r_0^2} \cdot C(\alpha,\eta) \cdot \left(\frac{r}{r_0}\right)^{-\alpha} \cdot \left(1+\frac{r}{r_0}\right)^{-(\eta-\alpha)} \tag{4.9}$$

where:

$$C(\alpha,\eta) = \Gamma(\eta-\alpha)\left[2\cdot\pi\Gamma(2-\alpha)\Gamma(\eta-2)\right]^{-1} \tag{4.10}$$

and
ρ_{ch}(r) - charged particle density at distance r[m] from shower core;
N - shower size (in this case the total number of charged particles);
r_0 - Molière type radius [m];
r - radius [m];
α,η - two shape parameters.

We have shown that the above mentioned parameterizations can be used to describe the shape of the true charge particle density, ρ(r) as given by simulations. The reconstructed particle density S(r) available after the simulation of the detector response or recorded experimentally is parameterized similarly with the real particle density by the same formulae.

In order to understand which of these parameterizations is best suited for the reconstruction procedure, several tests are performed in order to comparatively evaluate the quality of reconstructions obtained with each function [91]. CORSIKA simulated showers are used in these tests. H, C and Fe primaries are considered in various primary energy ranges between (1.00-1.78)·10^{16} eV up to (5.62·10^{17}-1.00·10^{18}) eV. The angles of incidence are selected randomly. For a given primary type in a given primary energy range the events are averaged. The averaged true particle densities as given by CORSIKA $<\rho_{ch}(r)>$ are compared to the ones obtained from LDF approximations of lateral densities, S_{fit}(r). The true densities of each shower are then distorted (with SHOWREC) by simulating detectors response and a reconstructed density S(r) is obtained. Reconstructed events are averaged also and the averaged reconstructed densities <S(r)> are again compared with values resulted from LDF approximations. For comparison, two quality parameters are defined and calculated:

$$<Q_\rho> = \frac{< S_{fit}(r)> - <\rho_{ch}(r)>}{<\rho_{ch}(r)>} \tag{4.11}$$

$$<Q_S> = \frac{< S_{fit}(r)> - < S(r)>}{< S(r)>} \tag{4.12}$$

The fits of the LDF approximations are performed on different radial ranges: 300 m - 700 m and 40 m - 700 m (the lower limit of 40 m radial range is set in order to avoid performing reconstructions on data very close to shower core, where particle densities are very high and there is a high risk of detector stations being over-flooded leading to unreliable data). The comparative plots [91] are presented in detail in Appendix D. These plots show that the reconstruction is most stable when fitting the lateral distribution on extended ranges. When compared with the other parameterizations, the Linsley function is most accurate in describing the lateral particle density distribution (followed closely by the Lagutin form). The Linsley form gives consistently better results for fits on restricted radial ranges as well as for the fits on extended radial ranges. The NKG and polynomial forms perform well on restricted radial ranges but give larger deviations from the true data when fitting extended radial ranges. Therefore the Linsley form is adopted for future use in this study. Figure 4.17 shows Linsley approximations of true averaged CORSIKA showers and of the resulting reconstructed lateral densities.

Figure 4.18 shows the variation of the reconstruction quality with the primary energy, when performing reconstructions of data close to 500 m distance to shower core (the $S(500)$ and the charged particle number in the 400 m - 600 m radial range are reconstructed). The fit quality is better for higher energies. One of the

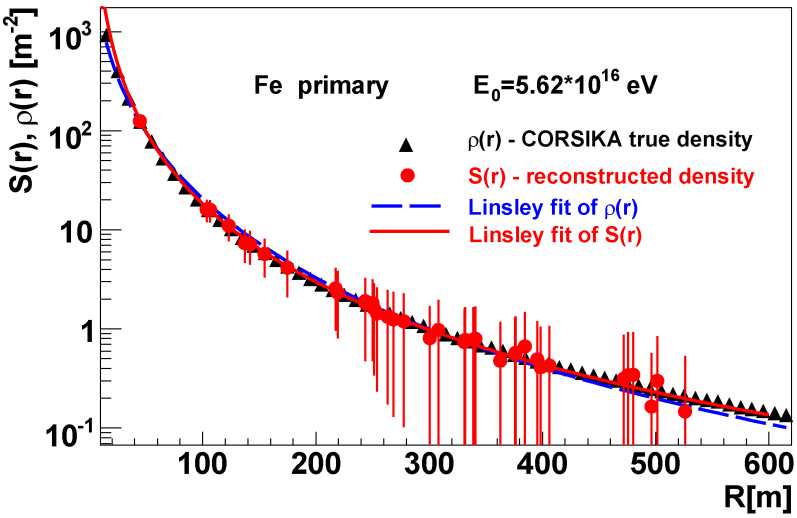

Figure 4.17: In this example, the results of the described SHOWREC reconstruction are presented; the initial ρ_{ch}(r) distribution (true charged particle lateral distribution) is compared with the reconstructed S(r) (resulting after EAS-detector interaction simulations and conversion of energy deposit into particle number with the help of LECF).

reasons is the increased accuracy of the core reconstruction. The higher probability of having lower reconstructed density at large distances from the core and the fact that such densities have also lower values of σ^2 tend to bias the fits to lower values at large distances from the core at low energies. It is also possible that for smaller

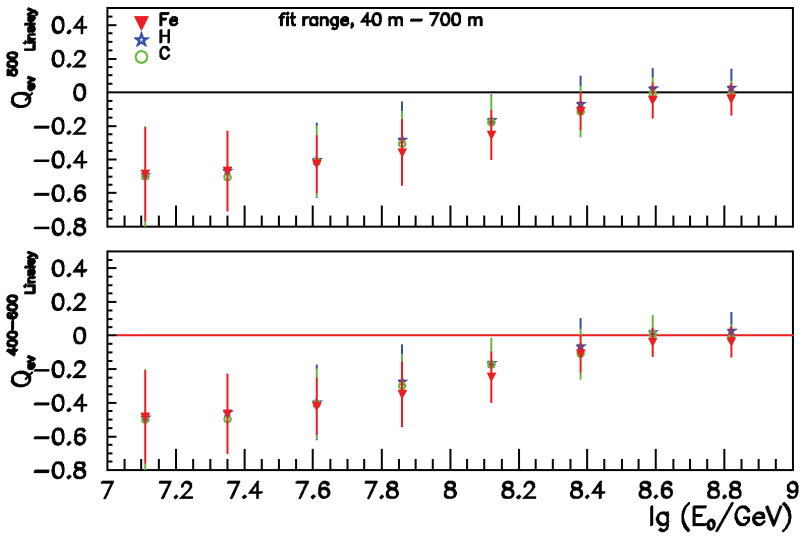

Figure 4.18: Averaged event reconstruction quality Q_{ev} for S_{500} and $N_{ch}^{400-600}$ (number of charged particles in the 400 m - 600 m radial range) using Linsley type of LDF. (from [91])

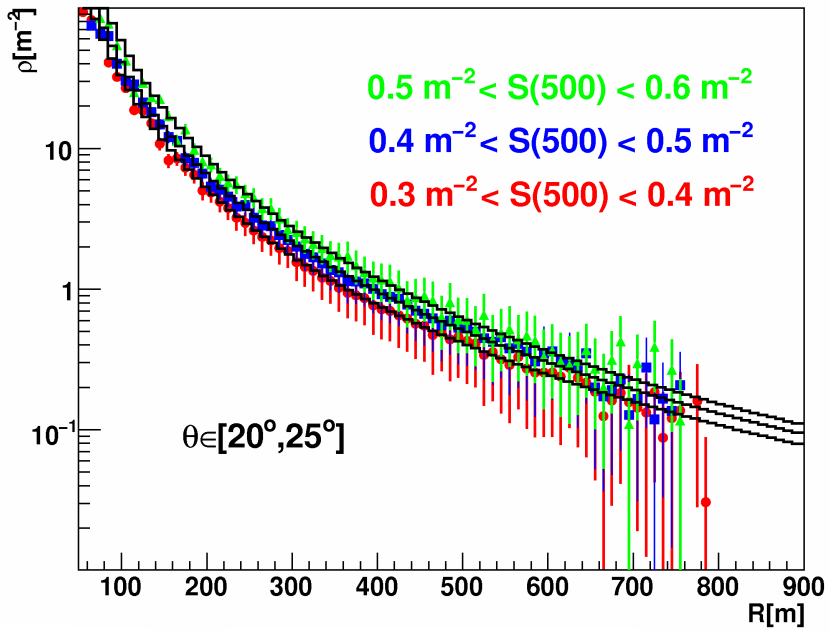

Figure 4.19: Averaged lateral density distributions of experimentally recorded EAS samples for three $S(500)$ ranges with Linsley fits($\theta \in [20°,25°]$).*(G. Toma et al. - KASCADE-Grande collaboration, DPG Frühjahrstagung 3-7 March 2008, Freiburg, Germany)*

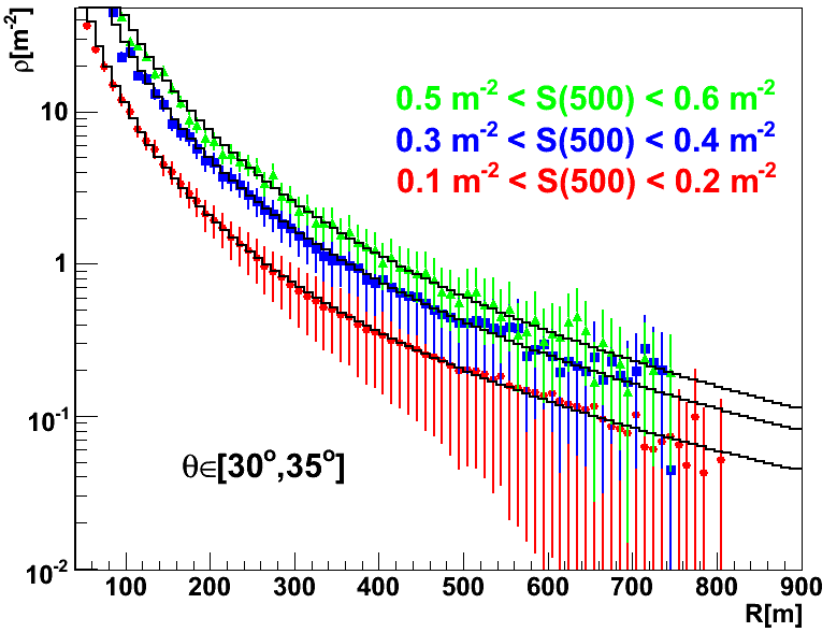

Figure 4.20: Averaged lateral density distributions of experimentally recorded EAS samples for three $S(500)$ ranges with Linsley fits($\theta \in [30°,35°]$).

energies, the EAS does not trigger stations at large radial ranges (close to 500 m) and the fit function describes only the data close to shower core (where the lateral density is much steeper, a feature that by extrapolation leads to underestimation of data at large radial ranges). The findings of these tests will have an impact in establishing relevant quality cuts used for selecting showers in the next chapters. Thus for the reconstruction of $S(500)$ the method is expected to give reliable results for large events triggering a considerable number of stations (with information at large radial ranges) and for LDF approximations starting from ranges close to shower core (40 m) up to the highest ranges available. The reconstruction has the tendency to underestimate the values of $S(500)$ for small events (low primary energies). Similar conclusions will be derived from the investigations on toy Monte Carlo simulations as described in subsection 4.3.5.

Figure 4.19 shows averaged lateral density distributions of experimentally recorded EAS samples for three $S(500)$ ranges and zenith angle θ in the [20°, 25°] range (the event selection procedure will be described in detail in Chapter 5). A two step procedure has been employed in order to construct this plot: first, the $S(500)$ value is reconstructed and stored for each detected event. Next, by reading the previously built $S(500)$ database, showers are selected and organized into three sub-samples according to their previously reconstructed $S(500)$ value. The density distributions of events in each sample is averaged and then fitted with a Linsley LDF (continuous lines). We stress here that in the second step, when building the averaged events, the true recorded data is averaged, and not the previously fitted values. The first Linsley fit has only the purpose of classifying the events according

to their $S(500)$ value. The Linsley fit reproduces accurately the averaged experimental lateral density distribution. Similarly as in fig. 4.19, in fig. 4.20 is shown the case of EAS events with $\theta \in [30°,35°]$.

4.3.4 The Linsley parameterization

The Linsley parameterization is a three parameter function. While the normalization factor N is an estimator of the shower size, the two parameters α and η describe the shape of the function and therefore are called shape parameters. The α parameter describes the steep part of the lateral distribution closer to shower core while the η parameter describes the distribution at large radial ranges. The steep part of lateral density distribution is expected to exhibit mass sensitivity [92]. This implies that also the η parameter should be sensitive to the mass of the primary particle.

In order to better understand how the three parameters describe the func-

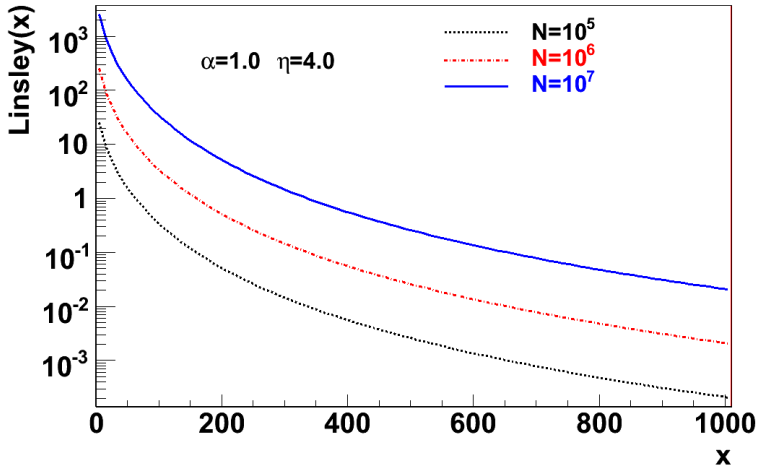

Figure 4.21: Variation of the shape of the Linsley function for different values of the N parameter (α and η parameters are fixed).*(G. Toma, private communications of the KASCADE-Grande collaboration, 2008)*

tion shape, a pure mathematical investigation is performed in which each parameter takes different values while the others remain fixed (figures 4.21-4.23). When fixing parameters or giving them variable values, such values are considered that the resulting value of the Linsley function resemble the values of particle densities in EAS events. Thus, for N three values are considered, 10^5, 10^6 and 10^7 since N should be an estimator of the shower size (N_{ch}). For α and η parameters the following intervals of variation are studied: $\alpha \in [0,2)$ and $\eta \in (2,12]$. It should be noted here that choosing the value 2 as upper and lower limit for α and η intervals of variation is the result of the Linsley analytical structure. The Gamma function has poles in 0 and, for the considered functional arguments, this translates directly in the Linsley function having poles for α=2, η=2 and α=η. As a result of all these, α is always

less than 2 while the η parameter will always have a value greater than 2.

Another feature of interest in the Linsley functional form is the presence of a ratio of Gamma functions. When close to poles, the ratio of Gamma functions could lead to large variations of the Linsley function and subsequently to instability of the fit routine. This can happen for certain poor quality lateral distribution (affected by large fluctuations and/or with many missing stations, e.g. the case of some small showers). In such cases it is possible that the Linsley minimization routine will find poor solutions by falling into minima created by shape parameters close to the limits. This points towards the necessity of a more in depth investigation of the ability of the Linsley fit routine to properly describe a lateral distribution. The special case of poor fits should be investigated in order to find solutions to improve the fit quality on one hand and on the other hand to more easily identify the events prone to yield poor reconstruction (and to eliminate them from the shower sample by the use of properly defined quality cuts). Such an investigation is presented in the next sub-section.

Figure 4.24 shows the effects of α and η variations on the values of the Linsley function calculated for the particular argument x=500 (fixed N=10^5). This plot suggests that the value of the Linsley function is most sensitive to variations of the η parameter. η variation alone inside the considered range can change the value Linsley(500) with ∼5 to ∼8 orders of magnitude depending on the value of α; in contrast, the greatest variation in Linsley(500) induced by the variation of α is only ∼4 orders of magnitude.

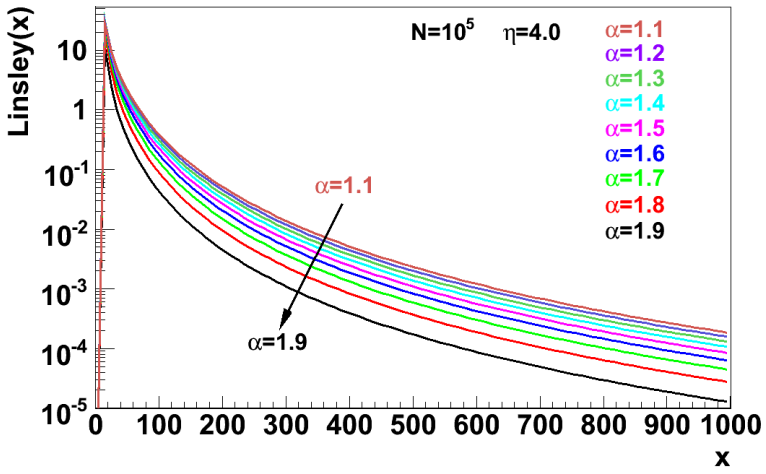

Figure 4.22: Variation of the shape of the Linsley function for different values of the α parameter (N and η parameters are fixed with values specified on the plot); the function value decreases with increasing values of α so that the maximum variation around x=500 is of ≈1 order of magnitude.

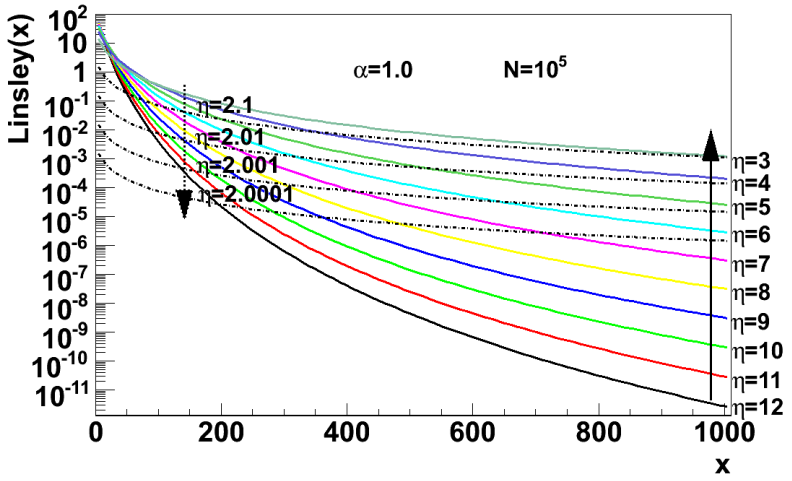

Figure 4.23: Variation of the shape of the Linsley function for different values of the η parameter (α and N parameters are fixed as indicated in the plot); the Linsley variation with the η parameter is not uniform and, for values close to the lower limit (η=2) the variation of the function abruptly changes from increasing to decreasing and it is also described by significantly reduced steepness; generally however, for η values far from the pole in 2, the function value decreases with increasing values of η so that the maximum variation around x=500 is of ≈6 orders of magnitude.

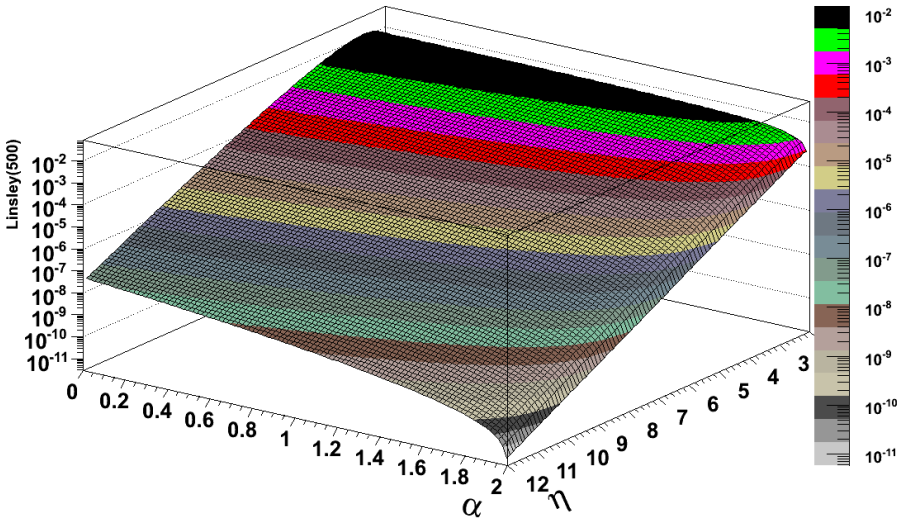

Figure 4.24: Linsley(500) for different α and η values in the considered intervals (N is fixed at N=10^5).

4.3.5 Reconstruction efficiency from toy Monte Carlo

Before proceeding to the reconstruction of full simulated and experimental events, we have to evaluate the ability of the Linsley minimization routine to properly describe the lateral density distribution. We have already investigated the possibility of using the Linsley function for this purpose (subsections 4.3.3 and 4.3.4) and found that the Linsley function describes well the lateral particle density distribution, but we want to further understand what are the limits that ensure a good reconstruction. Thus, we will investigate mainly the effects of data fluctuation, radial fit range variation and also the effects of missing stations in the fit. We will use a toy Monte Carlo test as described previously in subsection 4.1.2 of this chapter. The tests consists in fits of lateral distributions that are generated randomly as values of a Linsley function with random parameters. We compare the true value of the Linsley function (noted with ρ) with the value reconstructed by the fit (noted with S). Ideally, since both the data to be fitted and the fit function are the same type of function we should have very good agreement between the true value and the fit value. However we will artificially introduce fluctuations in the data and we shall also exclude certain stations from the fit so that there will be no data available for the fit inside certain radial ranges. Additionally, we will use various fit ranges in order to see how this affects the fit quality.

The lateral density distribution of an EAS has two main regions: a very steep region close to shower core, where the particle density decreases several orders of magnitude very quickly (below 200 m), followed by a shallow part at larger radial distances in which the particle density decreases only very slowly. The minimization routine must find only one set of parameters that describes accurately both parts of the distribution. In order to better steer the fit towards a correct result (in what concerns the reconstruction at $\approx$500 m range) we could fit only the data far from shower core and thus get a fairly good description of the data in this range at the expense of poor reconstructions for ranges closer to shower core (this would not affect the quality of the study since we are only interested in the reconstruction of $S(500)$). This decision however, convenient as it might sound from the mathematical point of view, is risky when applied to real data. This comes from the fact that we only have 37 points/stations available for the fit (at best, only for large showers) while as for smaller events only a very limited number of points might be available at larger ranges (this is because we require shower cores to be inside the detector area). When selecting a fit range far from shower core, too few stations would be available for the fit. With data affected also by fluctuations, we can expect that the fit would give in fact poor results. The plot in figure 4.25 is a correlation between the reconstructed $S(500)$ and true $\rho(500)$ values and depicts the case of two radial fit ranges, 200 m - 700 m and 300 m - 700 m. The upper limit of 700 m is chosen arbitrarily large, but according to the layout and size of the KASCADE-Grande array. It is obvious that for a radial fit range starting closer to shower core, the reconstruction efficiency of the fit function increases significantly. Due to the limited number of detector stations available, even a reduced number of additional stations (at low radial ranges in this case) will help the fit algorithm to better describe the density distribution at 500 m. We will thus exclude from the fit only the stations very close to the shower core (up to 40 m, to avoid saturated stations).

For a fixed radial fit range, we might have a different number of active sta-

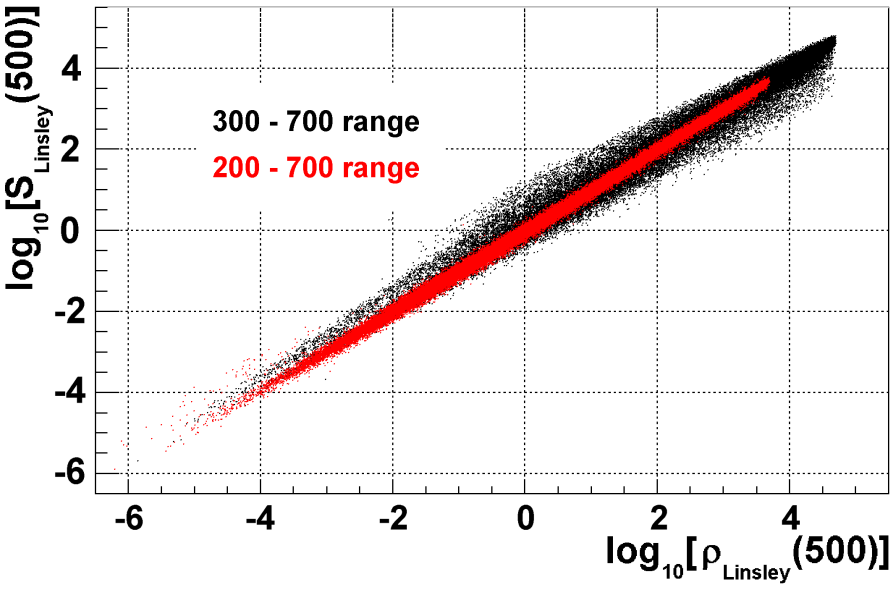

Figure 4.25: This plot shows that for a radial fit range starting at lower values, the reconstruction accuracy at 500 m increases.*(G. Toma, private communications of the KASCADE-Grande collaboration, 2008)*

tions in the fit range depending on the size of the EAS event. The fit quality will vary in consequence. We make a test in which stations are set silent randomly at large radial ranges (thus simulating showers of different sizes). The plot in figure 4.26 represents a correlation between the fit result $S(500)$ and the true $\rho(500)$ and shows that the fit quality improves significantly when more stations are available for the fit. Thus, we will have to impose a minimum number of stations for the events that are accepted by the reconstruction routines of SHOWREC, in order to exclude the small events that are likely to be reconstructed incorrectly.

Beside the effect of the number of station inside the fit range we are also interested in understanding what is the effect of their positioning inside the fit range. As an illustrative example of the problem, one can easily foresee two different cases: for a given fit range and for a given number of stations inside the fit range we could have the majority of stations gathered around a certain radial range or, alternatively, we might have them evenly spread over the entire fit range. The two cases will be treated differently by the fit and therefore the quality of the reconstruction will be different. The plot in figure 4.27 illustrates the difference. The gray distribution represents the correlation between the reconstructed $S(500)$ and the true function value $\rho(500)$ for events having 8 stations inside the fit range and the active station with the largest core distance closer than 350 m. The least scattered gray population represents events with 8 active stations in the fit range, but with the farthest active station farther than 350 m. The quality of fit is better for this population. We conclude that it is important to have active stations inside the fit range as far as possible from the shower core. As a result, all stations will be accepted from the lowest possible radial range (of 40 m) up to the farthest possible (if the shower core

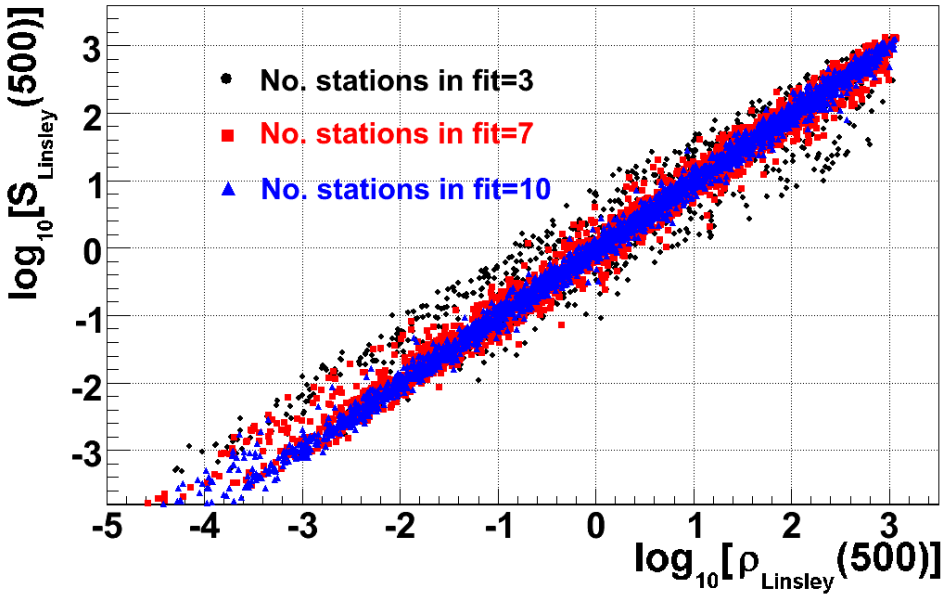

Figure 4.26: A correlation between the fit result $S(500)$ and the true $\rho(500)$ for different number of stations in the fit range; the quality of the fit increases for increasing number of stations inside the radial fit range.

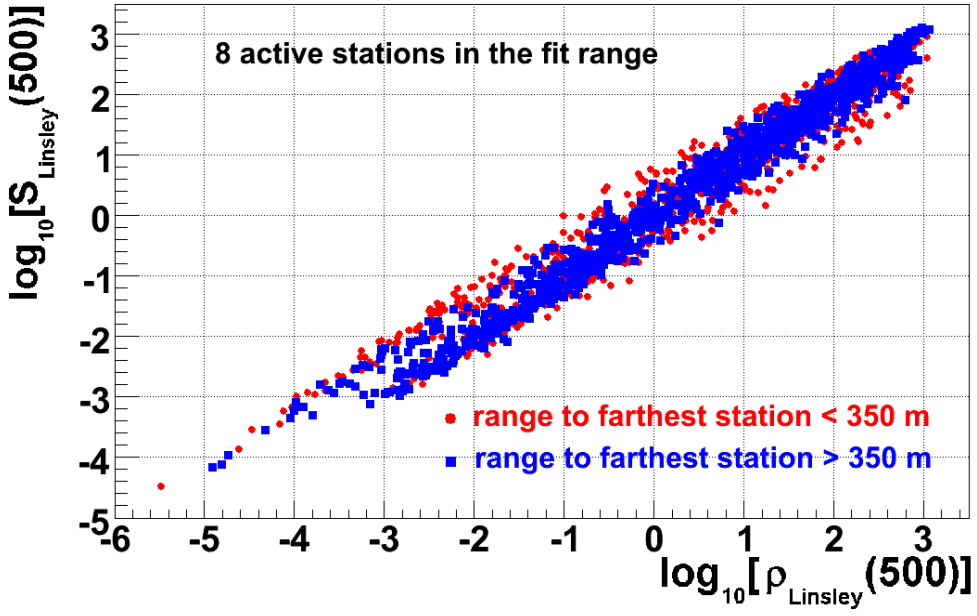

Figure 4.27: Correlation between the reconstructed $S(500)$ and the true function value $\rho(500)$ for events having 8 stations inside the fit range. The two markers represent the case of the farthest station closer than 350 m to shower core (circles) and the case of the farthest station at ranges greater than 350 m (squares). The plot shows that the quality of the fit increases if there are stations available for the fit at larger distances.

Angle[°]	0°	10°	20°	30°	40°
r[m]- detector plane	500	500	500	500	500
r[m]- normal plane	500	492	470	433	383

Table 4.1: The decrease of radial range in the normal plane with increasing zenith angle for a given 500 m radial range in the detector plane.

of an event is placed in the corner of the Grande array then the farthest station can not be farther than 1000 m and therefore the fit range that will be considered from now on is 40 m - 1000 m, effectively accepting all stations at large distances).

In the discussion above, we have always assumed that the reconstruction is performed in the detector plane. In the real reconstruction procedure, the data in the detector plane is in fact projected onto the normal plane and the two planes coincide only in the case of vertical showers. In the case of inclined showers, the radial range available in the shower plane is generally decreased (due to the projection), so the reconstruction efficiency is expected to decrease. A simple orthogonal projection from detector plane onto normal plane (for various angles of incidence) transforms a radial range of 500 m as in table 4.1. In order to avoid reconstructing showers with no data at ≈500 m from shower core, a limitation of the angle of incidence should be imposed when selecting showers. Starting from 30°, the radial ranges are significantly reduced (to less than ≈85%) by the projection and therefore only showers inclined up to 30° will be analyzed.

In order to evaluate the effect of data fluctuations, noise has been added

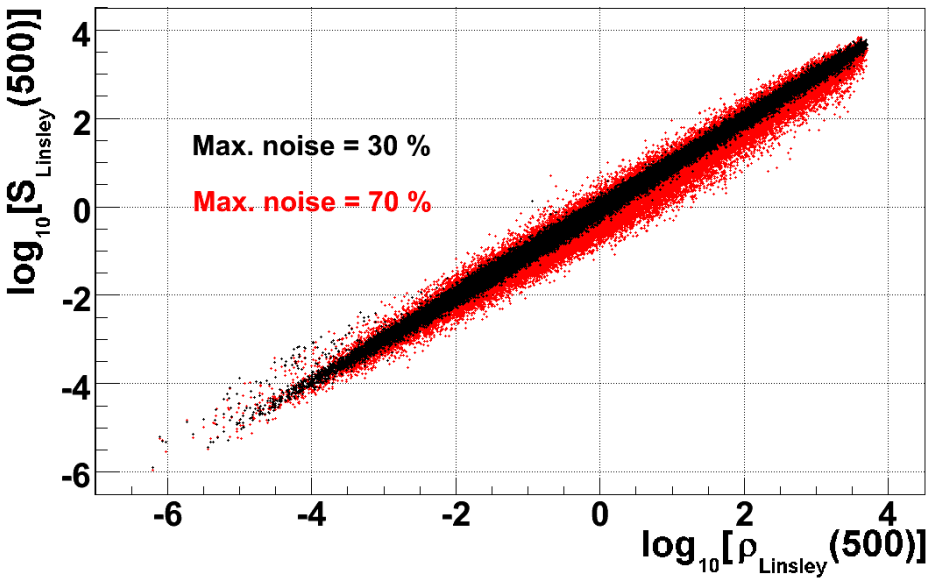

Figure 4.28: Correlation between the reconstructed $S(500)$ and the true function value $\rho(500)$ for events affected by different levels of noise.

randomly to the lateral distribution. It was possible to add noise with a given maximum amplitude as a percentage of the data value. The plot in figure 4.28 shows

that the quality of the fit decreases with the increase of the maximum noise level.

Another important test is the one in which we evaluate the minimum number of stations an event should trigger in order to be accepted for reconstruction. Various tests were already presented showing that small events are poorly reconstructed due to small particle densities around 500 m or due to missing stations at such distances. We will therefore have to impose a cut on the number of triggered stations in order to limit the presence of such showers in the reconstruction. For this, we generate a roughly equal number of events triggering different number of stations (these events are represented in fig. 4.29 with open bars; the number of showers triggering a given number of stations is generated randomly and that is why there are small differences between bars). We then plot the same distribution but only from those events in which the station with largest distance from shower core is situated farther than 500 m (this distribution is presented also in fig. 4.29 with filled gray bars). We can see that with the increase of the number of active stations the chance of having active stations at $\sim$500 m increases too. However, even if an event is triggering all 37 stations it is still possible that there is no active station farther than 500 m (as the last empty bar is not filled). Also we note that for events triggering 24 stations or less there is practically almost no event with active station at 500 m. We will therefore require from an event to trigger at least 25 stations in order to be accepted in the reconstruction (this is to exclude most smaller showers with no data at 500 m). For inclined showers we expect the situation to deteriorate since the reconstruction is performed in the normal plane and the projection of distances from the detector plane will shrink all radial distances accordingly. The case of inclined showers has been brought up before, when deciding to limit the angle of incidence to 30°.

4.4 Reconstruction by SHOWREC - outlook

Various tests have been performed in the attempt to best understand the behavior of the SHOWREC reconstruction procedure. Each relevant element of the reconstruction has been investigated in order to understand the strengths and limitations of the method. The main conclusions derived from this chapter are presented below. Some of these conclusions will act as guidelines when performing the reconstruction in the following chapters.

- SHOWREC is functioning independently from the standard reconstruction and identically for simulated and experimental events.
- A considerable increase in reconstruction speed is achieved by parameterizing the energy deposits of particles in detectors and thus by fast calculations of LECF functions.
- The parameterization most suited for this study is the Lisnley function. Comparative tests have shown that it is most stable in describing the lateral density distribution at various radial ranges (and for various radial fit ranges).

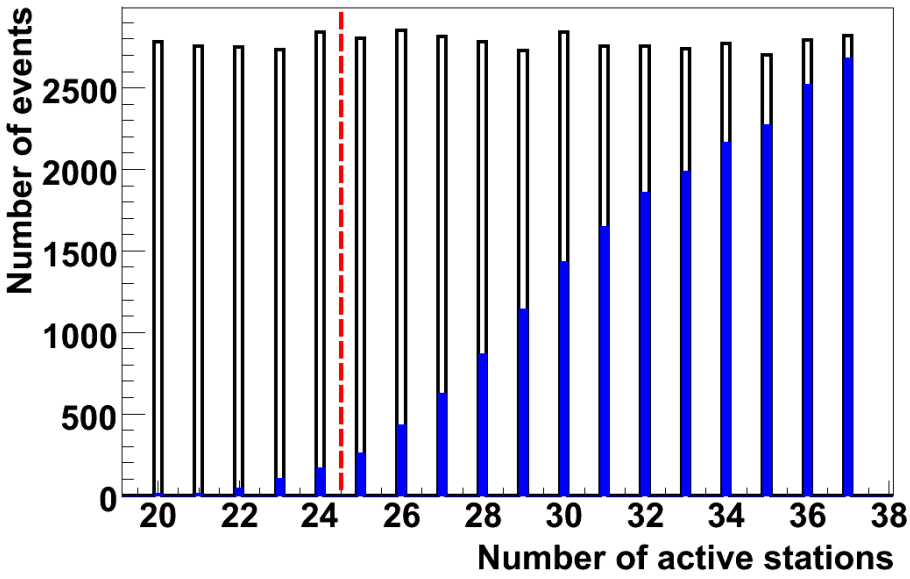

Figure 4.29: Total number of showers triggering a given number of active stations (black empty bars) and the fraction of events with active stations farther than 500 m (gray filled bars); all events below the dashed line will be rejected since they have almost no data in the lateral distribution at 500 m.

- The shape of the Linsley function is most sensitive to the value of the η parameter. In trying to evaluate the quality of the reconstruction one should investigate also to the values of this parameter.
- We expect that the reconstruction will give good results for high energy showers triggering large number of stations and with shower cores placed in such positions so that there are active stations close to 500 m. The lateral distribution of such showers will also be less affected by fluctuations. This means that the reconstruction will get more reliable towards higher energies.
- For the small showers the reconstruction will tend to underestimate the $S(500)$ and implicitly the reconstructed energy.
- The Linsley parameterization will describe the lateral density distribution with better accuracy when fitting larger radial distances (from small radial ranges i.e. 40 m to the farthest available i.e. 1000 m).
- The reconstruction quality will decrease with the increase of the zenith angle since radial distances are reduced by the projection in the normal plane. To limit this effect, those showers will be selected for which the zenith angle is below 30°.
- To maximize the ratio of events with active station around 500 m we will accept only those events triggering at least 25 Grande detector stations.

Chapter 5

The S(500) parameter

The SHOWREC reconstruction is applied for a set of simulated extensive air showers and then for an experimentally recorded one. The main goals of the investigation of simulated events is to test that $S(500)$ is indeed insensitive to primary mass, to establish the dependency between the primary energy E_0 and the reconstructed $S(500)$, to test the efficiency of the reconstruction chain and in general to fine-tune the reconstruction procedure. The procedure to generate Monte Carlo simulated events has been thoroughly described in Chapter 4, Section 4.1.1. The reconstruction is performed identically for every simulated and experimental shower and the $S(500)$ observable is reconstructed for every event. The attenuation effects characteristic to inclined showers in the atmosphere are investigated and then corrected by employing the **C**onstant **I**ntensity **C**ut method (CIC) [45]. The CIC-induced systematic uncertainty of $S(500)$ is evaluated.

5.1 Reconstruction of S(500)

5.1.1 Data selection

To ensure a good quality of the simulated and experimental events samples, a number of events are excluded by applying certain quality cuts (some of these cuts are derived from tests described in Chapter 4). As a general rule, the same quality cuts have been applied for both simulated and experimental events although there are some cuts that are specific to the experimental study. The imposed quality cuts presented below allow for selection of:

1. only events for which the reconstructed shower fell inside the detector array (this cut is introduced in order to minimize the risk of analyzing events that are geometrically poorly reconstructed; the considered fiducial area is defined by the KASCADE coordinates X∈[-500 m; 0 m], Y∈[-550 m; 50 m]) - see figure 141;

2. only events for which the station with maximum energy deposit is not one of the border stations (this cut is introduced in order to avoid reconstructing showers for which the core is poorly reconstructed);

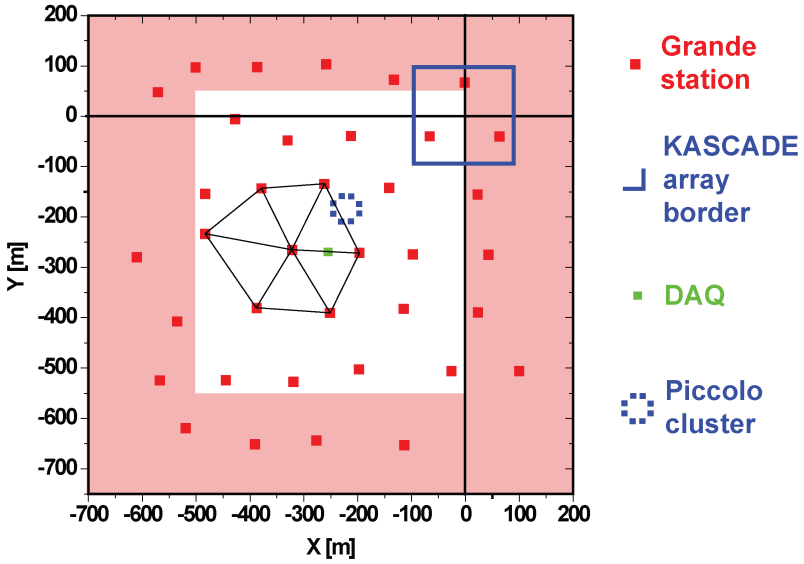

Figure 5.1: This plot shows in gray the area excluded by the shower core cut (a trigger hexagon is represented with continuous lines); the fiducial area is the rectangular one defined by X∈[-500 m; 0 m], Y∈[-550 m; 50 m].

3. only events triggering more than 7 trigger hexagons (a trigger hexagon is defined by 6 stations in a hexagonal pattern and the central station, as depicted schematically in fig. 141; the purpose of this cut is to create a sample of larger EAS events and to exclude the very small showers that tend to be poorly reconstructed);

4. only events for which the reconstructed zenith angle is less than 30° (to avoid reconstructing small events that have no data close to 500 m); the reason of this cut is presented in more detail in Chapter 4);

5. only events triggering more than 24 Grande stations (a cut introduced in order to select larger events and thus to minimize the risk of analyzing small showers characterized by lack of density information at ≈500 m distance from shower core; this quality cut has been investigated in more detail in Chapter 4).

6. only events for which the Linsley LDF approximation results in a good quality fit. The quality of the approximation is mainly evaluated by the values of the η fit parameter (as described in detail below), and only the events for which η<9.9 are accepted.

7. only events not susceptible of being triggered by the ANKA facility. This cut is characteristic for the experimental sample since it is related to the surrounding environment of the KASCADE-Grande array. Thus, the ANKA accelerator facility [99,100] is placed in close proximity of the KASCADE-Grande detector array and, during operating time periods, it can trigger the EAS detection array and thus lead to the recording of a false event. A technique has been devised to efficiently identify and exclude such false counts from the analysis

and only events not susceptible of being triggered by the neighboring ANKA facility are analyzed.

8. only those events recorded during the normal operation of the detector (this is another cut that is characteristic to the experimental investigation; events recorded during anomalous operation of the detector have been flagged and excluded from the analysis).

The Linsley approximation is performed on the 40 m - 1000 m radial range in order to avoid using the information from detector stations too close to the shower core (where there is a high probability of stations being saturated) and also to have data in the lateral distribution at larger radial ranges as close to 500 m as possible (or above when possible).

We emphasize in the following the significance of the quality cut on the η parameter. For this we rely mostly on the investigation of simulated events. In the fit routine, the fit parameters are allowed specific limits in which to be adjusted by the minimization algorithm. The intervals for the two shape parameters are $\alpha \in [0,2)$ and $\eta \in (2,10]$. The reason for choosing these intervals is derived from the analytical form of the Linsley function as explained in more detail in Chapter 4, Section 4.3.4. The resulting parameter distribution for the simulated EAS sample (before applying the η cut) are depicted below (figures 5.2 and 5.3). We will show that events with η very close to the upper limit 10 are in fact events with poorly reconstructed $S(500)$ (they amount for ≈13% of the total sample when all other cuts are already applied).

In the absence of the η cut, the $S(500)$ spectrum exhibits two main features

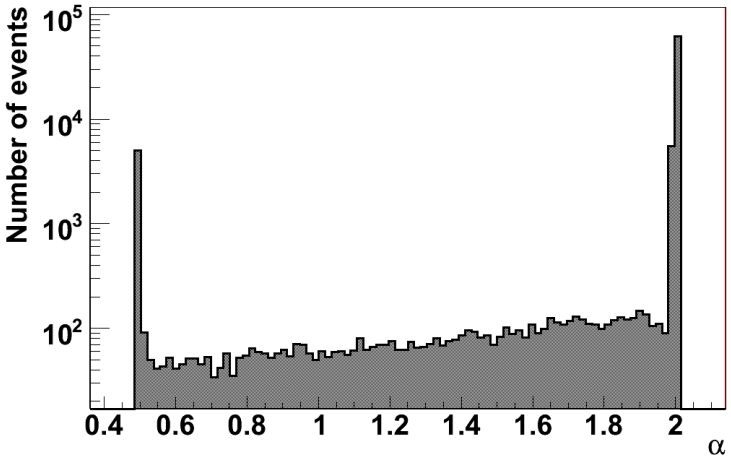

Figure 5.2: The distribution of the α parameter for the simulated shower sample (all primaries). The great majority of the events give an α value at the border of the allowed interval.

(figure 5.4 presents the case of simulated showers). While most of the events have their reconstructed $S(500)$ values gathered in the expected shape of a spectrum (zone A), some of them form a "*hump*"-like structure towards lower values (zone B).

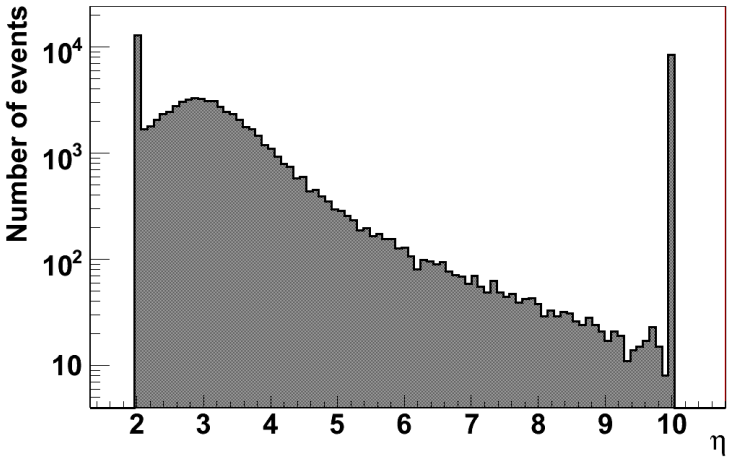

Figure 5.3: The distribution of the η parameter for the simulated shower sample (all primaries).

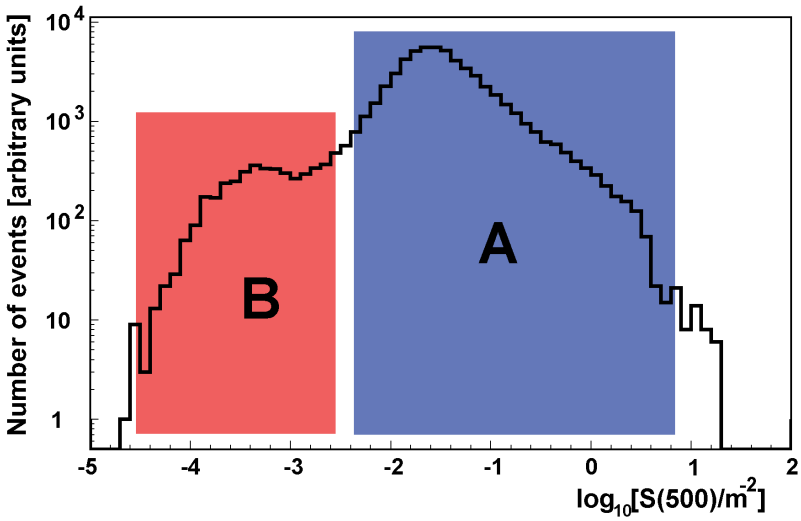

Figure 5.4: $S(500)$ spectrum obtained after the SHOWREC reconstruction of the simulated events when no cut on the η variable is performed (all primaries). Note the two features of this spectrum (the two grayed zones A and B are defined intuitively for explanatory purposes).

We can easily establish a correlation between events belonging into zone B of figure 5.4 with their η parameter value by overlaying the spectrum of showers having $\eta \approx 10$ ($\eta \in [9.9,10]$). The plot in figure 5.5 depicts the case of these events (the hatched distribution). We can conclude that in fact feature B of the spectrum is created exclusively by events with $\eta \approx 10$. When performing a cut on the η parameter these showers will be excluded. We can see that these events have their $S(500)$ predominantly underestimated (though there are also cases of overestimation). The poor reconstruction is caused by limitations in the functionality of the minimization routine that are in turn triggered by various factors (see Chapter 4, Sections 4.3.3-4.3.5). For some events, the distribution of active stations around the shower core and the fluctuations of data, coupled with the Linsley fit instability leads MINUIT into pitfalls and ultimately towards a poor result. This kind of behavior is often hard to predict and prevent and could lead to both underestimation and overestimation of the result. Further tests could not establish a clear relation between the reconstruction quality and other specific values of the shape parameters.

The next plots present some relevant correlations and the effects of the cut on

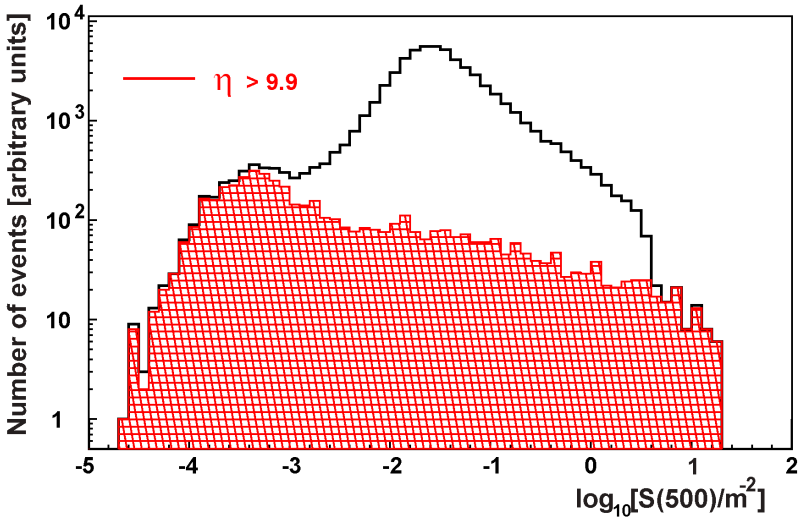

Figure 5.5: In black, the $S(500)$ spectrum (all primaries) for the simulated sample when all cuts are applied, except the η cut. The hatched area represents the contribution of events with $\eta \approx 10$. These events are excluded by the cut on the η parameter (their value is predominantly underestimated).

the η variable. Figure 5.6 presents the correlation of the reconstructed $S(500)$ with the true primary energy E_0 of events (available from CORSIKA). The scattered gray population is excluded by the η cut. The remaining data (in black) shows a clear correlation between $S(500)$ and E_0.

Besides $S(500)$, the number of electrons N_e (*size*) in the EAS is another well established energy estimator and for KASCADE-Grande it is made available by the standard reconstruction (implemented in the KRETA code). N_e is available for tests also in the SHOWREC output files (see the variable flow chart in Appendix C) and the plot in figure 5.7 shows the correlation between $S(500)$ and N_e (reconstructed by KRETA at iteration step 3). The scattered gray population contains events with

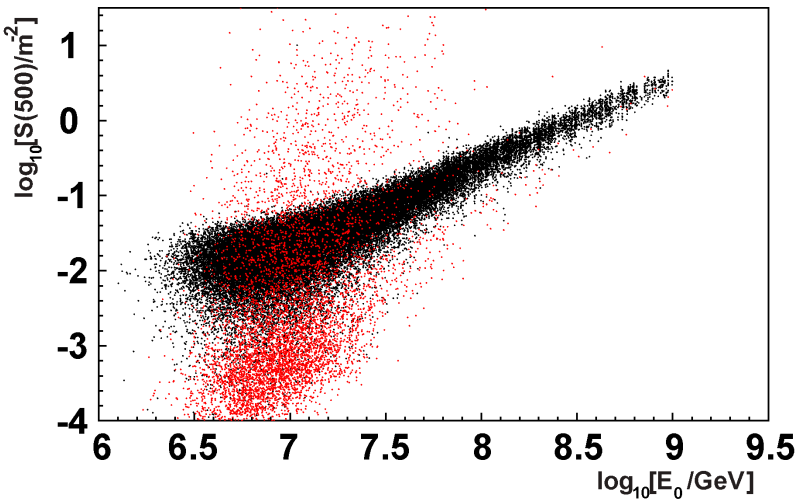

Figure 5.6: This plot shows the $S(500)$ versus the true primary energy E_0 correlation (simulations, all primaries). The smaller scattered population depicted in gray is the contribution of events with $\eta \approx 10$; as in fig. 5.5, these events have their $S(500)$ value systematically underestimated or spread away from the main correlation. The black population contains events with all quality cuts applied.*(G. Toma, private communications of the KASCADE-Grande collaboration, 2008)*

$\eta \approx 10$ and is clearly shifted away from the main population. The spread of this scatter plot is noticeably bigger because it contains the fluctuations of both $S(500)$ and N_e.

5.1.2 Reconstructing the simulated events

When all the shower selection cuts are applied, the resulting simulated EAS sample has 73.920 events in total. The reconstructed $S(500)$ spectrum for the full simulated shower sample with all quality cuts applied is presented in fig.5.9. The shape of the spectrum is expected to map the primary energy spectrum. In fact there is a good correlation between the two and is presented in figure 5.8 (with all quality cuts applied). Another type of poor reconstruction is characteristic to small events and is indicated in this plot. In these cases the lateral particle distribution of small showers is extinct at large radial ranges (that are of special interest in our investigation). Missing active stations at ranges $\approx$500 m means that the minimization will be performed predominantly on the data available at low radial ranges where the lateral particle density is tremendously steeper. Inevitably, at larger radial ranges this will lead to an extrapolation that will continue on the steep trend established by the fit and will result in underestimated values for $S(500)$ (as noted also in Chapter 4, Section 4.3.3). Future investigations should be directed towards improving the reconstruction of such events.

Figure 5.10 shows the total reconstruction efficiency for the simulated shower sample for three zenith angular bins: 0°-30°, 0°-15° and 15°-30°. For higher

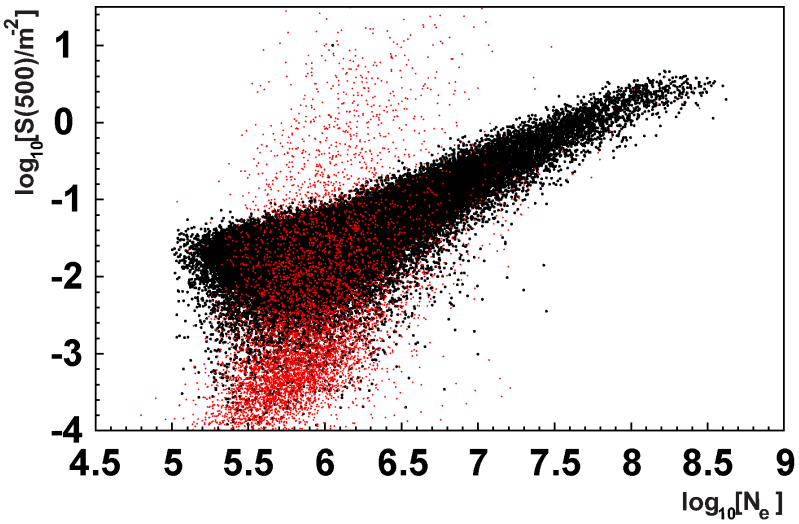

Figure 5.7: Correlation between the number of electrons N_e (available from KRETA) and the $S(500)$ (from SHOWREC) as reconstructed for the simulated shower sample, when η cut is not applied (all primaries). The scattered gray population is characterized by $\eta \approx 10$, the black population contains events with all quality cuts applied.

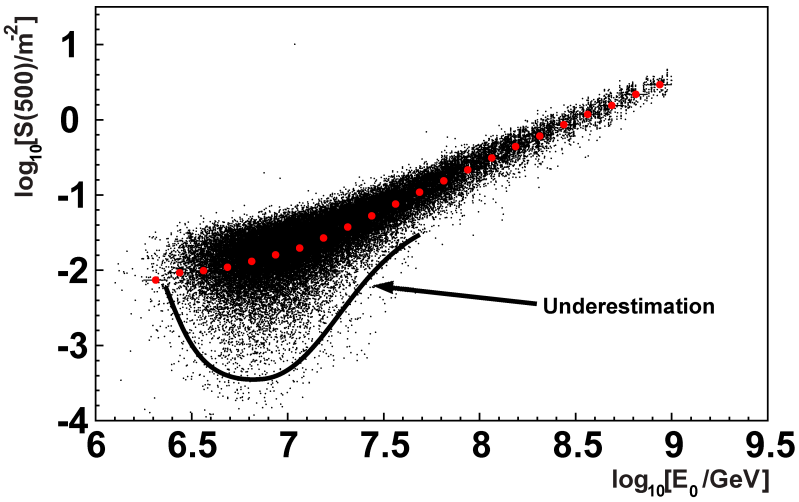

Figure 5.8: The $S(500)$ vs. E_0 correlation for all the simulated events that have passed the quality cuts (the tendency of underestimation for small events is indicated on the plot); the gray dots points are the profile of the scatter plot.

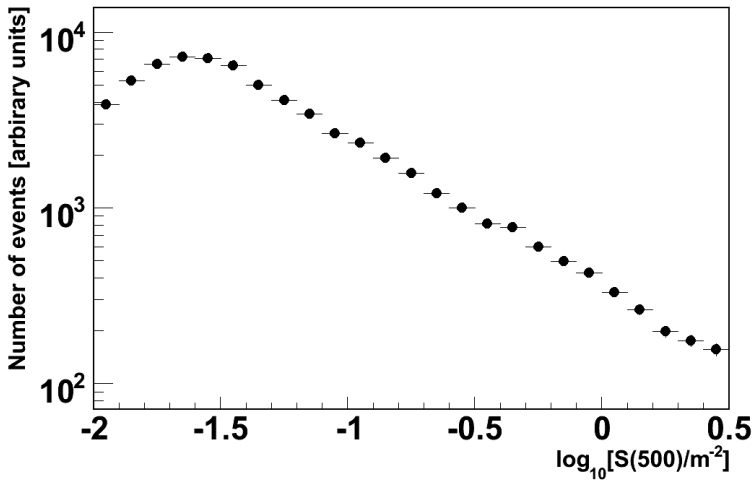

Figure 5.9: The $S(500)$ spectrum for the full simulated showers that survived the quality cuts; the spectrum exhibits a power law-like behavior, feature that was expected, since the $S(500)$ is mapping the primary energy and the primary energy used for input in the CORSIKA simulations is a power law.

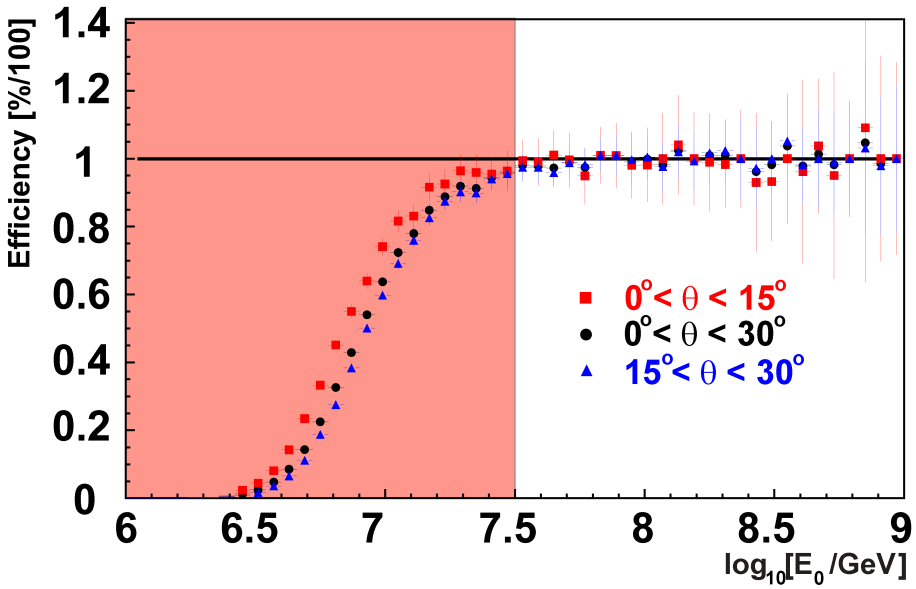

Figure 5.10: Efficiency of reconstruction for different angles of incidence as a function of primary energy.*(G. Toma et al. - KASCADE-Grande collaboration, ISVHECRI 1-6 September 2008, Paris, France)*

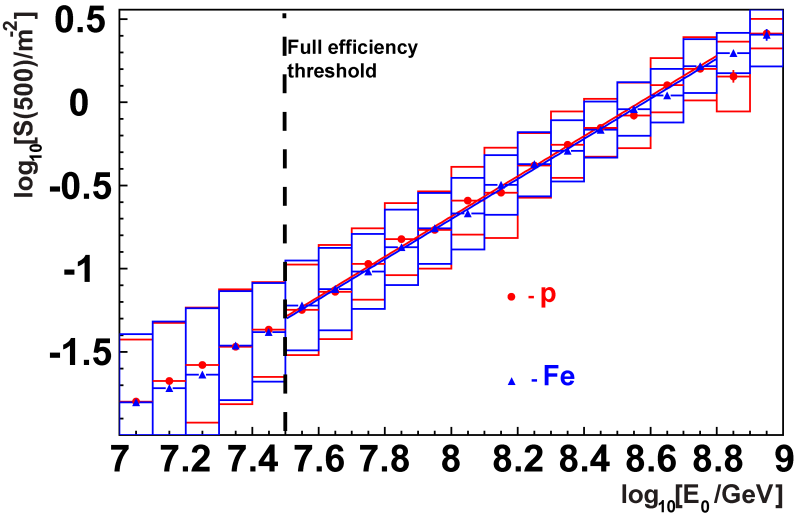

Figure 5.11: $S(500)$ dependence with E_0 for different primary particles (p and Fe). The box-errors are the errors on the spread while the errors on the mean are represented with bars. The continuous lines represent power law fits performed inside the full efficiency range and excluding the last higher energy bins to avoid the effects of loss of statistics at the end of the simulated sample. A narrow zenith angular bin has been used to construct this plot ($\theta \in [18^o, 24^o]$).*(G. Toma et al. - KASCADE-Grande collaboration, 30th ICRC 2007, Merida, Mexico)*

zenith angles (and small energies) the reconstruction efficiency curve is below that of events closer to vertical incidence (the reconstruction efficiency is poorer for more inclined events due to the restricted radial range and to the lower particle density). Figure 5.10 shows that the efficiency exceeds 95% for energies higher than $\log_{10}[E_0/\mathrm{GeV}]$=7.5. The fluctuations of data around the full efficiency value 1 (figure 5.10) is due to mis-reconstructions of the shower core. Thus the efficiency curve is obtained from a ratio of primary energy spectrum of all successfully reconstructed events versus the primary energy spectrum of all events. For the shower selection of reconstructed events the reconstructed shower core is used while as for the spectrum of all events, the true (from CORSIKA) shower core is used. It can happen that some shower cores that are outside the fiducial area are reconstructed inside the fiducial area, while the opposite is also possible and some events may be reconstructed outside the fiducial area where in fact their true shower core was placed inside. The stochastic competition between these two tendencies leads to fluctuations around the maximum possible value of the efficiency curve. For example, an efficiency value higher than 1 means that more showers migrated (by reconstruction) outside the fiducial area than leaked inside. The opposite case leads to values of maximum efficiency smaller than 1.

In fig. 5.11, two $S(500)$ vs. E_0 dependencies are shown for two primaries, a light primary (proton) and a heavy primary (Fe). The $S(500)$ exhibits almost no sensitivity to the mass of the primary particle and therefore the two dependencies are almost identical. The error on the spread (box-errors) is a relatively narrow band. Such a simulation-derived dependency can be used to convert experimentally

recorded $S(500)$ values into the corresponding primary energy values, leading to the reconstructed primary energy spectrum for the detected EAS events (though is must be noted that this is not the calibration curve that will be used for conversion, but a similar one which will be presented in chapter 6). This conversion however is not so straight forward (as it will be shown in the following sections) and some corrections need to be considered before proceeding to this conversion.

5.1.3 Reconstructing the detected KASCADE-Grande events

The same quality cuts are imposed on the experimentally detected shower sample as the ones imposed on the simulated shower sample. A total number of $5.6{\cdot}10^7$ EAS events have been detected by the KASCADE-Grande detector array during 1173 days total time of acquisition. Of these events, only $8.49{\cdot}10^5$ events have passed the imposed quality cuts and their reconstructed $S(500)$ values are considered. The plot in fig.5.12 shows the $S(500)$ spectrum for the experimentally recorded shower sample. The spectrum has a power law-like shape. Its spectral index along with other features will be discussed later in the light of the E_0 - $S(500)$ calibration curve (see the next subsection discussing the constant intensity cut method).

The KASCADE-Grande detector array is not perfectly symmetrical. In-

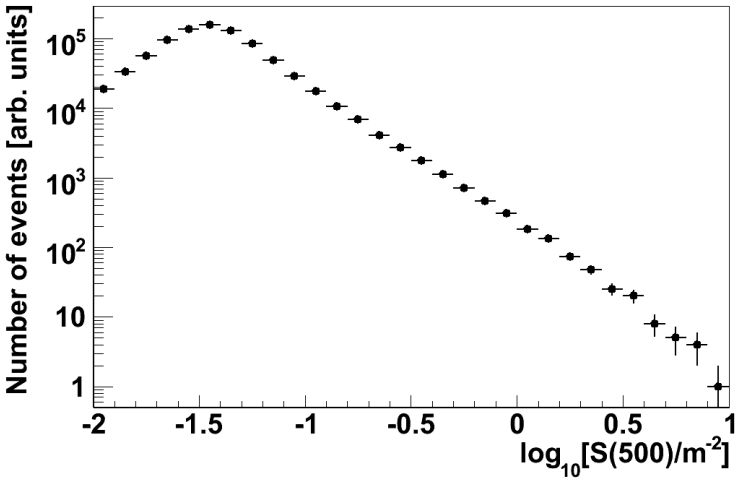

Figure 5.12: $S(500)$ spectrum for the experimentally recorded shower sample (after applying all the quality cuts).

tended as an array with a hexagonal pattern, the final placement of stations was dictated by various landscape features. The question is whether certain geometrical asymmetries of the array can have an impact on the efficiency of $S(500)$ reconstruction. Figure 5.13 show the $S(500)$ spectra obtained from showers falling in different halves of the array. To build this plot, two methods of dividing the array were investigated: a North by South division and a West by East one (these conventions are coded in shades of gray in the plot itself). The spectra do not seem to be affected by the positions of the EAS shower cores inside the fiducial area and therefore we

conclude that the array asymmetries do not play a noticeable role in the $S(500)$ reconstruction efficiency.

The next subsection will detail the attenuation effects of the $S(500)$ observ-

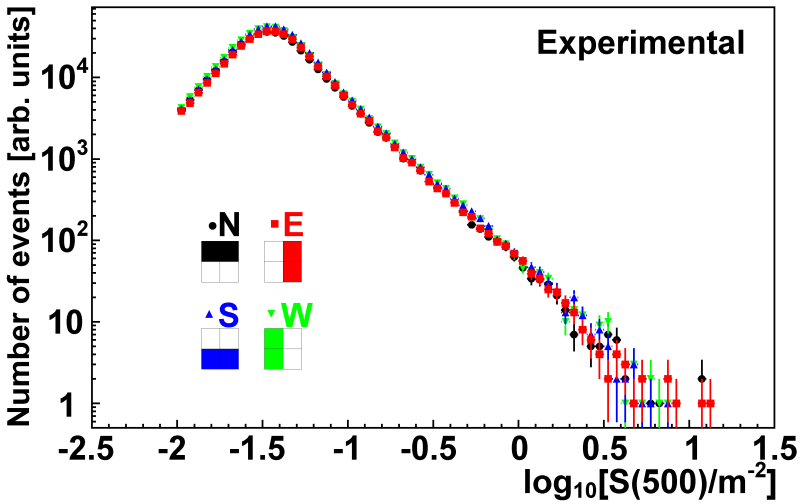

Figure 5.13: This plot shows a comparison between $S(500)$ spectra obtained for sub-samples of full simulated EAS events with shower cores falling inside different halfs of the detector array. *(G. Toma et al. - KASCADE-Grande collaboration, DPG Frühjahrstagung 3-7 March 2008, Freiburg, Germany)*

able with the EAS angle of incidence. Before proceeding to any investigation of the all-event $S(500)$ sample, one has to compensate for the attenuation of $S(500)$.

5.2 The constant intensity cut method

Before converting the recorded $S(500)$ values into the corresponding primary energy values (via a relation derived from simulation studies), one has to take into account the atmospheric attenuation affecting the charged particle densities observed on ground. For more inclined showers, the particles have to cross a longer path through the atmosphere before reaching the detector level. In such a case, on average, events generated by identical primaries (E_0, A) reach the detector level at different stages of EAS development, dependent on their angles of incidence. In order to bring all recorded EAS events to the same level of consistency, one has to eliminate the influence of the zenith angle on the recorded $S(500)$ observables. This is achieved by applying the **C**onstant **I**ntensity **C**ut (**CIC**) method [45]. The $S(500)$ attenuation is visible if $S(500)$ spectra are plotted for different EAS incident angles. For this, the recorded events are separated into several sub-samples characterized by their angle of incidence. The angular intervals are chosen in a way that they subtend equal solid angles: 0° - 13.2°, 13.2° - 18.8°, 18.8° - 23.1°, 23.1° - 26.7° and 26.7° - 30.0° (this partition is in fact similar to a solid angle normalization since we should observe the same number of events in equal solid angles, an effect of the here assumed cosmic rays isotropy). In fig. 5.14 the attenuation is visible, as $S(500)$

spectra are shifted towards lower values for increasing zenith angles. The error bars on these spectra are obtained assuming that the counts in each bin i are following a Poissonian distribution, therefore the value of error bars is equal to the square root of the bin value (eq. 5.1):

$$\sigma_i = \sqrt{n_i} \tag{5.1}$$

The CIC method assumes that a given intensity value in the energy spectrum

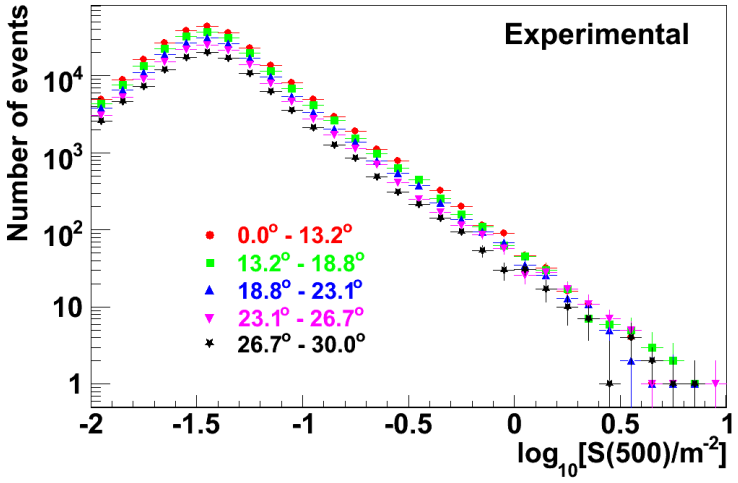

Figure 5.14: Experimentally recorded differential $S(500)$ spectra for different angles of incidence. The shift of $S(500)$ values i.e. spectra towards lower values for increasing angles of incidence is due to attenuation of showers in the atmosphere due to longer cross path.

corresponds to a given primary energy of particles and, since the $S(500)$ is mapping the primary energy spectrum, it is expected that this property of the intensity is true also in the case of $S(500)$ spectra. Therefore a constant intensity cut on integral $S(500)$ spectra is performed, effectively cutting them at a given primary energy (fig. 5.15). The integral $S(500)$ spectrum is obtained in preparation of the constant intensity cut. The value in each bin i in the integral spectrum is given by eq. 5.2:

$$J_i = \sum_{j=i}^{N} n_j \tag{5.2}$$

From eq. 5.1 and eq. 5.2 and using the theorem of propagation of errors we obtain the error bars of each bin in the integral spectrum:

$$\sigma(J_i) = \sqrt{\sum_{j=i}^{N} \sigma^2(J_j)} = \sqrt{(J_i)} \tag{5.3}$$

The CIC method is applied next. A cut is performed on the integral spectra in the range with good statistical quality, at intensity J_{cut}, effectively performing a cut on a given primary energy. The corresponding $S(500)$ value for this particular

cut intersecting each integral spectra is obtained by linear interpolation between two neighboring points in each spectra. The calculated $S(500)$ values are plotted against the sec(θ) corresponding to each angular interval, where θ is the mean of the angular distribution in that angular range. An attenuation curve is obtained (see fig. 5.16). The attenuation length $\lambda_{S(500)}$ of $S(500)$ is evaluated from such curve assuming that $\lambda_{S(500)}$ is given from eq. 5.4.

$$S(500)_\theta = S(500)_{0^\circ} exp\left(\frac{-h_0 \cdot sec\theta}{\lambda}\right) \tag{5.4}$$

where:

$S(500)_\theta$ - the measured $S(500)$ at a zenith angle θ;
$S(500)_{0^\circ}$ - the measured $S(500)$ at vertical incidence;
θ - a given zenith angle in the 0°-30° interval;
h_0 - the atmospheric depth of KASCADE-Grande with h_0=1023 g· cm^{-2};
λ - the $S(500)$ attenuation length [g· cm^{-2}].

The attenuation length $\lambda_{S(500)}$ is evaluated for various constant intensity cuts (see Appendix F) and remains fairly constant over the entire intensity range that is investigated (implicitly, $\lambda_{S(500)}$ remains constant over the entire energy range, since it was shown that cutting the integral spectrum at a given intensity is equivalent to selecting a certain primary energy). On average, the value of $\lambda_{S(500)}$ as derived from the experimental observations is $\bar{\lambda}_{S(500)}$=754±27 g· cm^{-2}.

Additional tests are performed on simulated events in the attempt to bet-

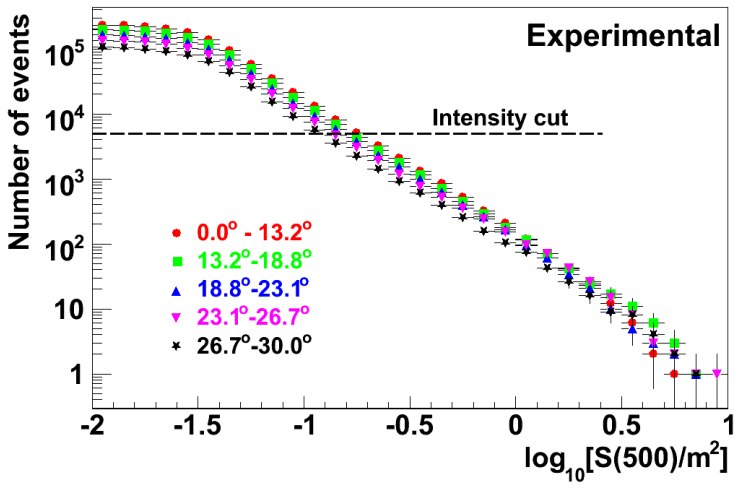

Figure 5.15: Integral $S(500)$ spectra; the horizontal line is a constant intensity cut at an arbitrarily chosen intensity.*(G. Toma et al. - KASCADE-Grande collaboration, ISVHECRI 1-6 September 2008, Paris, France)*

ter understand the attenuation of EAS observables in general (and the attenuation of $S(500)$ in particular). Besides the case of $S(500)$, the attenuation of the muon component N_μ and that of the electron component N_e have been evaluated from simulations for different energy ranges and different energy thresholds (see Appendix F).

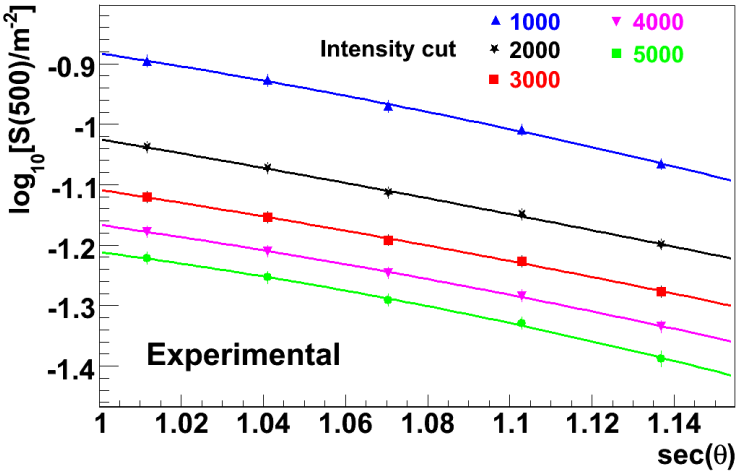

Figure 5.16: Attenuation of the $S(500)$ observable with the angle of incidence; the different curves show a set of arbitrarily chosen intensity cuts (in this plot, every point corresponds to an angular interval and the position of each point on the sec(θ) axis is the mean of the angular distribution in the respective angular interval).

The average values of λ_{N_μ} and λ_{N_e} (over the considered energy ranges) are found to be $\bar{\lambda}_{N_\mu}$=1637±33 g· cm^{-2}and $\bar{\lambda}_{N_e}$=377±3.3 g· cm^{-2}. Obviously, since muons form the EAS penetrating component, λ_{N_μ} is much larger when compared to λ_{N_e}. Similar studies on simulated events give an average value of $\bar{\lambda}_{S(500)}$=721±29 g· cm^{-2}. The value of $\lambda_{S(500)}$ in relation to i.e. between the λ_{N_e} and λ_{N_μ} is easy to explain since $S(500)$ exhibits mixed features of both EAS components (electron and muon). Attenuation lengths for all observables of interest seem fairly constant over the entire considered energy range. The value of $\lambda_{S(500)}$ as derived from simulations is in acceptable agreement with the value derived from experimental measurements.

In order to correct the attenuation of $S(500)$ it has been decided that an experimentally derived attenuation correction curve will be used. The advantage of relying on experimental data is that of avoiding any bias that could affect the simulations. In order to accurately describe the attenuation of observables, a simulation should ensure that the development of showers in the simulated sample is consistent with the development of real showers. For example when comparing simulated events with different inclinations we should know that at least the height of their first interaction is similar. This can be difficult to control when generating a limited simulated shower sample. Thus, for the attenuation correction, the experimental data is used without inference of simulations.

Both simulated and experimental studies show that the attenuation of $S(500)$ is fairly constant inside the considered energy range (we therefore assume that the attenuation curves are parallel). This means that we could use any of the attenuation curves in order to build our attenuation correction function. For the estimation of the attenuation length of $S(500)$ we have assumed an exponential attenuation and therefore we have used an exponential form for the description of the attenuation curve. For the purpose of correcting the recorded data we will make no assumption

on the shape of the attenuation curve and only try to find a parameterization that best describes it (thus a second degree polynomial curve will be used). We choose an attenuation curve that resulted from a CIC cut performed in a part of the spectrum that has good statistical quality. Additionally we are also selecting that curve for which a fit with a second degree polynomial fit gives the best result (in what concerns the χ^2 of the fit and the parameter uncertainties).

Since the experimental zenith angle distribution is peaked at ≈21° (fig. 5.17)

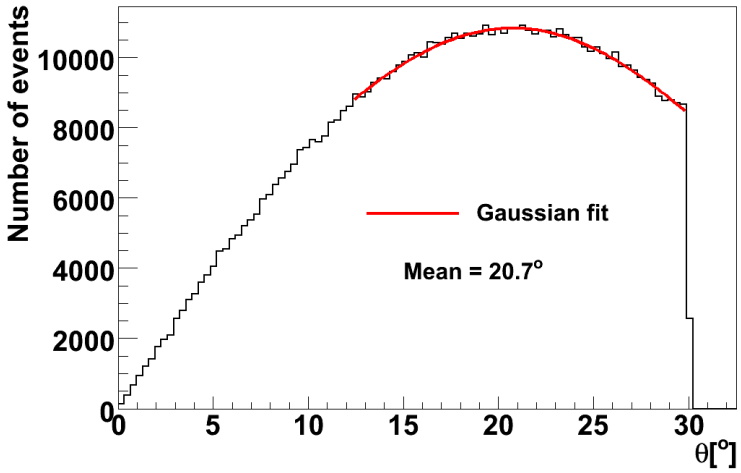

Figure 5.17: The experimental zenith angular distribution peaks at ≈21°; the continuous line is a Gaussian fit in order to establish the peak position.

we will use this value next as reference angle and correct all $\log_{10}S(500)$ values as if the EAS would be coming from this angle. We thus obtain an all-event $S(500)$ spectrum (fig. 5.19) in which all initial $S(500)$ values have been corrected for attenuation and converted into their would-be values at 21°. Attenuation corrected spectra for events in different zenith angle bins now overlap (fig. 5.18).

Since the $S(500)$ is mapping the primary energy we expect that features of the primary energy spectrum will be reflected in the $S(500)$ spectrum. In regard to the plot in figure 5.19 we note that the $S(500)$ spectrum has a power law-like shape. Anticipating the results in the next chapter, we investigate the spectral index of the $S(500)$ by fitting it with a power law. The resulting spectral index is $\gamma_{S(500)} = -3.00 \pm 0.01$. We will show later (Chapter 6) that in fact the dependency E_0 - $S(500)$ can be expressed as a power law with slope γ=0.90±0.01 (close to 1.0) and therefore the spectral index of $S(500)$ should not be very different from the spectral index of the energy spectrum of cosmic rays in this energy range. Thus the value of the $S(500)$ spectral index indicates that the spectral index of the primary energy is also close to -3. Additionally the $S(500)$ spectrum exhibits no other visible features (a knee-like structure, like the expected "second knee" in this energy range is difficult to observe on a spectrum without multiplication). Therefore it is necessary to multiply a spectrum with the corresponding energy to a power between 2 and 3 in order to make such features more easily observable. Such multiplication procedure will be applied in the next chapter on the reconstructed energy spectrum.

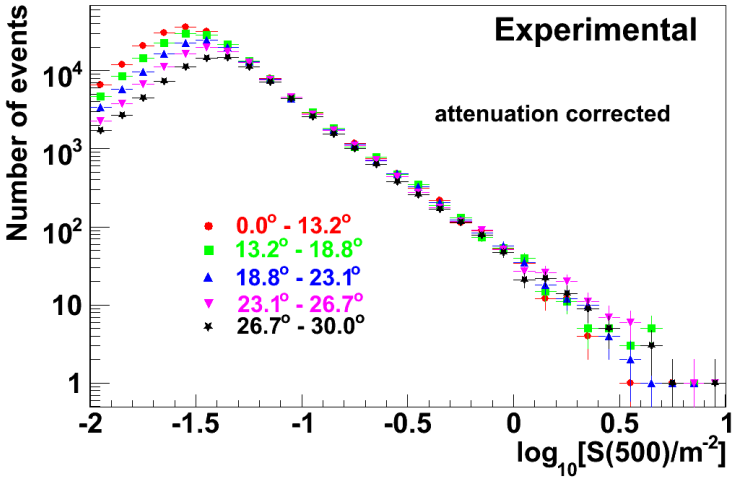

Figure 5.18: This plot shows the differential $S(500)$ spectra corrected for the attenuation effect. The spectra for different zenith angles overlap.*(G. Toma et al. - KASCADE-Grande collaboration, ISVHECRI 1-6 September 2008, Paris, France)*

5.3 CIC error estimation

We intend to calculate first the error associated to the $S(500)$ values in fig. 5.16. We start from the linear interpolation between two neighboring points in the integral $S(500)$ spectra (after the CIC cut) and we have:

$$J_i = p_0 + p_1 \cdot log_{10}S_i(500) \tag{5.5}$$

$$J_{i+1} = p_0 + p_1 \cdot log_{10}S_{i+1}(500) \tag{5.6}$$

Where i and i+1 are consecutive bins in the integral spectrum J_i, J_{i+1} their corresponding intensities with J_i<J_{cut}<J_{i+1} and with $S_i(500)$ and $S_{i+1}(500)$ the corresponding positions of the two bins on the $\log_{10}(500)$ scale of the spectrum. From 5.5 and 5.6 we have:

$$p_1 = \frac{J_{i+1} - J_i}{log_{10}S_{i+1}(500) - log_{10}S_i(500)} \tag{5.7}$$

$$p_0 = J_{i+1} - p_1 \cdot log_{10}S_{i+1}(500) \tag{5.8}$$

And from the propagation of errors we obtain:

$$\sigma^2(p) = \left(\frac{\partial p}{\partial J_{i+1}}\right)^2 \sigma^2(J_{i+1}) + \left(\frac{\partial p}{\partial J_i}\right)^2 \sigma^2(J_i) + 2\left(\frac{\partial p}{\partial J_{i+1}}\right)\left(\frac{\partial p}{\partial J_i}\right) cov(J_{i+1}, J_i) \tag{5.9}$$

Where p is any of the two p_0 or p_1 fit parameters. cov(J_{i+1},J_i)=J_{i+1} and from (5.9) we get the two errors associated to the two parameters:

$$\sigma^2(p_1) = (J_i - J_{i+1})[log_{10}S_{i+1}(500) - log_{10}S_i(500)]^2 \tag{5.10}$$

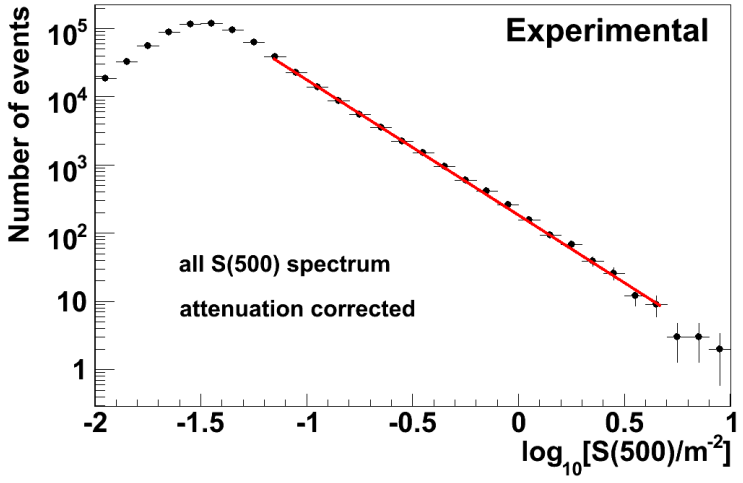

Figure 5.19: $S(500)$ spectrum for the experimentally recorded shower sample ($\theta \in [0°,30°]$), after CIC (the continuous line is a power law fit - spectral index $\gamma = -3.00 \pm 0.01$, χ^2=1.1).*(G. Toma et al. - KASCADE-Grande collaboration, ISVHECRI 1-6 September, Paris 2008, France)*

$$\sigma^2(p_0) = J_{i+1} + \sigma^2(p_1)[log_{10}S_{i+1}(500)]^2 \tag{5.11}$$

Furthermore:

$$cov(p_0, p_1) = -\sigma^2(p_1)[log_{10}S_{i+1}(500)] \tag{5.12}$$

and with:

$$log_{10}S_{cut}(500) = \frac{1}{p_1}(J_{cut} - p_0) \tag{5.13}$$

We obtain the error associated to the $\log_{10}S_{cut}(500)$:

$$\sigma^2[log_{10}S_{cut}(500)] = \left(\frac{\partial log_{10}S_{cut}(500)}{\partial p_0}\right)^2 \sigma^2(p_0) + \left(\frac{\partial log_{10}S_{cut}(500)}{\partial p_1}\right)^2 \sigma^2(p_1) + \\ +2 \cdot \left(\frac{\partial log_{10}S_{cut}(500)}{\partial p_0}\right)\left(\frac{\partial log_{10}S_{cut}(500)}{\partial p_1}\right) cov(p_0, p_1) \tag{5.14}$$

Or, simplified with the above calculations (5.10), (5.11), (5.12) and (5.13):

$$\sigma^2[log_{10}S_{cut}(500)] = \frac{\sigma^2(p_1)}{p_1^4}(J_{cut} - J_{i+1})^2 + \frac{J_{i+1}}{p_1^2} \tag{5.15}$$

The calculated $\sigma[\log_{10}S_{cut}(500)]$ is used for the points in the attenuation curve (fig. 5.16). For the purpose of attenuation correction, the attenuation curve can be parameterized with a second degree polynomial function (as described in the previous section). We will use the following parameterization for the attenuation curve:

$$log_{10}S_{cut}(500) = p_0 + p_1 \cdot sec\theta + p_2 \cdot sec^2\theta \tag{5.16}$$

The attenuation correction for the reference angle θ_{ref}=21° is done with the formula (derived from (5.16)):

$$log_{10}S_{cut}(500) = log_{10}S(500) + p_1 \cdot [sec(\theta_{ref}) - sec(\theta)] + p_2 \cdot \left[sec^2(\theta_{ref}) - sec^2(\theta)\right] \tag{5.17}$$

From (5.17), the CIC induced error associated to the $\log_{10}S_{ref}(500)$ is:

$$\sigma^2[log_{10}S_{ref}(500)]_{CIC} = \left(\frac{\partial log_{10}S_{ref}(500)}{\partial p_1}\right)^2 \sigma^2(p_1) + \left(\frac{\partial log_{10}S_{ref}(500)}{\partial p_2}\right)^2 \sigma^2(p_2) + \\ +2 \cdot \left(\frac{\partial log_{10}S_{ref}(500)}{\partial p_1}\right)\left(\frac{\partial log_{10}S_{ref}(500)}{\partial p_2}\right) cov(p_1, p_2) \Rightarrow \tag{5.18}$$

$$\Rightarrow \sigma[log_{10}S_{ref}(500)]_{CIC} = [sec(\theta_{ref}) - sec(\theta)]^2 \sigma^2(p_1) + \\ + \left[sec^2(\theta_{ref}) - sec^2(\theta)\right]^2 \sigma^2(p_2) + \tag{5.19}$$

$$+2 \cdot [sec(\theta_{ref}) - sec(\theta)] \left[sec^2(\theta_{ref}) - sec^2(\theta)\right] cov(p_1, p_2)$$

The following plots depict the CIC-induced uncertainty of $S(500)$ as a function of the angle of incidence (fig. 5.20) and of the corrected $S(500)$ value (fig. 5.21).

After the attenuation correction, the next step of our investigation will fo-

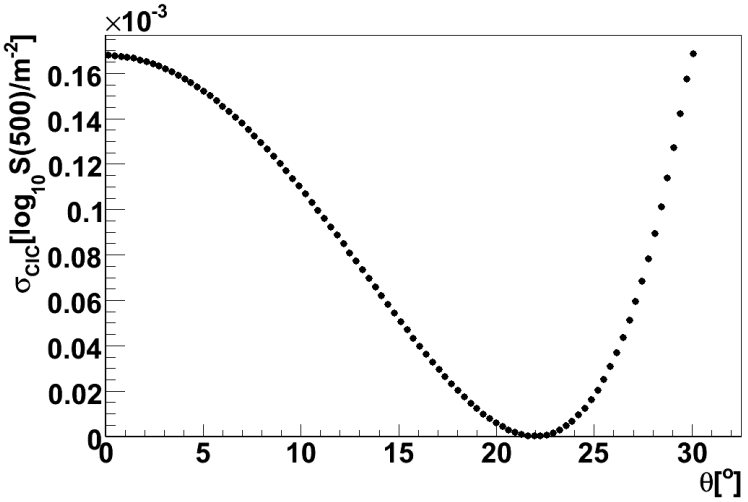

Figure 5.20: Uncertainty induced by the CIC method to the corrected $S(500)$ observable (this plot shows the profile of the distribution of the $\sigma[\log_{10}S_{ref}(500)]_{CIC}$ vs. θ; the error bars in this plot are the error of the mean and are dot-sized. The uncertainty is lowest for the chosen reference angle.

cus on converting $S(500)$ values into the corresponding primary energies in order to build the primary energy spectrum. This procedure is described in detail in the next chapter.

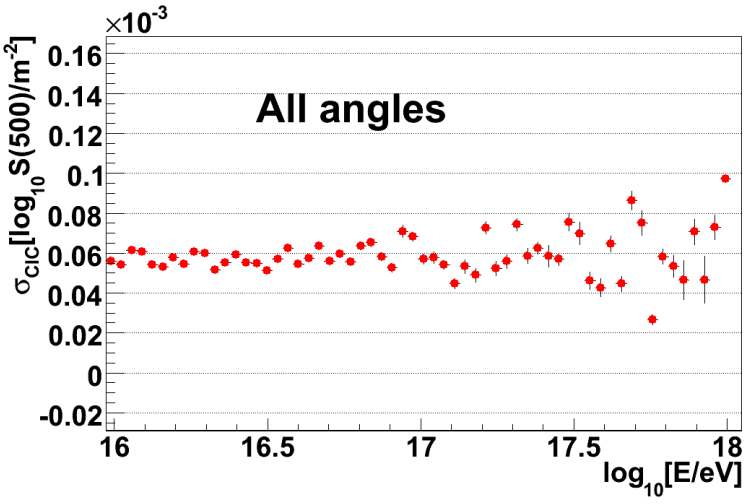

Figure 5.21: Uncertainty induced by the CIC method to the corrected $S(500)$ observable as a function of the true primary energy available from simulations (the CIC uncertainty seems not to depend on the primary energy).

Chapter 6

Reconstruction of the primary energy spectrum

6.1 Conversion to primary energy

The conversion of the recorded $S(500)$ values to primary energy is done with the help of simulation studies. The procedure to generate simulated EAS events has been described in Section 4.1.1. After correcting the recorded $S(500)$ values for attenuation, we can proceed to convert each value to the corresponding primary energy value by means of a simulation-derived calibration; thus the conversion is applied event-by-event. Fig. 6.1 shows the dependency of the primary energy $\log_{10}E_0$ with the reconstructed $\log_{10}S(500)$ as a scatter plot. The overlayed gray dots are the profile of the distribution and the errors associated with them are the errors of the mean. To build this dependency, only a subsample of the total EAS simulated sample was used. The subsample was built by randomly selecting events so that their resulting spectral index is -3 (which is closer to the real spectral index of cosmic rays in the energy range accessible to KASCADE-Grande). Furthermore only events with zenith angle $\theta \in [18°,24°]$ are used (this was decided having in mind that the reference angle adopted in CIC was 21° and therefore the calibration curve should best describe this angular domain; fig. 6.2 shows the angle dependence of the calibration curve). The continuous line in fig. 6.1 is a power law fit of the dependency (eq. 6.1). Since the primary energy spectrum is expected to exhibit a power law behavior and the $S(500)$ is mapping the primary energy, the choice for the calibration curve was a power law form. The fit is performed only on the data inside the full efficiency range ($\log_{10}[E_0/\mathrm{GeV}]>6.5$). The data close to the upper energy limit is excluded from the fit because it is affected by the loss of statistics at the end of the simulated sample (the systematic effects induced by statistical fluctuations in the calibration curve are evaluated in subsection 6.2.1).

$$E_0 = C \cdot S(500)^{\gamma} \tag{6.1}$$

with:
C - a constant;
γ - slope index of the power law dependency.

Figure 6.3 represents the reconstructed experimental primary energy spec-

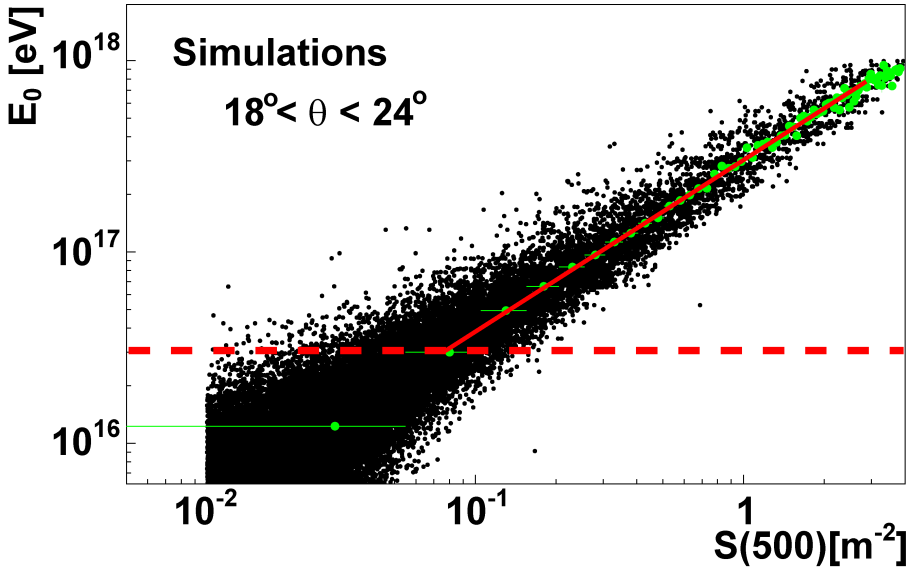

Figure 6.1: E_0 - $S(500)$ correlation (scatter plot, all primaries); the gray dots are the profile of the plot and the continuous line is a power law fit (γ=0.90±0.01, χ^2=2.28); the thick dotted line is the full efficiency energy threshold. *(G. Toma et al. - KASCADE-Grande Collaboration, Proc. 31st ICRC 2009, Łòdż, Poland)*

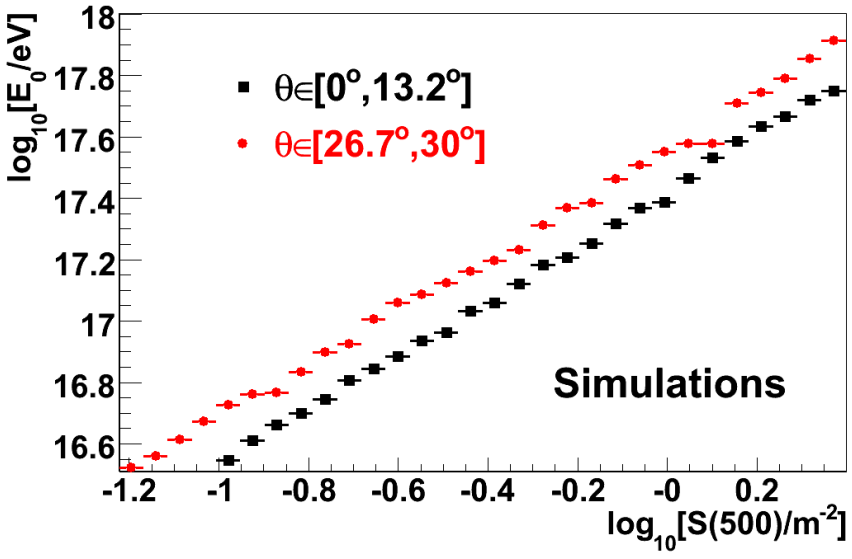

Figure 6.2: $\log_{10}E_0$ - $\log_{10}S(500)$ correlation for different angles of incidence - profile plots (all primaries); this plot shows that the calibration curve is shifted when choosing showers from different angular intervals (because the $S(500)$ is attenuated with increasing zenith angle); this is why the calibration curve must be built only from those events close to the reference angle of CIC, where the attenuation correction of $S(500)$ has been performed.

trum with a power law fit applied. The resulting slope index for the reconstructed energy spectrum is γ=-3.05±0.10 (as anticipated in the previous chapter, the shape and spectral index of the reconstructed energy spectrum are very similar with those of the S(500), since S(500) is mapping the primary energy). The spectrum is noticeably harder than the one predicted by a pure rigidity dependent model [34] and therefore seems to favor an extension of the galactic spectrum towards higher energies (∼10^{18} eV). The plot in fig. 6.4 represents the experimental energy spectra of events coming from different zenith angular bins (log scales are used). The same plots are then multiplied by E_0^3 and are plotted separately in fig. 6.5.

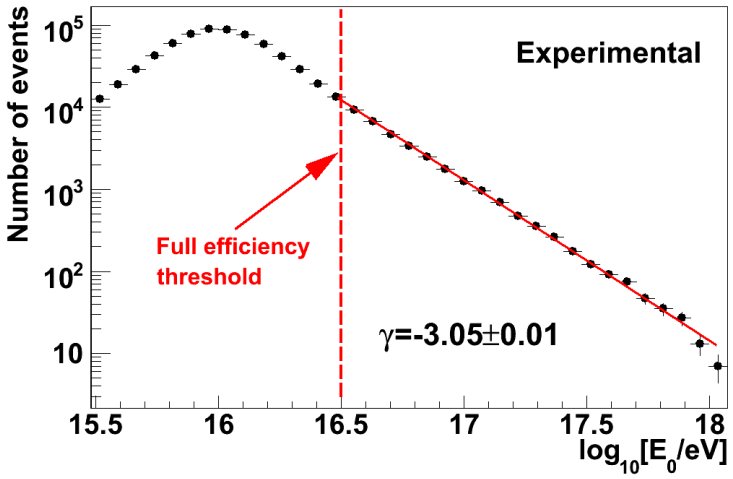

Figure 6.3: Reconstructed energy spectrum (the straight line is a power law fit the resulting power index is γ=-3.05±0.01).*(G. Toma, private communications of the KASCADE-Grande collaboration, 2008)*

6.2 Tests of reconstruction accuracy

6.2.1 Fluctuations of the flux

An important property of the reconstructed primary energy spectrum is the uncertainty affecting it. The statistical uncertainty is calculated easily assuming a Poissonian distribution of data in every energy bin. Thus the statistical error bars for a bin i is equal to the square root of the bin value (eq. 6.2). Normalization to area, time and solid angle is applied to the statistical errors as it is applied to the flux value itself.

$$\sigma(\Phi_i) = \sqrt{n_i} \tag{6.2}$$

Next we intend to evaluate the fluctuations of the flux value. These fluctuations originate from the variation of certain parameters characterizing the reconstruction

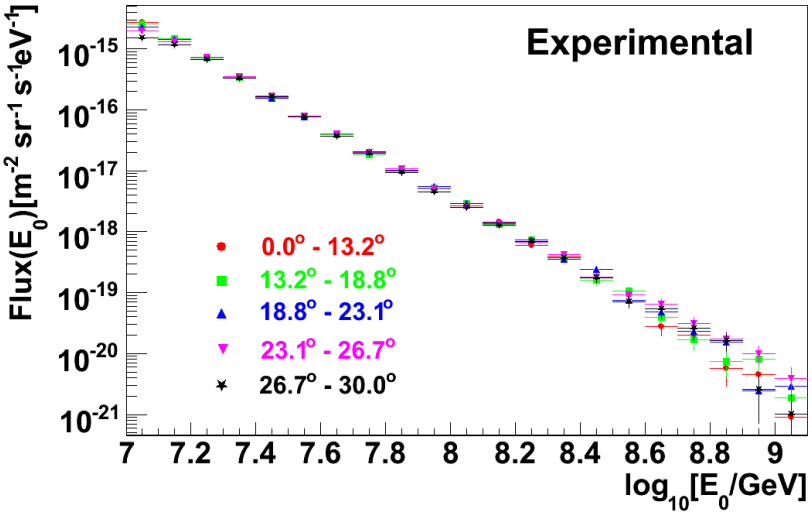

Figure 6.4: Flux for different solid angle bins (normalized to area, solid angle and time).

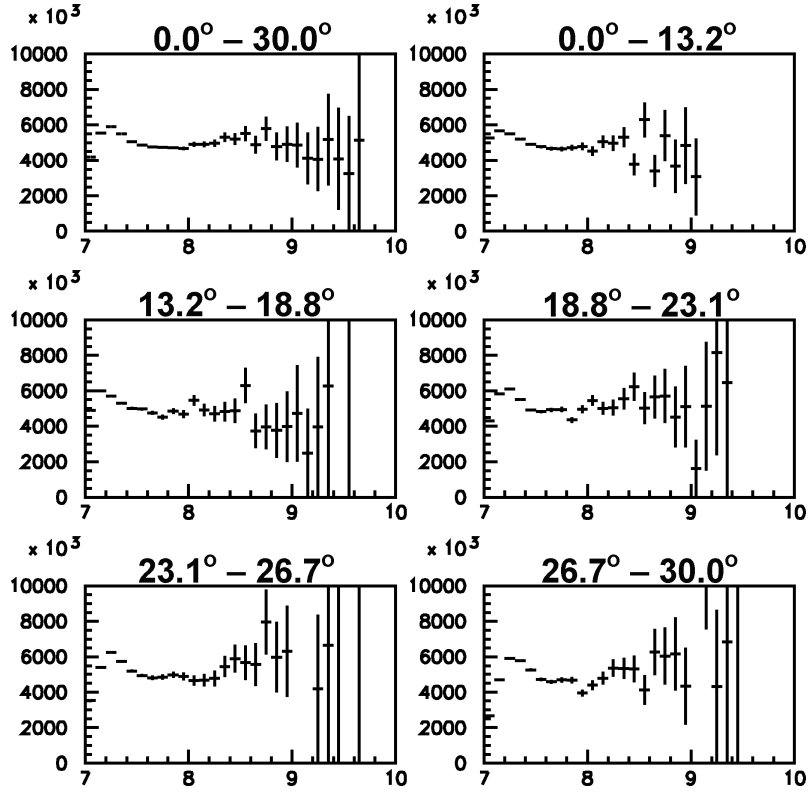

Figure 6.5: Energy spectra for increasing zenith angles, multiplied by E^3.

procedure. Thus, certain such parameters can vary arbitrarily and lead to fluctuations of the obtained flux. We identify such free parameters and estimate their contribution to the total fluctuation:

- the power law fit of the profile E_0 vs. $S_{ref}(500)$;
- the spectral index of the simulated event sample;
- influence of the Monte-Carlo statistics on the fit parameters;
- the systematic error of the corrected $S(500)$ itself;
- choosing a specific reference angle for which to perform the $S(500)$ correction of attenuation.

In order to evaluate the fluctuation induced to the energy flux by each of these factors, they have been allowed to change and the resulting variation of energy flux in % was evaluated.

a. the power law fit of the profile E_0 vs. $S_{ref}(500)$;

The profile of the E_0 vs. $S_{ref}(500)$ distribution is fitted with a power law in order to construct a calibration curve for energy reconstruction (as mentioned in the previous section). This fit is characterized by its defining parameters and their associated uncertainties. In order to evaluate the flux systematic uncertainty induced by this parameterization, the fit parameters were allowed to be changed according to their uncertainty and the primary energy spectrum has been reconstructed in this particular cases. A <1% deviation in energy flux has been introduced by this change in comparison to the standard reconstruction (fairly constant over the entire energy range).

b. the spectral index of the simulated event sample;

The full simulated shower sample used for the tuning of experimental reconstruction had a primary energy spectrum with a spectral index of -2, as opposed to the natural index of the cosmic ray spectrum of ≈-3. In order to evaluate the flux uncertainty introduced by this factor, a simulated sub-sample of showers has been constructed from the total one, in which the spectral index of the energy spectrum was equal to -3 (for this, showers were randomly selected). Te new sub-sample was used to construct a new E_0 vs. $S_{ref}(500)$ parameterization and the primary energy spectrum has been reconstructed in this particular case. A <1% deviation in energy flux has been introduced by this change in comparison to the standard reconstruction (fairly constant over the entire energy range).

c. influence of the Monte-Carlo statistics on the fit parameters;

The simulated shower sample used for energy calibration is generated by a Monte-Carlo algorithm which introduces fluctuations differently for different energy ranges, since the energy spectrum is a power law and at high energies there are much less events available for analysis than at lower energies. In order to estimate the effect of these fluctuations, the energy range is divided into several sub-ranges and the energy calibration is performed for every sub-range. The new parameterizations will vary

slightly from one case to the other due to Monte-Carlo fluctuations. A reconstruction is being performed in the particular case of such a parameterization and the result is compared to the standard reconstruction. A ≈7% deviation in energy flux has been introduced by this change in comparison to the standard reconstruction (fairly constant over the entire energy range).

d. the systematic error of the corrected $S(500)$ itself;

The CIC method introduces an uncertainty on the corrected $S(500)$ (see previous section) and that uncertainty is expected to act as a source of systematic uncertainty on the reconstructed energy spectrum. To evaluate the effect of this source, the attenuation corrected $S(500)$ is allowed to change according to the value of its uncertainty and the primary energy spectrum is reconstructed again in this particular case. A <1% deviation in energy flux has been introduced by this change in comparison to the standard reconstruction (fairly constant over the entire energy range).

e. choosing a specific reference angle to which to perform the $S(500)$ correction of attenuation.

When correcting the $S(500)$ for attenuation, a certain reference angle is chosen. Since the experimental zenith angular distribution is peaked at 21°, this angle was chosen to be 21° in order to let the CIC method to significantly affect as few showers as possible. However it is possible to choose another angle as well without changing the relevance of the end result. In practice this would however affect the value of the reconstructed flux and thus the choosing of a reference angle acts as a source of systematic uncertainty. In order to evaluate the contribution of this source, new reference angles are used for the CIC method. By comparing the deviations from the standard reconstruction we can evaluate the contribution of this uncertainty source. A ≈6% deviation in energy flux has been introduced by this change in comparison to the standard reconstruction (fairly constant over the entire energy range).

The above sources introduce a combined systematic uncertainty of ≈14% in the energy flux at E_0=10^{17} eV. The contributions are fairly constant over the entire full efficiency range. Table 6.1 shows separately the statistical and systematic uncertainty for every energy bin in Fig. 7.1.

6.2.2 Reconstruction accuracy

In order to evaluate the reconstruction accuracy we will directly compare the reconstructed primary energy with the true one from simulations. For this, the reconstruction procedure (SHOWREC+CIC) is applied to the full simulated events sample (as discussed in Chapter 5) and a direct comparison is performed between the true and reconstructed primary energy for the full simulated events. As mentioned in Chapter 4, the reconstruction procedure is identical for full simulated and experimental showers therefore in the two cases we have the same level of consistency.

Fig. 6.6 presents a comparison between the reconstructed primary energy E_{rec}

log(E$_0$/GeV)	Flux [m^{-2}s^{-1}sr^{-1}eV^{-1}]	Statistical uncertainty	Systematic uncertainty
7.55	7.270E-17	5.889E-19	1.090E-17
7.65	3.631E-17	3.709E-19	5.447E-18
7.75	1.829E-17	2.346E-19	2.744E-18
7.85	9.612E-18	1.516E-19	1.441E-18
7.95	4.808E-18	9.556E-20	7.213E-19
8.05	2.499E-18	6.141E-20	3.749E-19
8.15	1.263E-18	3.890E-20	1.894E-19
8.25	6.453E-19	2.478E-20	9.680E-20
8.35	3.546E-19	1.637E-20	5.319E-20
8.45	1.747E-19	1.024E-20	2.621E-20
8.55	8.205E-20	6.256E-21	1.230E-20
8.65	4.509E-20	4.133E-21	6.764E-21
8.75	2.287E-20	2.624E-21	3.431E-21
8.85	1.123E-20	1.639E-21	1.685E-21
8.95	5.507E-21	1.023E-21	8.261E-22

Table 6.1: Energy flux, statistical and systematic uncertainty for every energy bin in fig. 7.1.

and the true primary energy E_0 for a simulated shower sample. The quality is presented in the form of a factor as in eq. 6.3.

$$Q_E = \frac{log_{10}E_{rec} - log_{10}E_0}{log_{10}E_0} \tag{6.3}$$

There are two cases depicted, the case of the entire simulated shower sample (zenith angle $\theta \in [0^o,30^o]$) and showers with their zenith angle close to the reference angle of CIC, 21° ($\theta \in [18^o,23^o]$). The error bars in the plot are errors on the spread and can be regarded as energy resolution. We can see that the energy resolution is of about 20% fairly constant over the entire full efficiency range (slowly improving towards higher energies). These plots show a tendency of systematic underestimation for small energy events. This behavior seems to be consistent with the tendency in fig. 4.18 where the value of the reconstructed $S(500)$ itself was underestimated. At its maximum, the underestimation is comparable to the energy resolution. It is important to remember that the comparison between fig. 6.6 and fig. 4.18 should be a qualitative one, since in the case of fig. 4.18, as mentioned in Chapter 4, the detector interaction was not fully simulated. The tendency to underestimate the particle density at large radial ranges for small events is due to the features of the lateral particle density distribution of these events. Thus, for small showers, the lateral particle density dies quicker at larger radial ranges and the EAS event reaches the detector level with only few or no particles at such ranges. The lateral particle density distribution is thus composed only from the very steep region close to shower core. The Linsley fit function describes this radial range accordingly and finds a set of fit parameters that are best suited for a steep slope (according to the recorded data). Such parameters innevitably lead to underestimated particle densities at larger radial ranges (where there was no data to steer the fit). In fact

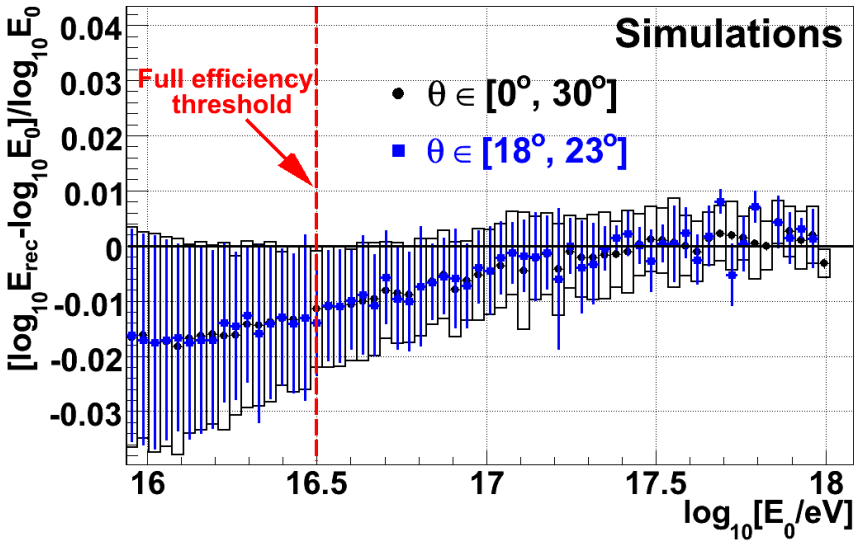

Figure 6.6: Comparison between the reconstructed primary energy E_{rec} and the true energy E_0; the plot represents the profile of the Q_E (eq. 6.3) vs. E_0 scatter plot and the error bars are the error on the spread; the case of two zenith angular bins is depicted.*(G. Toma, private communications of the KASCADE-Grande collaboration, 2008)*

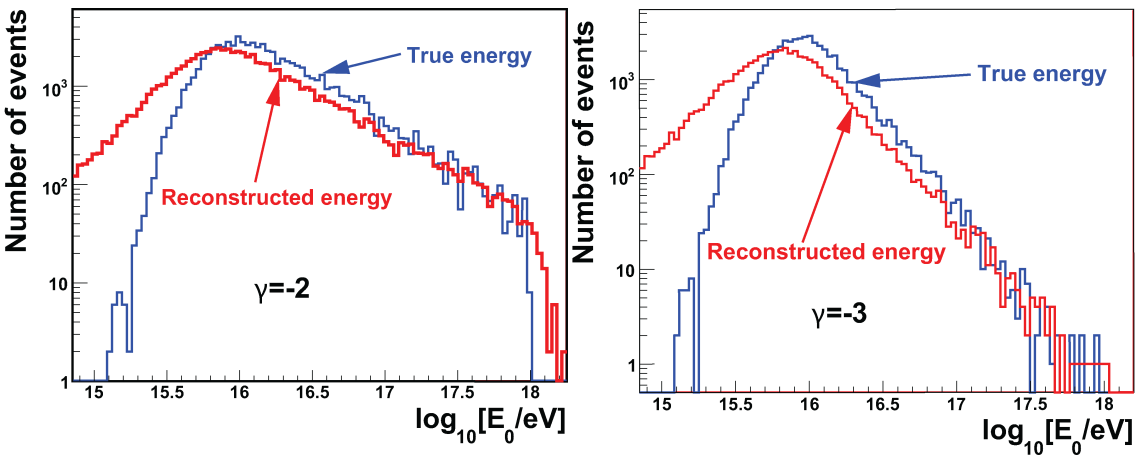

Figure 6.7: True and reconstructed primary energy spectrum for the entire simulated shower sample *(left)* and primary energy spectra for a subsample of the simulated shower sample (subsample with spectral index -3) *(right)*.

this is not necessarily a feature of the Linsley function, but rather a feature of the reconstruction technique as a whole. Thus, even with other parameterizations (as those described in Chapter 4), we would see the same effect [91]. For higher energy events (E_0>10^{17} eV), the systematic underestimation decreases and there is a good agreement between the reconstructed data and the true one. This improvement is hinting that high energy events (triggering more detector stations, especially at larger radial ranges) produce lateral density distributions that are less likely to produce the systematic underestimation.

The same tendency for underestimation of some low energy events is visible

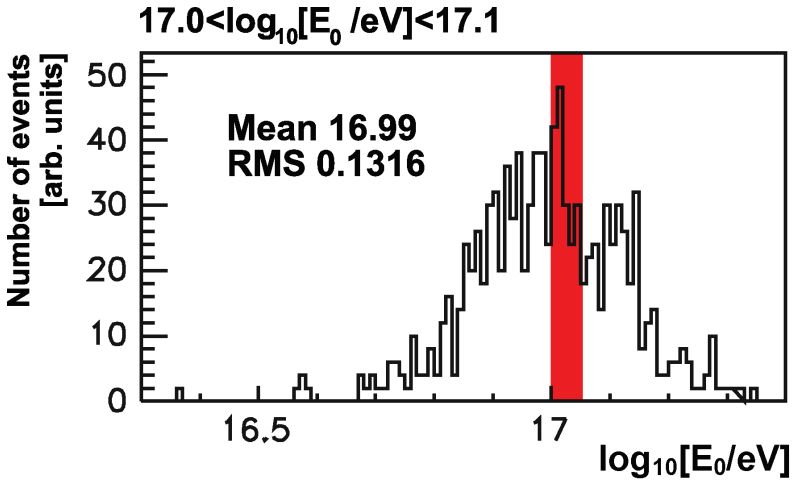

Figure 6.8: The plot shows the distribution of reconstructed primary energy (simulations) for events having their true primary energy in the $\log_{10}[E_0/eV]$ ∈[17,17.1] range.*(G. Toma, private communications of the KASCADE-Grande collaboration, 2008)*

in fig. 6.8. This plot is the direct comparison of true versus reconstructed energy spectra for the simulated shower sample. Two cases are displayed, the case of all events available from simulations, energy spectrum index -2 (left) and the case of a sub-sample with energy spectrum index -3 (right). The events that have their energy underestimated are visible in the spectrum tail towards lower energies, where there is no contribution in the true spectrum.

Additionally to the comparisons in previous plots, Appendix E shows the fluctuations of reconstructed energy values for narrow bins of primary true energy. Figure 6.8 presents such a plot for the particular case of primary true energy in the $\log_{10}[E_0/eV]$ ∈[17,17.1] range (the true energy bin is presented as a gray band).

6.3 Methods cross-check

The reconstructed energy spectrum presented in this thesis is the result of a reconstruction chain that functions independently from the standard one (Chapter 4). A second reconstruction method has been applied to the experimentally recorded

EAS sample and the primary energy spectrum has been inferred from the N_{ch} - N_{μ} correlation (i.e. the correlation between the number of charged particles and the number of muons) [101]. A comparison of the two results is presented in figures 6.9 and 6.10 (the KASCADE spectrum obtained for lower energies 10^{15} eV-10^{17} eV is presented also for comparison). Figure 6.10 shows the spectra multiplied by $E_0^{2.5}$.

The two spectra start from different minimum energies due to the different

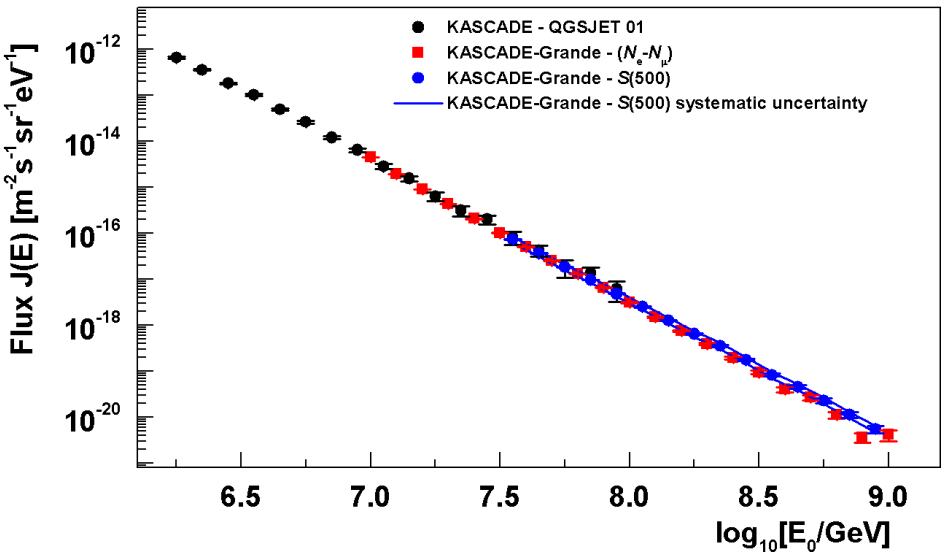

Figure 6.9: Reconstructed experimental energy spectrum by KASCADE-Grande from $S(500)$/CIC (gray round dots) along with results from the N_{ch} - N_{μ} dependence (squared dots) and the previous results of KASCADE (round black dots); the continuous lines above and below the $S(500)$ derived spectrum are the error envelopes and show the systematic uncertainties; the statistical errors are presented with lines for each of the spectra and are dot sized.*(G. Toma, private communications of the KASCADE-Grande collaboration, 2008)*

full efficiency thresholds of the two methods (it has been shown in Chapter 5 that the relevant energy range for the reconstruction of energy spectrum from $S(500)$ starts from $\log_{10}[E_0/\text{GeV}]\approx 7.5$). The $S(500)$ derived spectrum is slightly shifted towards higher energy values($E_0 > 10^{17}$ eV). At lower energies the two spectra overlap, but at these energies we expect that the $S(500)$ derived spectrum is systematically underestimated. Thus, on average, there is a systematic shift between the $S(500)$ derived energy flux and the one derived from the N_{ch} - N_{μ} correlation. The systematic between the two results appears to be larger than the size of the systematic uncertainty band. A significant contribution to this shift could be induced by features of the E_0 - $S(500)$ calibration function and could indicate that the simulations do not describe the shape of the lateral density distributions with sufficient accuracy. Both spectra are mass insensitive, but they are based on simulation derived assumptions. It is therefore possible that the present results will change if the assumed model for

high energy interactions (QGSJETII) is changed.

Regarding the underestimation of the $S(500)$ derived spectrum at lower en-

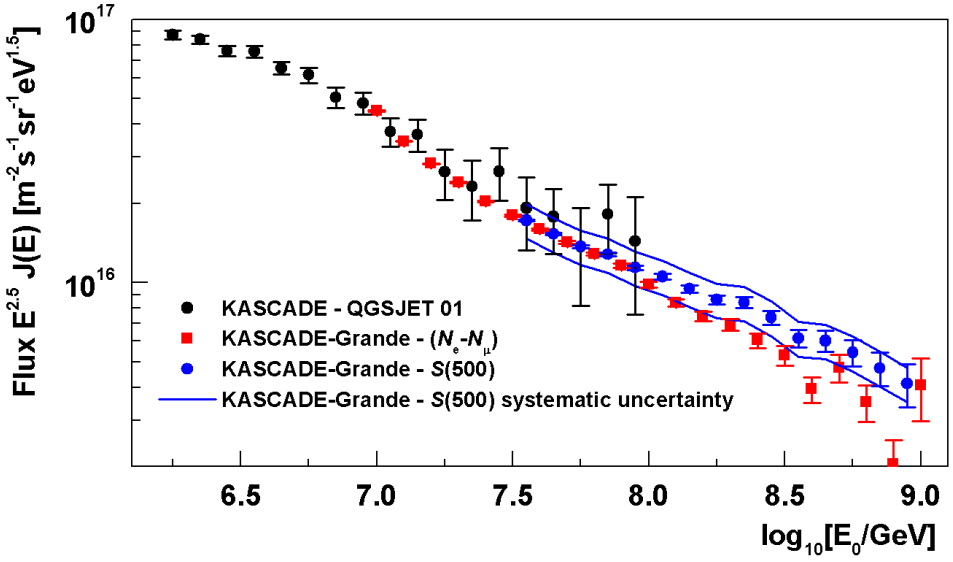

Figure 6.10: Same as the previous plot but the fluxes are here multiplied with $E_0^{2.5}$ in order to make spectral features more visible.

ergies we envisage a method of correcting the result by the application of a response matrix. We are representing the flux as a histogram in which we store data in every bin according to the reconstructed energy. The mis-reconstruction of an event (by under- or over-estimation) may lead to the storing of that particular event in the wrong (neighboring) energy bin. Thus in every energy bin of our spectrum we will have the data correctly belonging to that bin, but also data that was migrating from neighboring bins. Assuming that we have only statistical mis-reconstructions, as the energy spectrum is very steep we expect that for a given energy bin, the mis-reconstructed events falling into it will be coming predominantly from lower energy bins. The systematic effects are contributing additionally to this migration effect. It is possible to account for these by calculating (from simulations) how many events migrate in this way and where they add their contribution. In fact, this is done with the help of a response matrix. This correction technique is subject of future investigations but is presented in more detail in Appendix G along with a very preliminary result of its application on the data.

Chapter 7

Conclusions and outlook

The aim of this thesis is the investigation of one of the most important aspects of cosmic ray physics, the features of the primary energy spectrum of cosmic rays. In this paper the primary energy spectrum has been obtained by analyzing the particle density distributions in EAS and their arrival times for events recorded with the KASCADE-Grande detector. The method has been applied for EAS events generated by primaries in an energy range that is not suited for direct observations (i.e. the energy range accessible by the KASCADE-Grande detector array, 10^{16} eV - 10^{18} eV). The study includes also an extensive investigation of simulated events. The reconstruction procedure is based on the SHOWREC reconstruction code (developed by the Romanian partner in the KASCADE-Grande collaboration and to which the author has brought fundamental contributions). In the following we present an outlook on the applied procedure emphasizing its advantages and limitations, the obtained results and the prospects for future improvement.

The method. The reconstruction procedure consists of several steps and starts from the energy deposits of particle in detectors and the corresponding arrival times. The arrival times are used in order to reconstruct the arrival direction of the EAS event, a geometrical property that is vital for any other further investigation. Energy deposits of particles are converted into particle numbers by the use of lateral energy correction functions. The lateral energy correction functions take into account the angle of incidence of particles in detectors and are obtained from parameterizations of energy deposits, a technique that greatly accelerates the reconstruction procedure. The particle density distributions were approximated with a Linsley LDF and the particle density at 500 m from shower core has been reconstructed (an observable that was found to be a good primary energy estimator for the case of the KASCADE-Grande array). The attenuation effects characteristic for inclined showers have been corrected by applying the CIC method on the recorded $S(500)$ and then, by employing a simulation-derived calibration of E_0 with $S(500)$ the primary energy spectrum of the experimentally recorded EAS sample has been reconstructed. The study was performed identically on simulated events. Thus it was possible to evaluate the efficiency of the reconstruction by directly comparing the true primary energy (that is available in simulations) with the reconstructed one. The reconstructed primary energy spectrum has been normalized to detection area, time and solid angle. The fluctuations of the reconstructed flux induced by various factors have been evaluated.

Advantages and limitations. One of the main advantages of the technique is that it is designed to function independently from the standard reconstruction chain applied at KASCADE-Grande. This allows for cross-checks between the results of the two chains and thus for relevant consistency tests. Another key feature of the applied procedure is its speed. Thus, the reconstruction relies on lateral energy correction functions that are parameterized from simulated energy deposits (full simulations of energy deposits are performed only once). This way the reconstruction is greatly accelerated with practically no loss in quality. Another strength comes from the fact that the method relies entirely on recorded data for program input, performing no extrapolations on data recorded by KASCADE towards radial ranges comparable to the Grande array (i.e. the methods using the reconstructed muon number N_μ calculate this number by such an extrapolation because N_μ is possible to measure directly only with the smaller KASCADE array). On the limitations side it has been shown that the method is sensitive to the lateral density distribution shape and structure. It was observed that for events initiated by lower energy primaries there is a tendency of underestimation of $S(500)$ and implicitly of the reconstructed primary energy. This is linked with the lack of information at ranges $\approx$500 m for small events, or with very small energy deposits in this radial range. This tends to bias the Linsley fit towards lower values. Additionally the full efficiency threshold for the described method is higher as compared to the full efficiency threshold of other reconstruction methods. The increased sensitivity to the shape of the particle density distribution limits also the zenith angular interval of application.

Results. Figure 7.1 shows the reconstructed primary spectrum by KASCADE-Grande from $S(500)$, multiplied by $E^{2.5}$ together with results of other experiments in the energy range accessible to KASCADE-Grande. The spectrum is normalized to time, solid angle and area. The analysis of the reconstructed energy spectrum shows a good agreement with the results of other experiments, notably with the results of the KASCADE experiment operating in the 10^{14} eV - 10^{16} eV range. The small error bars are statistical uncertainties assumed distributed by a Poissonian law. The wider band defined by continuous lines above and below the spectrum represents the fluctuation of the reconstructed flux when certain reconstruction parameters are changed arbitrarily. This band can be regarded as a systematic uncertainty characterizing the reconstructed flux. A cross-check has been performed comparing the result of the described method with the result obtained from the standard reconstruction (figure 6.10). A systematic appears between the results of the two spectra. This is generally larger than the uncertainty band. A significant contribution to this shift could be induced by features of the E_0 - $S(500)$ calibration function and could indicate that the simulations do not describe the shape of the lateral density distributions with sufficient accuracy.

The obtained spectrum is noticeably harder than the one predicted by a pure rigidity model and therefore seems to favor an extension of the galactic spectrum towards energies of $\sim 10^{18}$ eV. One of the main goals of the KASCADE-Grande is to search for the predicted "iron knee". The first investigation of spectral shape around few times 10^{17} eV reveals no obvious feature, a result that could indicate a mixed galactic composition in that energy range. However the search of spectral features is still open as further refinements of the reconstruction are still possible.

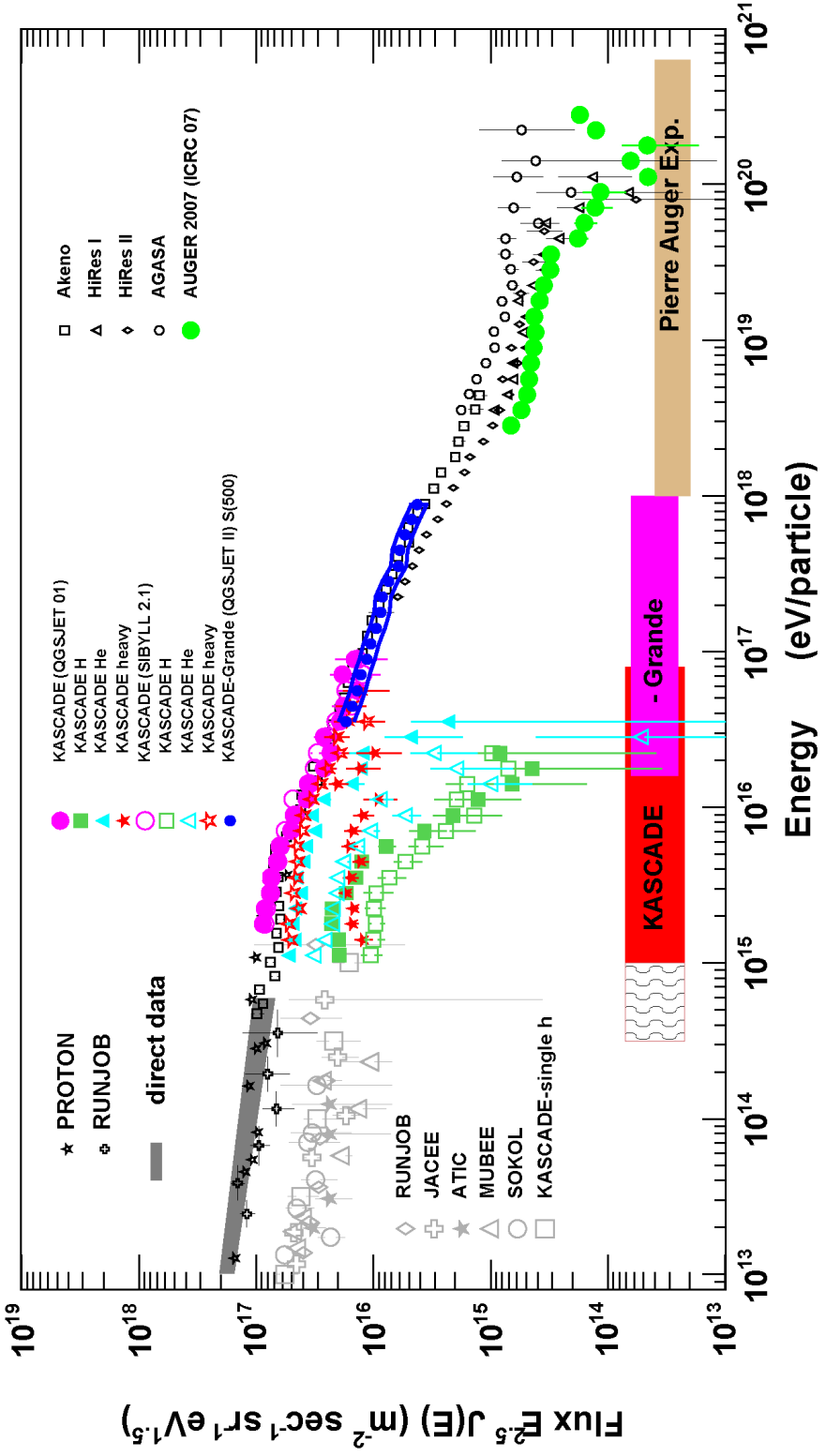

Figure 7.1: Reconstructed experimental energy spectrum by KASCADE-Grande from $S(500)$/CIC, multiplied by $E^{2.5}$ along with results of other experiments; the continuous lines above and below the $S(500)$-derived spectrum show the systematic uncertainties. *(G. Toma et al. - KASCADE-Grande Collaboration, Proc. 31st ICRC 2009, Lòdż, Poland)*

As KASCADE-Grande is acquiring more data, also the statistical quality of the future event sample will improve.

Prospects for improvement. A possibility to improve the present result is that of correcting the systematic underestimation of reconstructed data at lower energies. A technique to account for this is to employ a response matrix and thus shift the mis-reconstructed events into the correct bin in the energy spectrum. This method corrects also the effect of the statistical fluctuations. A preliminary investigation has shown promising results (see Appendix G), but needs more refinements.

Another possibility for significantly improving the results would be to recalculate the lateral energy correction functions by taking into account also the metal hut and concrete base of the Grande stations, thus giving a better description of particle energy deposits in detectors. Electrons and photons account for most of the secondaries in an EAS and their energy deposit spectrum changes significantly when accounting for the detector hut. Thus it is expected that the new energy deposit simulation would affect the value of reconstructed particle densities in stations and indirectly the $S(500)$ and the primary energy.

Acknowledgements

This thesis is the result of extensive and complex investigative efforts that have been supported and enabled by several groups of research institutions and organizations. I would like to thank first my supervising professor, Prof. Dr. Octavian Sima whose guidance and collaboration was invaluable in the entire duration of the project. A considerable part of this work, especially that concerning the experimental aspects of the investigation has been performed at the site of the KASCADE-Grande experiment in the frame of a DAAD-sponsored doctoral scholarship. During this period of my research visit in Karlsruhe Institute for Technology I had interaction with many fellow researchers whose help and positive critical attitude greatly facilitated the progress of the investigation. I would like to thank Dr. Andreas Haungs for countless scientific discussions and comments and equally for facilitating my accommodation and co-operation with the colleagues in Karlsruhe Institute for Technology, Campus Nord. I thank also Prof. Dr. Heinigerd Rebel and Dr. Iliana Brancus for the active collaboration in this project and for their helpful guidance. Also I would like to thank all members of the KASCADE-Grande collaboration for their constructive attitude, always ready for help and guidance and last but not least I emphasize the fair collaborative spirit. In particular, I would like to mention the fruitful interaction with Dr. Juan Carlos Arteaga Velasquez, Dr. Fabiana Cossavella and Dr. Donghwa Kang. For the financial support during this research activity I have to thank the Romanian Ministry of Education, Research, Youth and Sport and also the Deutscher Akademischer Austausch Dienst as a substantial part of this investigation has been performed in the frame of a DAAD-sponsored doctoral scholarship (A/06/09016 Ref.322). I would like to thank the National Institute for Physics and Nuclear Engineering - Horia Hulubei (IFIN-HH) for hosting an important part of the research activities in Romania. Finally I express special thanks to my family for the warm support and patience during this work.

The KASCADE-Grande experiment is supported by the BMBF of Germany, the MIUR and INAF of Italy, the Polish Ministry of Science and Higher Education, and the Romanian Ministry of Education, Research, Youth and Sport.

Bibliography

[1] V.Hess, Z.Phys. 12 (1911) 998; Z.Phys. 13 (1912) 1084

[2] P. Auger, R. Maze and T. Grivet Mayer, Compt.Rend.Acad.Sci. 206 (1938) 1721

[3] W. Kohlhörster, I. Matthes and E. Weber, Naturwisssenschaften 26 (1938) 576

[4] J. A. Simpson, Ann. Rev. Nucl. Part. Sci. 33 (1983) 323

[5] B.Wiebel-Sooth, P. L. Biermann and H. Meyer, Astron. Astrophys. 330 (1998) 389

[6] J. Abraham et al. - Pierre Auger Collaboration, Astropart. Phys. 29 (2008) 243

[7] E. Fermi, Phys. Rev. 75 (1949) 1169

[8] L. O. Drury, Rep. Prog. Phys. 46 (1983) 973

[9] C. J. Cesarsky and T. Montmerle, Space Sci. Revs. 36 (1983) 173

[10] J. R. Jokipii and G.Morfill, Astrophys. J. 312 (1987) 170

[11] A. K. Harding and T. K. Gaisser, Astrophys. J. 358 (1990) 561

[12] J. P. Rachen and P. L. Biermann, Astron. Astrophys. 272 (1993) 161

[13] K. S. Cheng, C. Ho and M. Ruderman, Astrophys. J. 300 (1986) 500

[14] G. Sigl, Ann. Phys. 303 (2003) 117

[15] G.V. Kulikov and G.B. Khristiansen, Sov. Phys. JETP 35 (1959) 441

[16] J. Hörandel, Astropart. Phys. 21 (2004) 241

[17] E. G. Berezhko and L. T. Ksenofontov, J. Exp. Theor. Phys. 89 (1999) 391

[18] T. Stanev, P. L. Biermann and T. K. Gaisser, Astron. Astrophys. 274 (1993) 902

[19] K. Kobayakawa, Y. Sato and T. Samura, Phys. Rev. D66 (2002) 083004

[20] V. S. Ptuskin, Astron. Astrophys. 268 (1993) 726

[21] J. Candia, E. Roulet and L. N. Epele, JHEP 12 (2002) 033

[22] A. D. Erlykin and A. W. Wolfendale, J. Phys. G23 (1997) 979

[23] R. Wigmans, Nucl. Phys. Proc. Suppl. 85 (2000) 305

[24] D. Kazanas and A. Nicolaidis, arXiv:astro-ph/0103147v2

[25] S. P. Knurenko et al., Nucl. Phys. Proc. Suppl. 151 (2006) 92

[26] M. Ave et al., Astropart. Phys. 19 (2003) 61

[27] D. J. Bird et al. - HIRES Collaboration, Astrophys. J. 424 (1994) 491

[28] T. Abu-Zayyad et al. - HiRes-MIA Collaboration, Astrophys. J. 557 (2001) 686

[29] M. Nagano et al., J. Phys. G18 (1992) 423

[30] M.A. Lawrence et al., J. Phys. G Nucl. Part. Phys. 17 (1991) 773

[31] G. Agnetta et al., Nucl. Intrum. Methods 359 (1995) 596

[32] M. Takeda et al., Astropart. Phys. 19 (2003) 447

[33] V.S. Berezinsky, S.I. Grigorieva, B.I. Hnatyk, arXiv:astro-ph/0403477v2

[34] A.M. Hillas, J. Phys. G: Nucl. Part. Phys. 31 (2005) R95

[35] K. Greisen, Phys. Rev. Lett. 16 (1966) 748

[36] G. T. Zatsepin and V. A. Kuzmin, JETP Lett. 4 (1966) 78

[37] A. Haungs, H. Rebel and M. Roth, Rep. Prog. Phys. 66 (2003) 1145

[38] A. Haungs et al. - KASCADE-Grande collaboration, Proc. 28th ICRC 2003, Tsukuba, vol. 2, p. 985

[39] A.M. Hillas et al., Proc. 12th ICRC 1971, Hobart, vol. 3, p. 1001

[40] H.Rebel,..., G.Toma et al. - KASCADE-Grande Collaboration, Proc. 29th ICRC 2005, Pune, vol. 6, p. 297

[41] O. Sima, I.M. Brancus, H. Rebel and A. Haungs, Report FZKA 6985, Forschungszentrum Karlsruhe 2004

[42] F. Cossavella,..., G.Toma et al. - KASCADE-Grande Collaboration, Proc. 30th ICRC 2007, Merida, vol. 4, p. 211

[43] R. Glasstetter,..., G.Toma et al. - KASCADE-Grande collaboration, Proc. 29th ICRC 2005, Pune, vol. 6, p. 293

[44] J. Linsley et al., Journ. Phys. Soc. Japan 17 (1962) A-III

[45] M. Nagano et al., J.Phys G Nucl.Phys. 10 (1984) 1295

[46] D.M. Edge et al., J. Phys. A Math. Nucl. Gen. 6 (1973) 1612;
Y. Dai et al., J.Phys.G Nucl. Part. Phys. 14 (1998) 793;
M. Roth et al.- Pierre Auger Collaboration, Proc. 28th ICRC 2003, Tsukuba, vol. 2, p. 333

[47] H.Y. Dai et al., J. Phys. G Nucl. Phys. 14 (1988) 793

[48] M. Roth et al. - Pierre Auger Collaboration, Proc. 30th ICRC 2007, Merida, vol. 4, p. 327

[49] P. Auger et al., Rev. Mod. Phys. 11 (1939) 288

[50] T. Antoni et al. - KASCADE collaboration, Astropart. Phys. 15 (2001) 149
W.D. Apel,..., G. Toma et al. - KASCADE-Grande collaboration, Astroparticle Physics 29 (2008) 317

[51] W.D. Apel et al. - KASCADE-Grande Collaboration, Astropart.Phys. 31 (2009) 86

[52] T. Antoni et al. - KASCADE Collaboration, Astropart.Phys. 14 (2001) 245

[53] H. Rebel, Progr.Part.Nucl.Phys 46 (2001) 109

[54] Pierre Auger Project Design Report 1997, Pierre Auger Collaboration, Fermi National Accelerator Lab., www.auger.org/admin

[55] M.T. Dova et al. - Pierre Auger Collaboration, Proc. 27th ICRC 2001, Hamburg, vol. 2, p. 699

[56] I.M. Brancus,..., G.Toma et al. - KASCADE-Grande Collaboration, Proc. 29th ICRC 2005, Pune, vol.6, p. 361

[57] G. Toma et al. - KASCADE-Grande Collaboration, Proc. 31st ICRC 2009, Łòdż
G. Toma et al. - KASCADE-Grande Collaboration, Nuclear Physics B (Proceedings Supplements) 196 (2009) 247

[58] A. Haungs,..., G.Toma et al.- KASCADE-Grande Collaboration, Proc. 31st ICRC 2009, Łòdż, arXiv:0910.4824v1 [astro-ph.HE]

[59] G. Navarra et al. - KASCADE-Grande collaboration, Nucl.Instr. and Meth. A 518 (2004) 207
D. Kang,..., G. Toma et al. - KASCADE-Grande collaboration, Modern Physics Letters A (2009) in press

[60] T. Antoni et al. - KASCADE Collaboration, Nucl.Instr. and Meth. A 513 (2003) 429

[61] M. Aglietta et al. - EAS-TOP Collaboration, Nucl.Instr. and Meth. A 336 (1993) 310

[62] H. Falcke,..., G.Toma et al. - LOPES Collaboration, Nature 435 (2005) 313
K.-H. Kampert,..., G.Toma et al. - KASCADE-Grande Collaboration, Nucl. Phys. B (Proc. Suppl.) 190 (2009) 213
A. Haungs,..., G. Toma et al. - LOPES Collaboration, Modern Physics A vol. 21 Suppl. 1 (2006) 182

[63] A. Haungs,..., G. Toma et al. - LOPES collaboration, Nucl. Instrum. Methods A 604 (2009) S236

[64] G. Toma et. al, Rom. Rep. Phys. 56 (2004) 741-748

[65] G. Toma et. al, Rom. Rep. Phys. 57 (2005) 334-341

[66] I.M. Brancus,..., G. Toma et al., Int. J. Mod. Phys. A, Vol. 20 No. 29 (2005) 6784-6786

[67] D. Heck et al., Report FZKA 6019, Forschungszentrum Karlsruhe 1998

[68] CERN program library, *GEANT user's guide* (1997)
http://cernlib.web.cern.ch/cernlib/

[69] J. Ranft, Phys. Rev. D 51 (1995) 64

[70] J.N. Capdevielle et al., Report KfK 4998, Kernforschungszentrum Karlsruhe 1992

[71] N.N. Kalmykov and S.S. Ostapchenko, Yad. Fiz. 56 (1993) 105; Phys. At. Nucl. 56 N3 (1993) 346;
N.N. Kalmykov, S.S. Ostapchenko and A.I. Pavlov, Izv. RAN Ser. Fiz. 58 (1994) N12 21;
N.N. Kalmykov, S.S. Ostapchenko and A.I. Pavlov, Bull. Russ. Acad. Sci. (Physics) 58 (1994) 1966;
N.N. Kalmykov, S.S. Ostapchenko and A.I. Pavlov, Nucl. Phys. B Proc. Suppl. 52B (1997) 17;
S.S. Ostapchenko, private communications (2001)

[72] S.S. Ostapchenko, Nucl. Phys. B Proc. Suppl. 151 (2006) 143 and 147; Phys. Rev. D 74 (2006) 014026

[73] R.S. Fletcher, T.K. Gaisser, P. Lipari and T. Stanev, Phys. Rev. D50 (1994) 5710;
J. Engel, T.K. Gaisser, P. Lipari and T. Stanev, Phys. Rev. D46 (1992) 5013

[74] R. Engel, T.K. Gaisser, P. Lipari and T. Stanev, Proc. 26th ICRC 1999, Salt Lake City, vol.1, p. 415;
R. Engel, private communications

[75] K. Werner, Phys. Rep. 232 (1993) 87

[76] H.J. Drescher et al., Phys. Rep. 350 (2001) 93

[77] I. Abt et al. - H1 Collaboration, Nucl. Instrum. Meth. A 386 (1997) 310; Nucl. Instrum. Meth. A 386 (1997) 348;
A. Aktas et al. - H1 Collaboration, Phys. Lett. B 638 (2006) 432;
F. D. Aaron et al. - H1 Collaboration, Phys. Lett. B 668 (2008) 268

[78] U. Holm - ZEUS Collaboration, *The ZEUS Detector. Status Report* (unpublished), DESY 1993, http://www-zeus.desy.de/bluebook/bluebook.html;
S. Chekanov et al. - ZEUS Collaboration, Submitted to Phys. Lett. B. [arXiv:0906.1504]

[79] K. Werner, F. M. Liu and T. Pierog, Phys. Rev. C 74 (2006) 044902

[80] A. Fassò et al., CHEP2003 2003, La Jolla, paper MOMT005; eConf C0303241 (2003); arXiv:hep-ph/0306267; http://www.fluka.org/

[81] H. Fesefeldt, Report PITHA-85/02 1985, RWTH Aachen

[82] S.A. Bass et al., Prog. Part. Nucl. Phys. 41 (1998) 225;
M. Bleicher et al., J. Phys. G: Nucl. Part. Phys. 25 (1999) 1859;
http://www.th.physik.uni-frankfurt.de/urqmd/

[83] W.R. Nelson, H. Hirayama and D.W.O. Rogers, Report SLAC 265 (1985), Stanford Linear Accelerator Center;
http://www.slac.stanford.edu/pubs/slacreports/slac-r-265.html;
http://www.irs.inms.nrc.ca/inms/irs/EGS4/get egs4.html

[84] K. Kamata, J. Nishimura, Prog. Theoret. Phys. Suppl. 6 (1958) 93

[85] G. Corcella et al., JHEP 0101 (2001) 010; G. Marchesini et al., Comp. Phys. Comm. 67 (1992) 465; http://hepwww.rl.ac.uk/theory/seymour/herwig/

[86] M. Ambrosio et al., Auger technical note GAP 2003-013 (2003); Proc. 28th ICRC 2003, Tsukuba, 595;
http://www1.na.infn.it/wsubnucl/cosm/auger/activities.html

[87] C. Dobrigkeit, *Estimate of the Arrival Direction of Primary Particles Inducing Air Showers, From Data Obtained by the Top Cluster in the KASCADE Experiment*, FZKA Interner Bericht, Forschungszentrum Karlsruhe 1996

[88] K. Greisen, Prog. Elem. Part. Cosmic Ray Phys. 3 (1956) 1

[89] F. Schmidt and J. Knapp, *CORSIKA Shower Images*
http://www.ast.leeds.ac.uk/~fs/showerimages.html

[90] J.van Buren,..., G.Toma et al. - KASCADE-Grande collaboration, Proc. 29th ICRC 2006, Pune, vol. 6, p. 301

[91] O. Sima,..., G.Toma et al., *The reconstruction of the lateral charge particle distributions and the studies of different LDF parameterisations*, FZKA Interner Bericht KASCADE-Grande 2005-01, Forschungszentrum Karlsruhe 2005

[92] I.M. Brancus,..., G.Toma et al., *Studies of primary energy estimation and mass discrimination of cosmic rays in the region of 10^{17} eV by observing the EAS lateral charged particle distributions with KASCADE-Grande*,FZKA Interner Bericht KASCADE-Grande 2004-02, Forschungszentrum Karlsruhe 2004
I.M. Brancus,..., G.Toma et al., *Event-by-event studies of the lateral distribution of charged EAS particles: observable correlations and non-parametric analyses of multivariate distributions*,FZKA Interner Bericht KASCADE-Grande 2005-02, Forschungszentrum Karlsruhe 2005

[93] G.Toma et al. - KASCADE-Grande Collaboration, Proc. 26th ECRS 2006, Lisbon, so-134

[94] W-M Yao et al 2006 J. Phys. G: Nucl. Part. Phys. 33 1

[95] O. Sima, *Simularea Monte Carlo a transportului radiatiilor*(in Romanian), Editura ALL, ISBN 973-9156-69-X

[96] A.A. Lagutin, A.V. Plyasheshnikov and V.V. Uchaikin, Proc. 16th ICRC 1979., Kyoto, vol. 7, p. 18;
J.N. Capdevielle for KASCADE Collaboration, Proc. 22nd ICRC 1991, Dublin, vol. 4, p. 405

[97] A.A. Lagutin et al., Proc. 25th ICRC 1997, Durban, vol. 6, p. 285

[98] R. Glasstetter et al. - KASCADE-Grande Collaboration, Proc. 28th ICRC 2003, Tsukuba, vol. 2, p. 781

[99] F. Cossavella, Report FZKA 7513, Forschungszentrum Karlsruhe 2009

[100] http://ankaweb.fzk.de

[101] M. Bertaina,..., G.Toma et al. - KASCADE-Grande Collaboration, Proc. 31st ICRC 2009, Łòdż

[102] G.L. Cassidy et al., Rev. Nucl. Part. Sci. 35 (1985) 351

[103] D.J. Bird et al., Phys. Rev. Lett. 71 (1993) 3401

[104] John N Matthews et al. - HiRes Collaboration, Proc. 27th ICRC 2001, Hamburg, vol. 2, p. 350

[105] M. Takeda et al. - AGASA Collaboration, Phys. Rev. Lett. 81 (1998) 1163

[106] B.N. Afanasiev et al., Proc. 24th ICRC 1995, Rome, vol. 2, p. 756

[107] A.A. Chilingaryan et al., Proc. 26th ICRC 1999, Salt Lake City, vol. 1, p. 240

[108] A.V. Daryan et al., Proc. 27th ICRC 2001, Hamburg, vol. 1, p. 273

[109] M. Amenomori et al., Astrophys. J. 461 (1996) 408

[110] C. Bacci et al., Proc. 26th ICRC 1999, Salt Lake City, vol. 5, p. 265

[111] J. Engler et al., Nucl. Instrum. Methods A 427 (1999) 528

[112] A. Haungs et al., Nucl. Instrum. Methods A 372 (1996) 515

[113] H. Bozdog et al., Nucl. Instrum. Methods A 465 (2001) 455

[114] S. Swordy and D. Kieda, Astropart. Phys. 13 (2000) 137

[115] A. Karle et al., Astropart. Phys. 3 (1995) 321

[116] K. Bernlöhr et al., Astropart. Phys. 5 (1999) 139

[117] S.N. Vernov, Proc. 16th ICRC 1979, Kyoto, vol. 8, p. 129

[118] Y.A. Fomin et al., Proc. 22th ICRC 1991, Dublin, vol. 2, p. 85

[119] J.W. Fowler et al., Astropart. Phys. 15 (2001) 49

[120] S.M. Kasahara et al., Phys. Rev. D 55 (1997) 5282

[121] M. Glasmacher et al., Astropart. Phys. 10 (1999) 291

[122] A. Borione et al., Nucl. Instrum. Methods 346 (2000) 682

[123] F. Arqueros et al., Astron. Astrophys. 359 (2000) 682

[124] N. Ito et al., Proc. 25th ICRC 1997, Durban, vol. 4, p. 117

[125] Y. Hayashi et al., Proc. 27th ICRC 2001, Hamburg, vol. 1, p. 111

[126] J.E. Dickinson et al., Proc. 26th ICRC 1999, Salt Lake City, vol. 3, p. 136

[127] R.A. Antonov et al., Proc. 27th ICRC 2001, Hamburg, vol. 2, p. 828

[128] O. Adriani et al., Nucl. Instrum. Methods 488 (2002) 209

[129] O.A. Gress et al., Nucl. Phys. B Proc. Suppl. 75A (1999) 299

[130] E.N. Alexejev et al., Proc. 16th ICRC 1979, Kyoto, vol. 10, p. 276

[131] V.N. Bakatanov et al., Astropart. Phys. 8 (1979) 59

[132] Y. Shirasaki et al., Astropart. Phys. 15 (2001) 357

[133] L.T. Baradzei et al., Nucl. Phys. B 370 (1992) 365

[134] M. Akashi et al., Phys. Rev. D 24 (1981) 2353

[135] J.R. Ren et al., Phys. Rev. D 38 (1981) 1414

[136] M. Ahlen et al., Nucl. Instrum. Methods A 324 (1993) 337

[137] A.M. Hillas, Proc. 17th ICRC 1981, Paris, vol. 8, p. 1993

[138] M. Teshima et al., Nucl. Instrum. Methods A 311 (1992) 338

[139] P. Doll et al., Nucl. Instrum. Methods A 488 (2002) 517

[140] S. Petrera, Nuovo Cimento C 19 (1996) 737

[141] M. Aglietta, Phys. Lett. B 337 (1994) 376

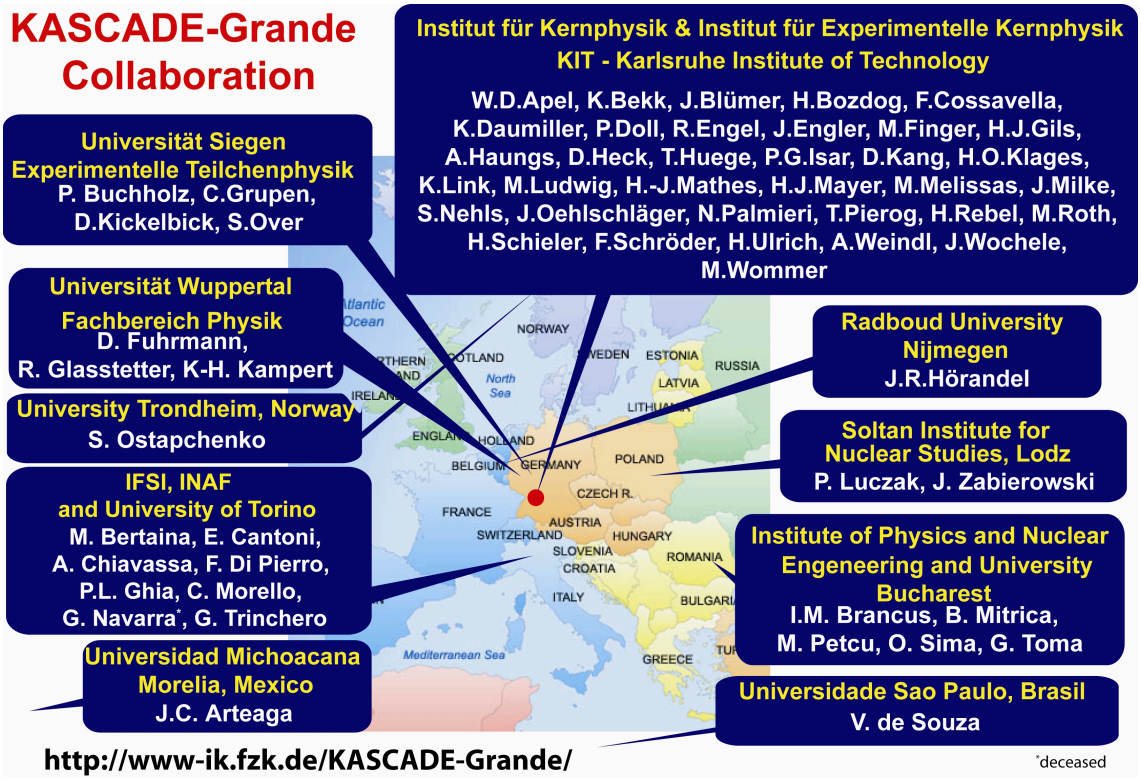

Appendix A

EAS experiments

Experiment	Location	Detector	Observables	References/ operating (Y|N)
CASA	Dugway, Utah, US	Scint. array	N_e	[121]/N
MIA	870 g·cm^{-2}	μ-underground	N_μ	[122]/N
BLANCA	W 112.8 N 40.2	Č. -light	X_{max}	[119]/N
DICE		2 imag. Č. -telesc.	X_{max}	[114]/N
HEGRA	La Palma (Canary Isl.)	Scint. array	N_e	[123]/N
AIROBICC	790 g·cm^{-2} W 17.9 N 28.8	Č. -light CRT	X_{max} Part. tracking	[115]/N [116]
MSU	Moscow, Russia 1000 g·cm^{-2}	Scint. array μ-underground	N_e μ	[117]/N [118]
EAS-TOP	Gran Sasso, Italy 810 g·cm^{-2}	Scint. array h-μ-calorimeter	N_e N_μ, h	[61]/N
MACRO	Undergr. 3100m w.e. E 13.6 N 42.4	μ-Tracking ($E_\mu > 13$ TeV)	Multi-μ	[136]/N
AKENO	Akeno, Japan 920 g·cm^{-2} E 138.5 N 35.8	Scint. array μ-counter Č. -counter	N_e N_μ X_{max}	[45]/N [138]
KASCADE	Karlsruhe, Germany 1020 g·cm^{-2} E 8.4 N 49.0	Scint. array LST-tunnel Calorimeter MWPC, LST, Scint.	N_e, N_μ μ-Tracking N_h, E_h N_μ, ρ_μ μ-Arrival times	[60]/Y [139] [111] [113]
KASCADE-Grande		Scint. array	N_{ch}	[38]/Y
MAKET-ANI	Mt Aragats, Armenia	Scint. array	N_e	[107]/N
GAMMA	700 g·cm^{-2} E 45.2 N 41.2	Scint. array	N_e, N_{mu}	[108]/Y

TIBET ASγ	Yanbajing, China	Scint. array	N_e	[109]/Y
ARGO	606 g·cm^{-2} E 90.5 N 30.1	RPC-carpet μ-Multiplicity	N_{ch}	[110]/Y
Haverah Park	Yorkshire, UK 1020 g·cm^{-2}	Water Č. -array	N_e, rise times	[30]/N
Grex/cover-plastex	W 1.6 N 56.0	RPC stack	Arrival times	[31]/N
AGASA	Akeno, Japan 920 g·cm^{-2} E 138.5 N 35.8	Scint. array	N_{ch}	[105]/N
Yakutsk	Russia 1020 g·cm^{-2} E 129.4 N 61.7	Scint. array Č. -light μ-underground	N_e,N_μ X_{max}	[106]/Y
Fly's Eye	Dugway, Utah, US 870 g·cm^{-2} W 112.8 N 40.2	FD-telescope	Fluor. light	[102]/N
HiRes Fly's Eye	Dugway, Utah, US 870 g·cm^{-2} W 112.8 N 40.2	FD-telescopes	Fluor. light	[103]/N
AUGER	Argentina 875 g·cm^{-2} W 69.3 S 35.5	Water Č. -array FD-telescopes	N_{ch} Fluor. light	[54]/Y [55]
NORIKURA	Japan, 740 g·cm^{-2} E 137.3 N 36.1	Scint. array	N_e	[124]/N
GRAPES III	Ooty, India 600 g·cm^{-2}	Scint. array Prop. counters	N_e N_μ	[125]/Y
SPASE VULCAN	Southpole 650 g·cm^{-2}	Scint. array Č. -light	N_e X_{max}	[126]/N
Tien-Shan	Kyrgyzstan 690 g·cm^{-2}	Scint. array Č. -light	N_e X_{max}	[127]/Y
L3+C	CERN, Switzerland 1000 g·cm^{-2} E 6.01 N 46.15	Scint. array μ-tracking ($E_\mu > 15$ GeV)	N_e μ-Multip., Eμ	[128]/N
Tunka 133	Russia, 950 g·cm^{-2} E 103 N 51.5	Č. -light	X_{max}	[129]/Y
BAKSAN	Russia, 833 g·cm^{-2}	Scint. array	N_e	[130]/Y
BUST	E 42.7 N 43.4	Undergr. array	Muons	[131]/Y
Mt Chacaltaya BASJE	Bolivia, 540 g·cm^{-2} W 68.2 S 16.4	Emulsion Ch. Scint. array	h + γ N_e	[132]/N

PAMIR	Tadjikistan 600 g·cm^{-2}	Emulsion Ch.	TeV h + e/γ	[133]/Y
Mt. Kanbala	Japan 520 g·cm^{-2}	Emulsion Ch.	TeV h + e/γ	[134]/N
Mt. Fuji	Japan 650 g·cm^{-2}	Emulsion Ch.	TeV h + e/γ	[135]/N

Table A.1: List of EAS experiments and their relevant characteristics.

Appendix B

Toy Monte-Carlo details

This sub-section presents the input file for the toy Monte Carlo program that has been used for this investigation. The parameters of the input file are explained thus giving the reader an idea of the toy simulation features.

Number of events (LDDs to be generated)
(indicates how many events will be simulated)
1000
Use constant level of noise for all stations (0) or variable (1)?
(indicates whether the random fluctuations that are added to the stations are of equal amplitude or are variable with a maximum possible value)
1
Maximum level of noise to densities in % [0-100]
(the maximum amplitude of the simulated noise in %)
30
Minimum number of stations with information [1-37]
(it is possible here to tell the program to only generate events that have a specified minimum number of active stations)
20
Rule used for excluding stations: randomly (0) or at large distances(1)
(one can decide here that silent stations are placed at random radial ranges or predominantly at large radial ranges)
1
Shower core generation boundaries xmin, xmax, ymin, ymax in KASCADE coordinates
(all events will be generated with shower cores inside the specified limits)
-500 0 -550 50
Radial range used for fitting [m]
(this is to select the radial range used for fitting the lateral density distribution that was generated according to the above options)
200 700
Create LDD histograms? (Y=1, N=0)
(this option tells the program whether to create histograms of the generated lateral density distributions - for visual inspection purposes)
0

Alpha min, max (<2) *(NFMIN, NFSTART, NFMAX, NFSTEP)*
(this option - and the following two - specify the intervals from which the Linsley parameters are randomly selected when generating lateral density distributions)
0.5 1.999
Eta min, max (>2)
2.001 10.
N parameter min, max
0.00001 1E+12
N data for fit initialization
(NFMIN, NFSTART, NFMAX, NFSTEP)
(this option - and the following two - specify the minimum and maximum allowed values for the Linsley fit parameters, their starting value and step size in the minimization routine)
0.00001 1E+8 1E+20 5.0
ALPHA data for fit initialization
(ALPHAFMIN, ALPHAFSTART, ALPHAFMAX, ALPHAFSTEP)
0.5 1.15 1.99999 0.03
ETA data for fit initialization
(ETAFMIN, ETAFSTART, ETAFMAX, ETAFSTEP)
2.0001 4.0 10. 0.03

Appendix C

SHOWREC variable flow

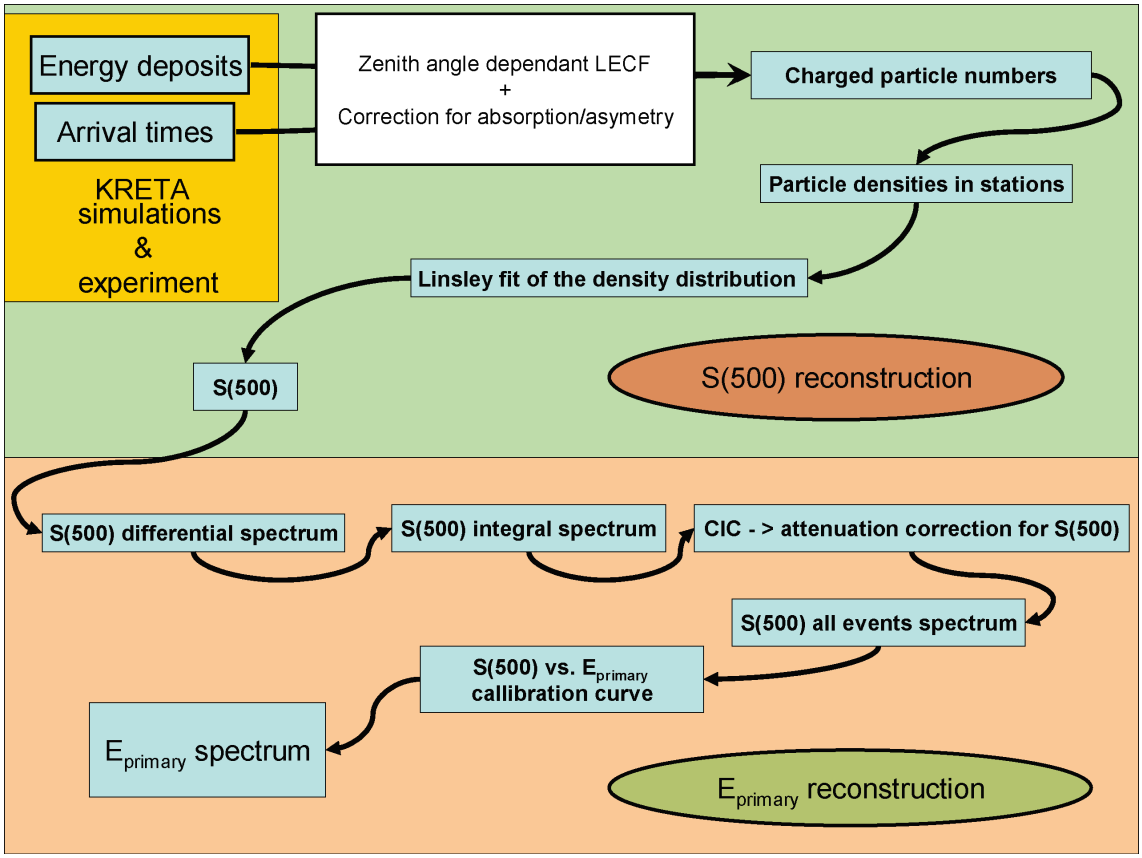

Figure C.1: Reconstruction chain in SHOWREC.

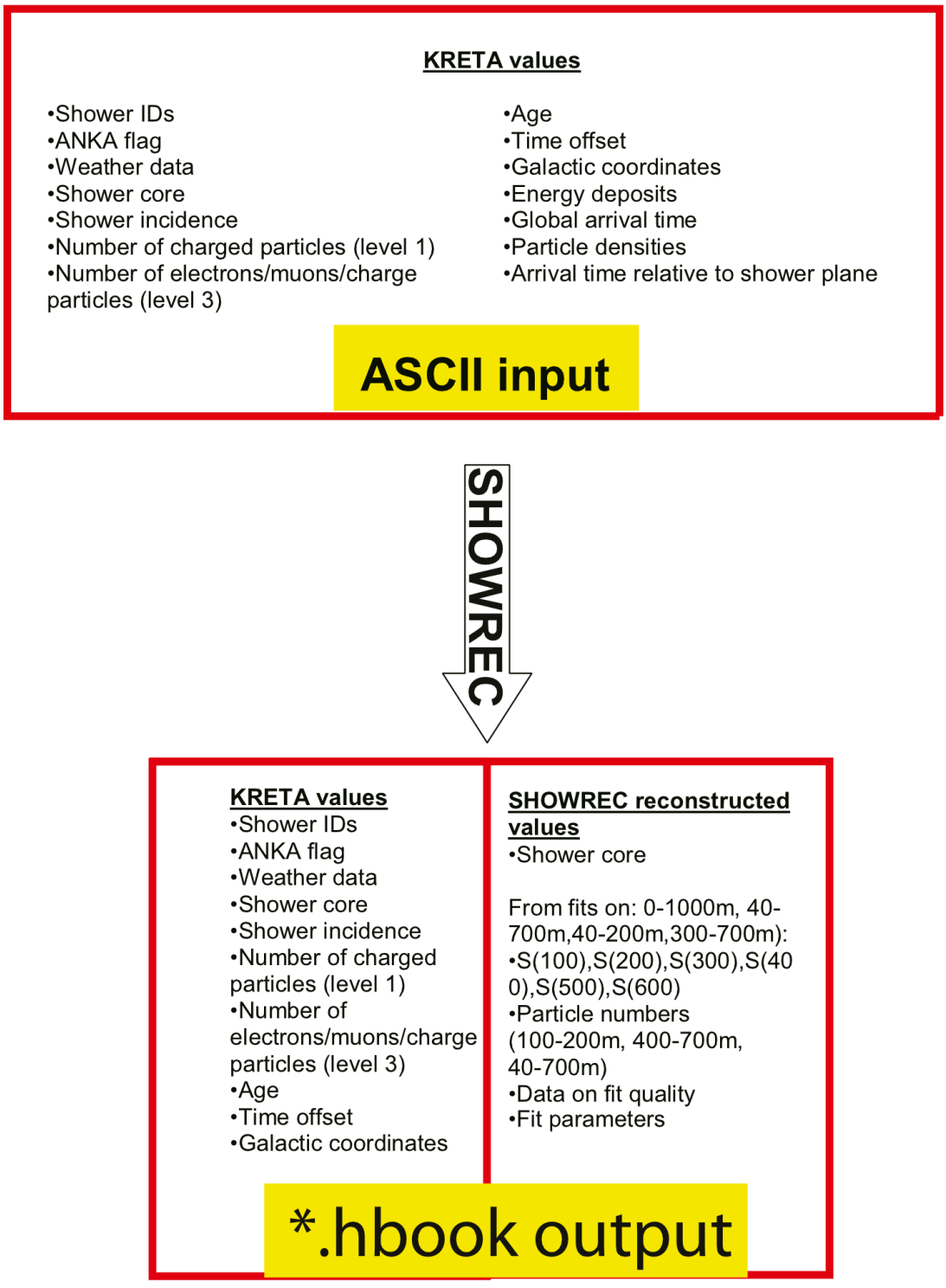

Figure C.2: Variable flow in SHOWREC.

Appendix D

Reconstruction quality test for various LDF forms

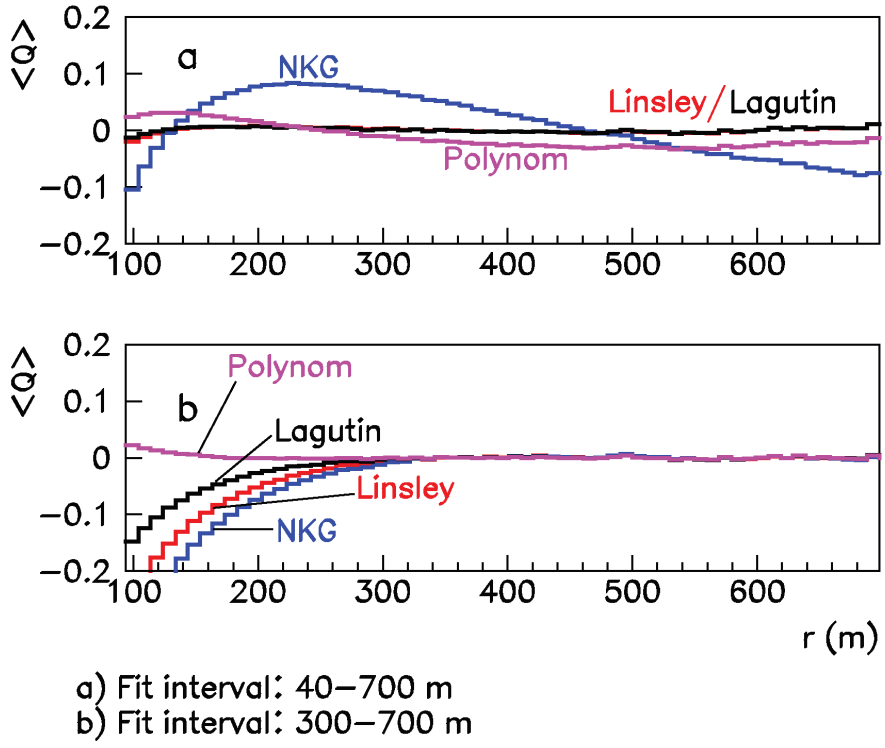

Figure D.1: Comparison of the reproduction of the average CORSIKA lateral charged particle distribution by various forms of the LDF (case: proton induced EAS of (1.0-1.78)·10^{17} eV).

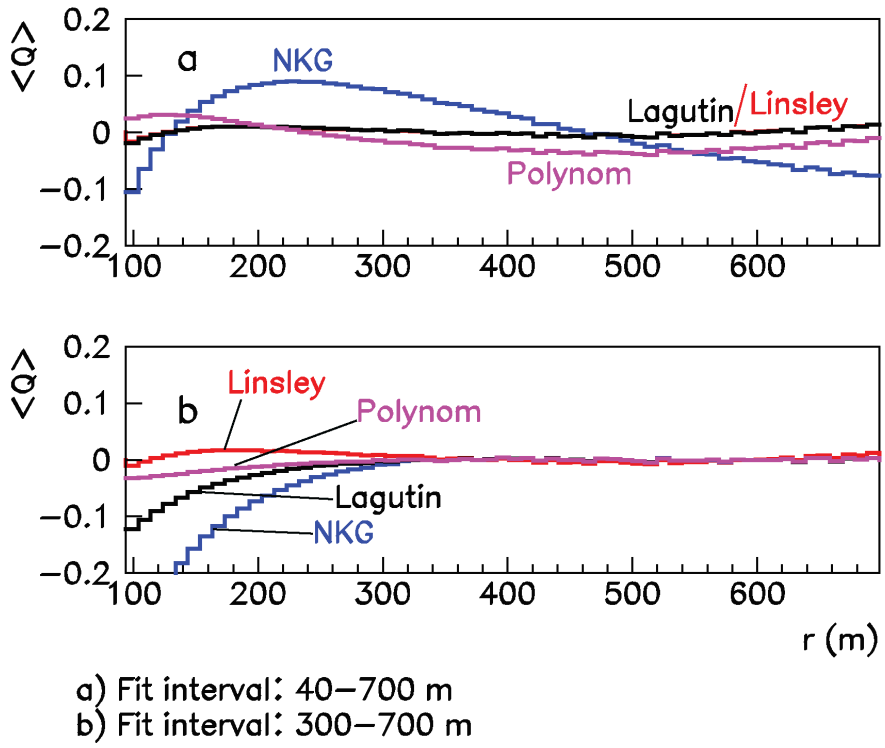

Figure D.2: Comparison of the reproduction of the average CORSIKA lateral charged particle distribution by various forms of the LDF (case: carbon induced EAS of (1.0-1.78)·10^{17} eV).

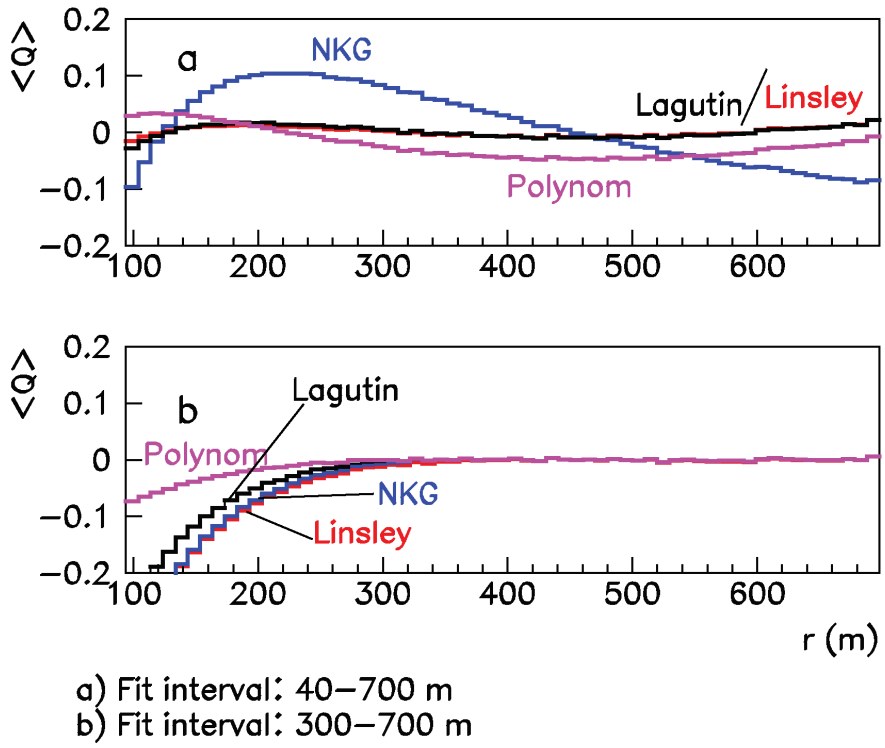

Figure D.3: Comparison of the reproduction of the average CORSIKA lateral charged particle distribution by various forms of the LDF (case: iron induced EAS of (1.0-1.78)·10^{17} eV).

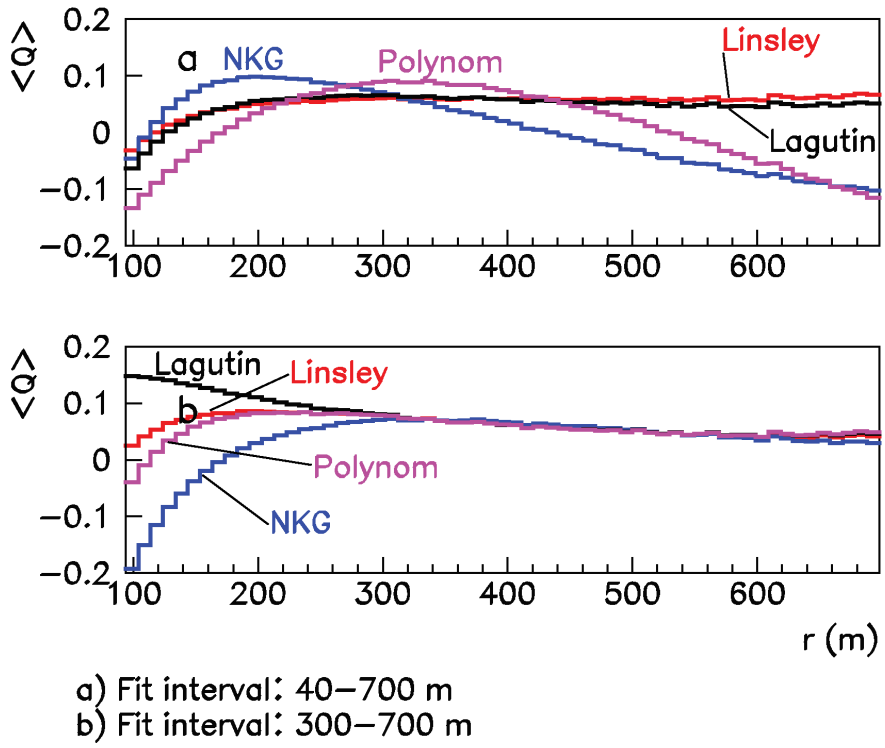

Figure D.4: Comparison of the reproduction of the average reconstructed lateral charged particle distribution by various forms of the LDF (case : proton induced EAS of (1.0-1.78)·10^{17} eV).

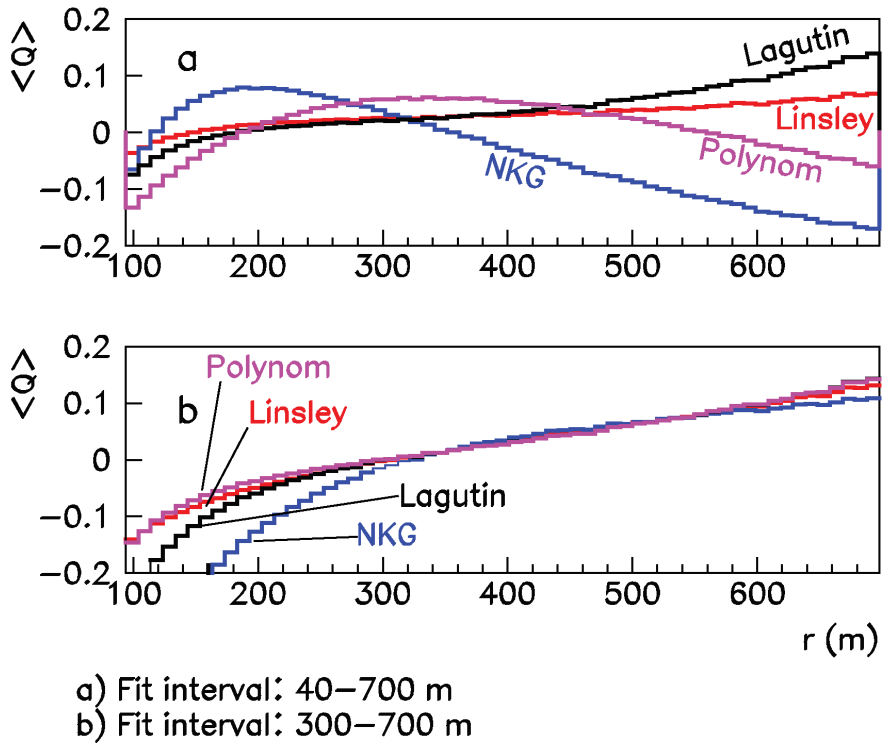

Figure D.5: Comparison of the reproduction of the average reconstructed lateral charged particle distribution by various forms of the LDF (case : carbon induced EAS of (1.0-1.78)·10^{17} eV).

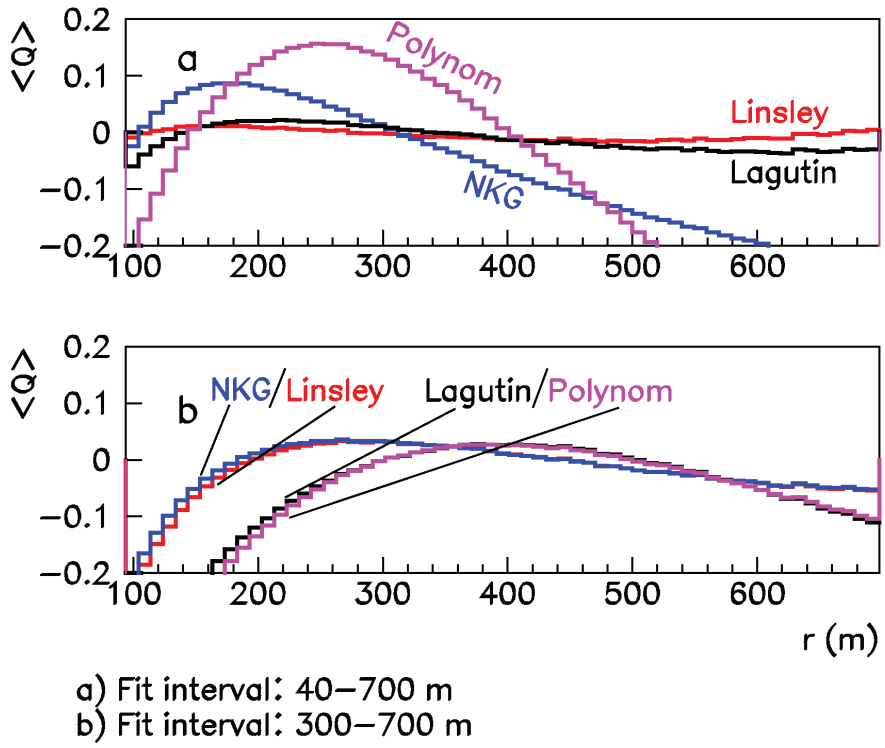

Figure D.6: Comparison of the reproduction of the average reconstructed lateral charged particle distribution by various forms of the LDF (case : iron induced EAS of (1.0-1.78)·10^{17} eV).

Appendix E

Shower fluctuations

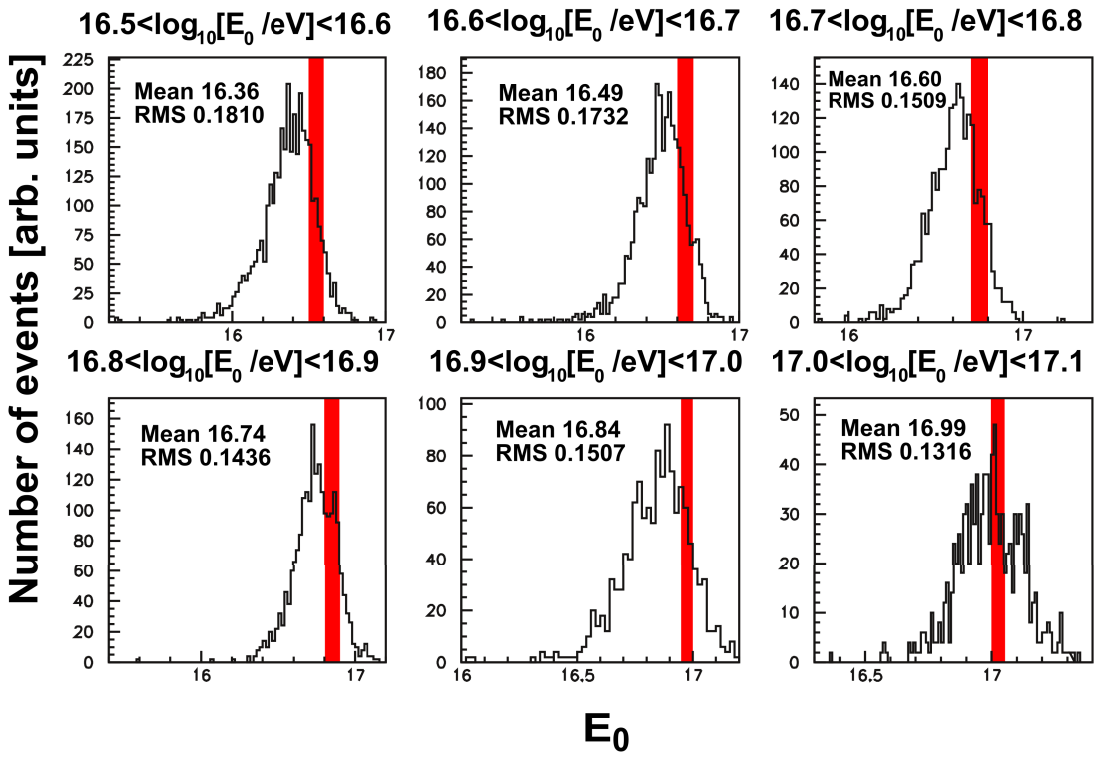

Figure E.1: The distribution of reconstructed primary energy (simulations) for events having their true energy distributed in narrow bins in the $\log_{10}[E_0/eV] \in$[16.5,17.1] range.

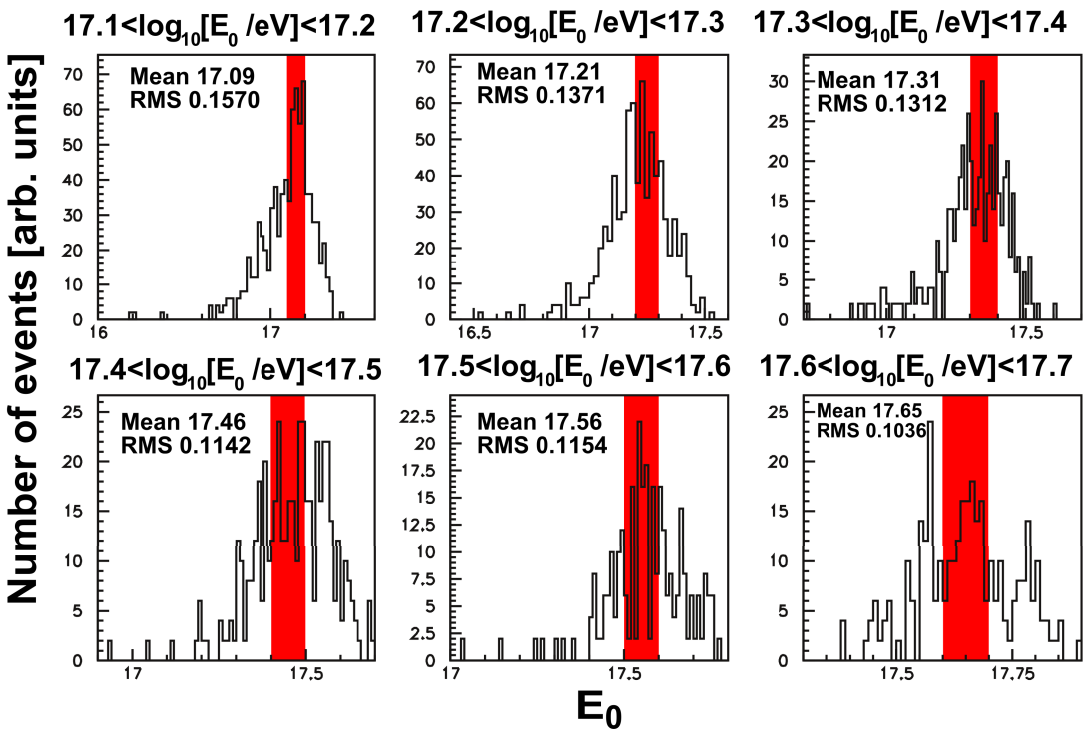

Figure E.2: The distribution of reconstructed primary energy (simulations) for events having their true energy distributed in narrow bins in the $\log_{10}[E_0/eV] \in$[17.1,17.7] range.

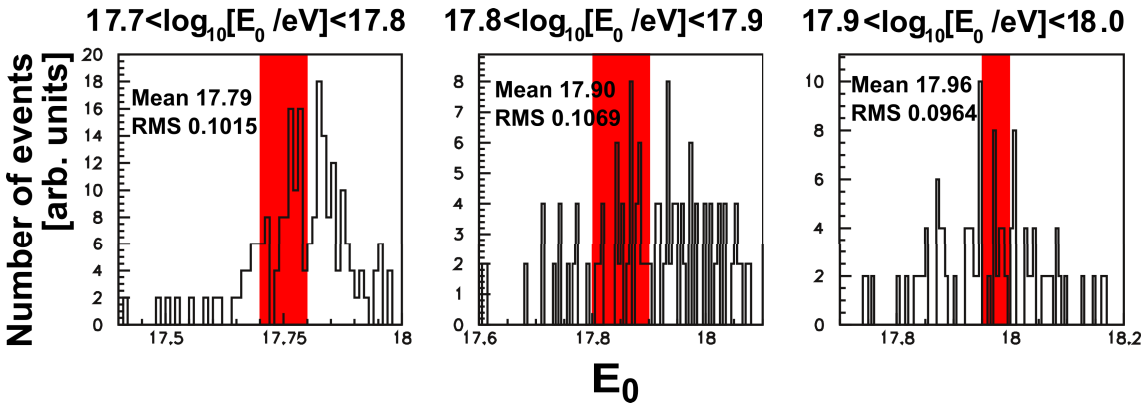

Figure E.3: The distribution of reconstructed primary energy (simulations) for events having their true energy distributed in narrow bins in the $\log_{10}[E_0/eV] \in$[17.7,18.0] range.

Appendix F

The attenuation of EAS observables

When extensive air showers travel through the Earth's atmosphere at various angles of incidence they are attenuated differently, according to the corresponding atmospheric track length. A more inclined shower will reach the detector in a more attenuated state than a less inclined one (a direct comparison of events is of course possible only if we assume that the primary particle (E_0,A) was the same in both cases and the first interaction occurred at similar atmospheric heights). The effect is visible when plotting the spectra of observables for different zenith angular bins (assuming that we perform a normalization of the spectra to area, time and solid angle).

An investigation has been performed on both simulated and experimental events in order to evaluate the attenuation length of various EAS observables of interest. Thus the attenuation of electrons and muons was evaluated from simulated studies (separately for each component). Next, the attenuation of S(500) was evaluated from both simulated and experimental studies. The results are presented below.

The investigation of simulated events shows that the attenuation length of the muon component is much larger than that of the electron component. This is obvious since the electrons are getting absorbed much faster than the muons. Simulations showed also that the attenuation length of S(500) is between the values of muons and electrons. This is because the S(500) exhibits mixed features of both muon and electron components. Also the comparison between simulation-derived S(500) attenuation lengths and experimentally derived values show acceptable agreement.

- Electrons

The electron size was evaluated only from simulations. The electron size was plotted (fig. F.1) as a function of the zenith angle for various primary energy thresholds and for various energy bins. The profiles of these plots were fitted with the attenuation formula described in chapter 5.

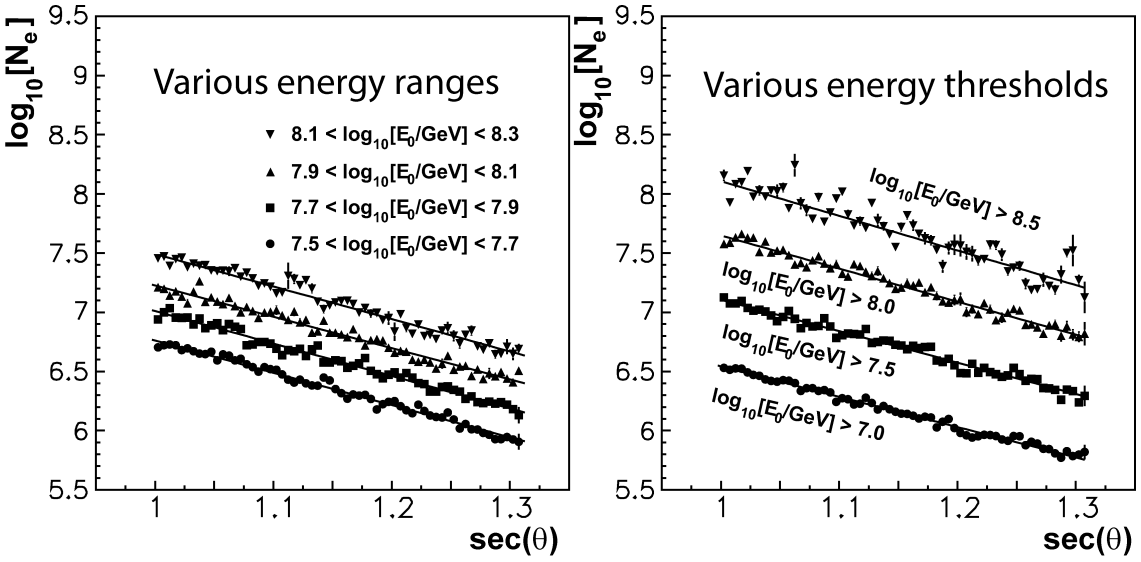

Figure F.1: Attenuation of the electron size N_e for various primary energies (simulations, all primaries).

$\log_{10}[E_0/\mathrm{GeV}]$	$\lambda_{N_e} \pm \sigma_\lambda$ [g· cm^{-2}]	$\log_{10}[E_0/\mathrm{GeV}]$	$\lambda_{N_e} \pm \sigma_\lambda$ [g· cm^{-2}]
>7.0	399±3	[7.5,7.7]	375±2
>7.5	385±3	[7.7,7.9]	373±3
>8.0	366±4	[7.9,8.1]	387±4
>8.5	349±4	[8.1,8.3]	372±4

Table F.1: The attenuation of N_e (simulations, all primaries; these values result from the fits presented in plot F.1).

- Muons

The muon size was evaluated only from simulations. The muon size was plotted (fig. F.2) as a function of the zenith angle for various primary energy thresholds and for various energy bins. The profiles of these plots were fitted with the attenuation formula described in chapter 5.

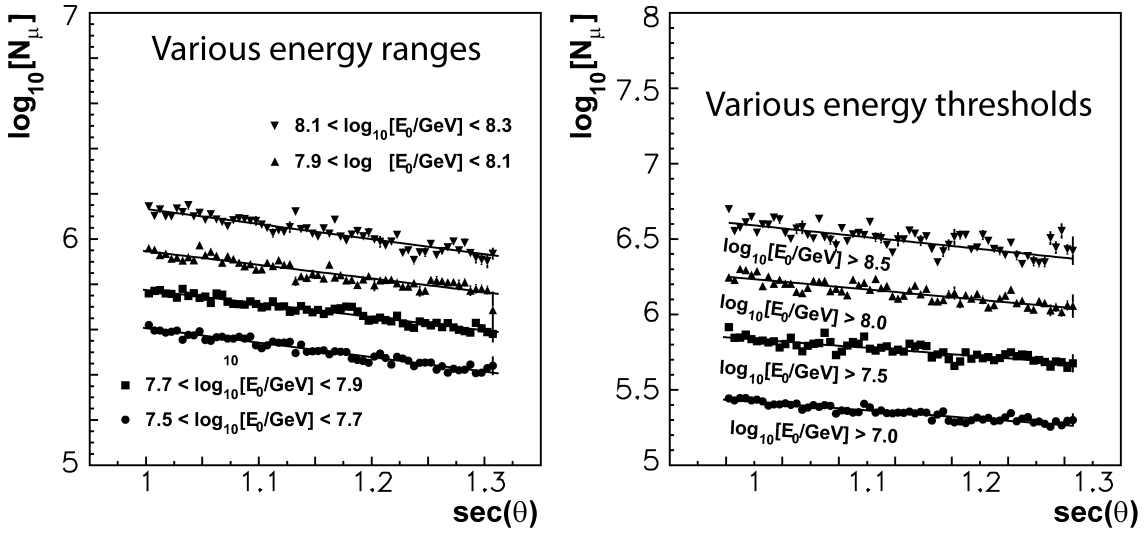

Figure F.2: Attenuation of the electron size N_μ for various primary energies (simulations, all primaries).

$\log_{10}[E_0/\mathrm{GeV}]$	$\lambda_{N_\mu} \pm \sigma_\lambda$ [g· cm^{-2}]	$\log_{10}[E_0/\mathrm{GeV}]$	$\lambda_{N_\mu} \pm \sigma_\lambda$ [g· cm^{-2}]
>7.0	1831±36	[7.5,7.7]	1598±27
>7.5	1825±55	[7.7,7.9]	1722±33
>8.0	1499±51	[7.9,8.1]	1694±40
>8.5	1309±39	[8.1,8.3]	1534±31

Table F.2: The attenuation of N_μ (simulations, all primaries; these values result from the fits presented in plot F.2).

- S(500)

The attenuation of S(500) was evaluated from both simulations (similarly to the test presented above for N_μ and N_e) and experimental data (by employing the CIC method).

The experimental evaluation of $S(500)$ attenuation has been performed

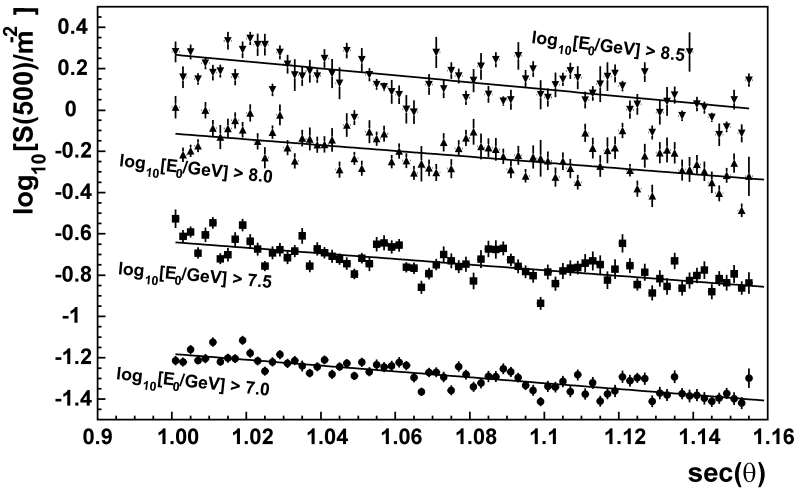

Figure F.3: Attenuation of the S(500) for various primary energy thresholds (simulations, all primaries).

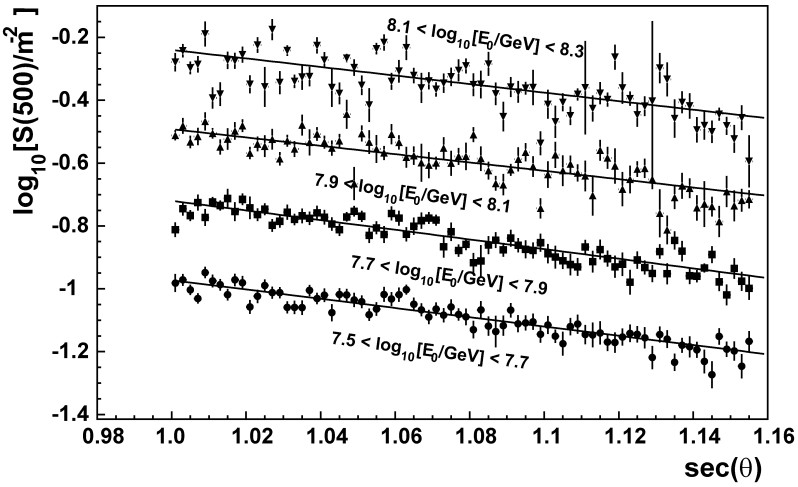

Figure F.4: Attenuation of the S(500) for various primary energy ranges (simulations, all primaries).

for various constant intensity cuts in the integral spectra of S(500) (for increasing zenith angular bins, as presented in chapter 5). Fig. F.5 presents these cuts.

$\log_{10}[E_0/\mathrm{GeV}]$	$\lambda_{S(500)} \pm \sigma_\lambda$ [g· cm^{-2}]	$\log_{10}[E_0/\mathrm{GeV}]$	$\lambda_{S(500)} \pm \sigma_\lambda$ [g· cm^{-2}]
>7.0	721±15	[7.5,7.7]	694±14
>7.5	750±23	[7.7,7.9]	666±13
>8.0	727±27	[7.9,8.1]	771±51
>8.5	606±17	[8.1,8.3]	752±21

Table F.3: The attenuation of $S(500)$ (simulations, all primaries; these values result from the fits presented in the plots F.3 and F.4).

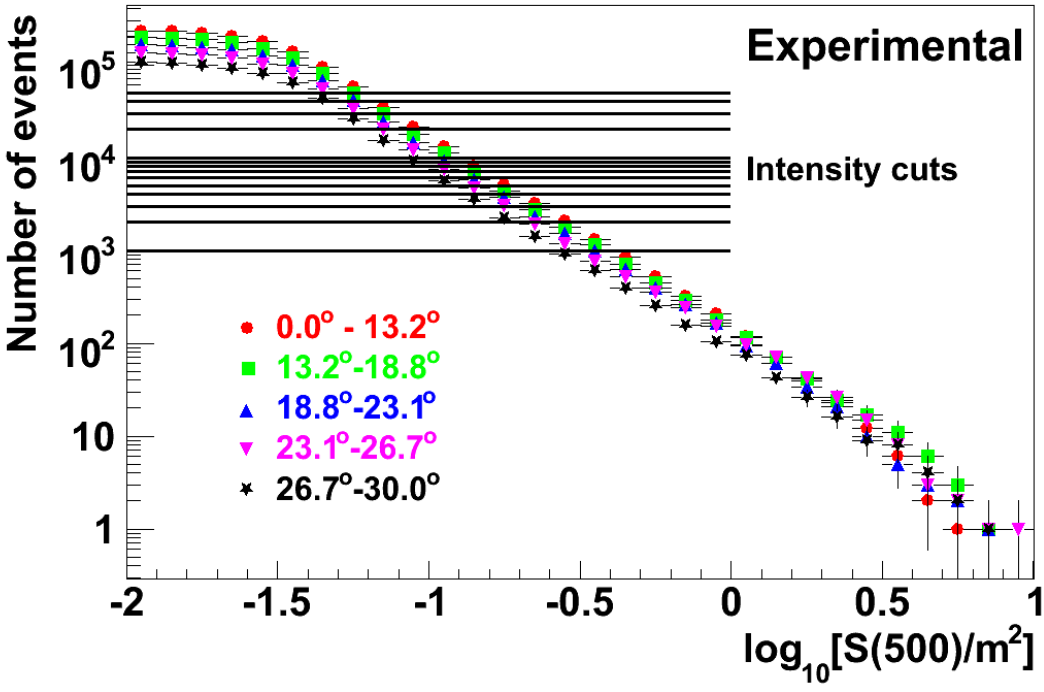

Figure F.5: Constant intensity cuts for which the S(500) attenuation length was evaluated (experimental data).

Intensity($\times 10^3$)	1	2	3	4	5	6	7
$\lambda_{S(500)}$[g$\cdot$ cm^{-2}]	704	708	732	729	729	731	737
$\sigma_{\lambda_{S(500)}}$[g$\cdot$ cm^{-2}]	22	22	25	27	25	29	26

Intensity($\times 10^3$)	8	9	10	20	30	40	50
$\lambda_{S(500)}$[g$\cdot$ cm^{-2}]	743	750	753	799	826	822	795
$\sigma_{\lambda_{S(500)}}$[g$\cdot$ cm^{-2}]	30	26	26	29	27	32	33

Table F.4: The attenuation of $S(500)$ (experimental data; these values result from the constant intensity cuts presented in the plot F.5).

Appendix G

The response matrix

This appendix presents the technique of building and then applying a response matrix in order to correct the effects of mis-reconstructions. We plan to evaluate the number of events migrating to wrong energy bins in the reconstructed energy spectrum and also to understand where this leak takes place. We build the dependency of true energy E_0^{true} as a function of the reconstructed energy E_0^{rec} as a 2-dimensional plot of cells (i,j) in which we set the bin size as in our reconstructed energy flux (with the total number of bins N_{bins}, figure G.1). In this plot (i,j) is the position of a cell with reconstructed energy E_0^{rec}(i) and true energy E_0^{true}(j). We then construct a matrix n(i,j) (i,j=$\overline{1, N_{bins}}$) in which the contents of the element (i,j) is the number of events stored in the corresponding cell (i,j) of the previously obtained plot (figure G.1). We then calculate the probability P(i,j) of having n(i,j) events with reconstructed energy E_0^{rec}(i) from a total N(j) events with true energy E_0^{true}(j) (that is the probability of reconstructing an event in bin i when its true energy is in bin j). Thus P(i,j) is given by equation G.1 and forms in fact our response matrix.

$$P(i,j) = \frac{n_{i,j}}{\sum_{i=1}^{N_{bins}} n_{i,j}} \tag{G.1}$$

The probabilities calculated at eq. G.1 do not depend on the spectrum which was used for obtaining them (apart of course from the statistical fluctuations). With the above calculated probabilities, the number of events with reconstructed energy in bin i is given by equation G.2. In this equation we add the contribution of all events with true energy $E^{true}(j)$ being reconstructed as $E^{rec}(i)$ (of course the summing is done over j, since j is counting the true energy bins). If equation G.2 describes the case of events with reconstructed energy in bin i, we could generalize the equation in order to describe all bins i=$\overline{1, N_{bins}}$ at the same time. Thus equation G.2 is converted to a matrix equation, G.3.

$$N^{rec}(i) = \sum_{j=1}^{N_{bins}} P(i,j) \cdot N^{true}(j) \tag{G.2}$$

$$N^{rec} = P \cdot N^{true} \tag{G.3}$$

where:
- N^{rec} and N^{true} are column matrices;

- P is the probability response matrix given by G.1.

In the case of the experimentally reconstructed spectrum we know the N^{rec} matrix (see equation G.3) and we also have the response matrix P from simulated studies. From equation G.3 we can calculate the N^{true} matrix (equation G.4).

$$N^{true} = P^{-1} \cdot N^{rec} \tag{G.4}$$

where:
- N^{rec} and N^{true} are matrices with the same significance as in equation G.3;
- P^{-1} is the inverse of the response matrix.

In order to facilitate the comparison between the results of this method and the results of other reconstructions (i.e. the reconstruction of primary energy from S(500) versus the reconstruction from other observables) a simplified procedure has been applied, in which the response matrix has not been inversed. Figure G.2 shows the result of applying the correction on the same simulation data from which the response matrix P is derived (as a consistency check). As expected, the reconstructed spectrum is corrected and brought to the form of the true spectrum. The statistical fluctuations in the true spectrum are induced also in the corrected spectrum. In order to avoid propagating such statistical fluctuations one should not apply the correction matrix directly on the experimental data (an additional "smoothing" of the matrix should be applied first).

A procedure to smooth the response matrix has been proposed. Thus, for a given bin i of reconstructed energy (X axis in figure G.1) we assume that the response matrix data inside that bin is distributed according to a Gaussian shape (in regard to the true energy, Y axis in figure G.1). As an example see the bin marked with a rectangle in figure G.1. We fit the data in several (relevant) such bins with a Gaussian function and plot the variation of the Gauss function parameters (most probable value (MPV), width and height) with the reconstructed energy (figures G.3-G.5). We parameterize their dependence with the reconstructed energy and then, based on the parameterized values we compute a new response matrix. The new matrix will resemble the original one (since it is derived from parameterizations of it), but will not be affected by statistical fluctuations inherent to event samples of restricted size (in effect, the new response matrix is a smooth image of the original one). A comparison between the original matrix and the smoothed one is presented in figure G.6.

Figure G.8 shows the result of applying the correction on the experimental spectrum(the corrected spectrum has slightly increased spectral index γ=3.22$\pm$0.18). Besides accounting for statistical fluctuations, the response matrix corrects also the tendency of underestimation for smaller energy events. This results in a noticeable increase in the corrected flux towards smaller energies (since the response matrix will account for events with underestimated energy). Figure G.9 shows the same flux multiplied with E_0^3. The error bars on the corrected spectrum result from the propagation of errors in the un-corrected spectrum and also from the errors in the energy matrix (the error associated to a cell (i,j) in the energy matrix -fig. G.1- is assumed equal to the square root of the value stored in that particular cell i.e. is given by a Poissonian law; similarly the error associated to an energy bin in the un-corrected spectrum is considered equal to the square root of the value stored in

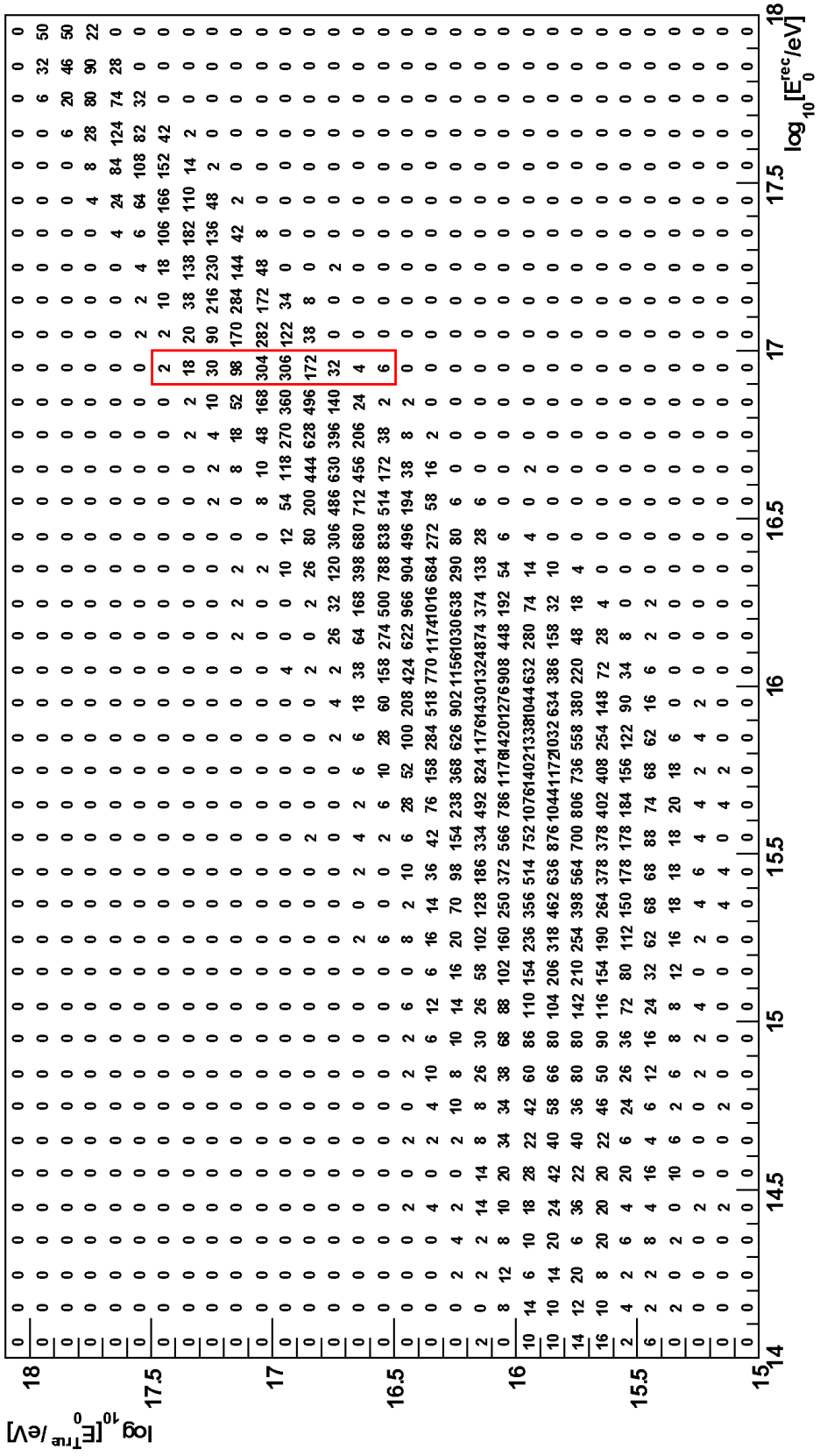

Figure G.1: Energy matrix (the precursor of the response matrix).

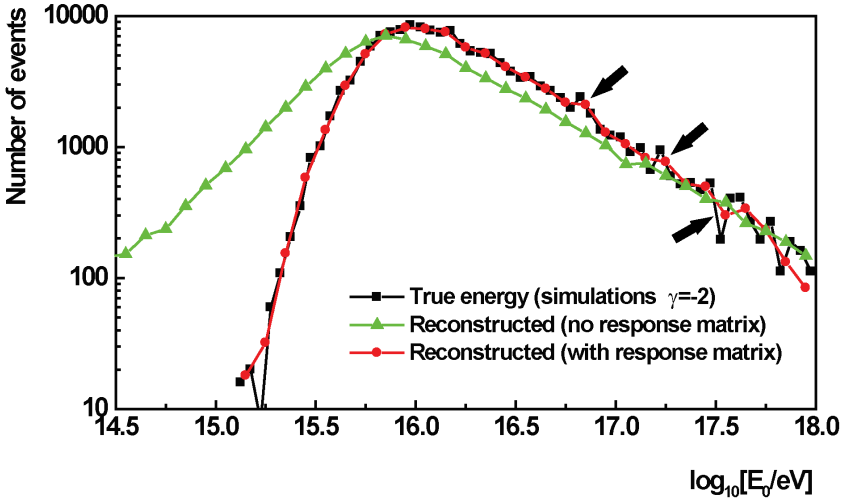

Figure G.2: Simulations: applying the response matrix correction on the reconstructed spectrum (gray triangles); the resulting corrected spectrum (filled circles) is almost identical to the true one (black squares), but contains fluctuations induced by the statistical fluctuations in the true spectrum (some cases are indicated by small arrows as examples).

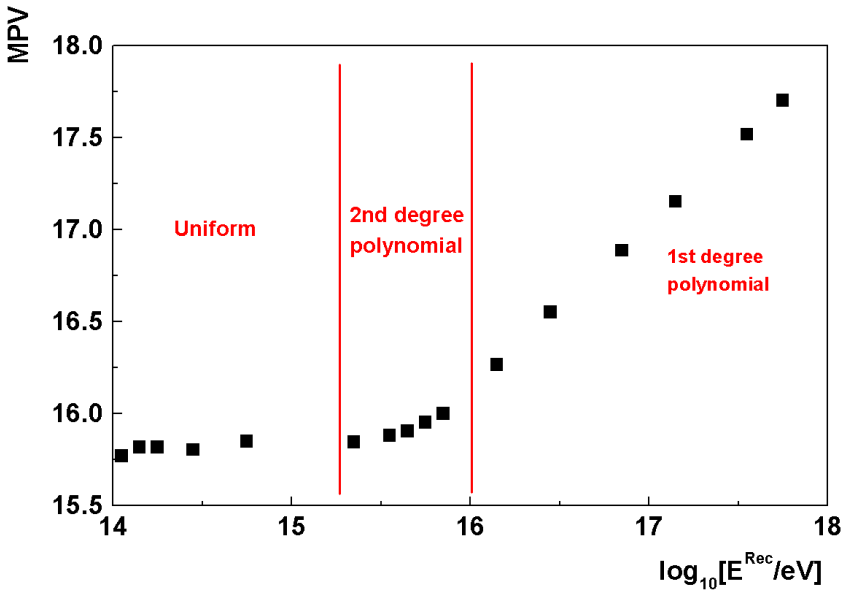

Figure G.3: Most probable value of the Gauss function when fitting response matrix data in various bins of reconstructed energy; three parameterizations were used to describe this variation, a uniform one, a second degree polynomial and a first degree polynomial in the ranges indicated on the plot.

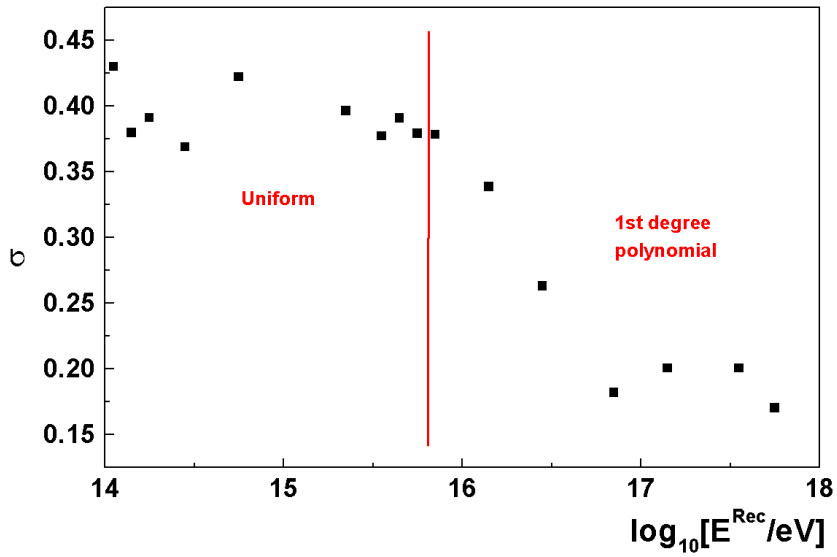

Figure G.4: Width of the Gauss function plotted against the reconstructed energy; two parameterizations were used to describe this variation, a uniform one and a first degree polynomial in the ranges indicated on the plot.

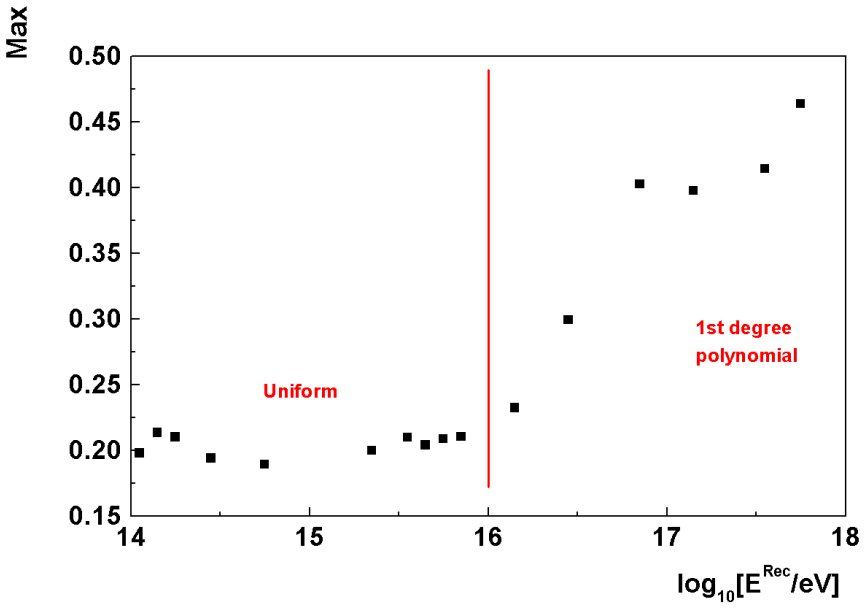

Figure G.5: Maximum of the Gauss function plotted against the reconstructed energy; two parameterizations were used to describe this variation, a uniform one and a first degree polynomial in the ranges indicated on the plot.

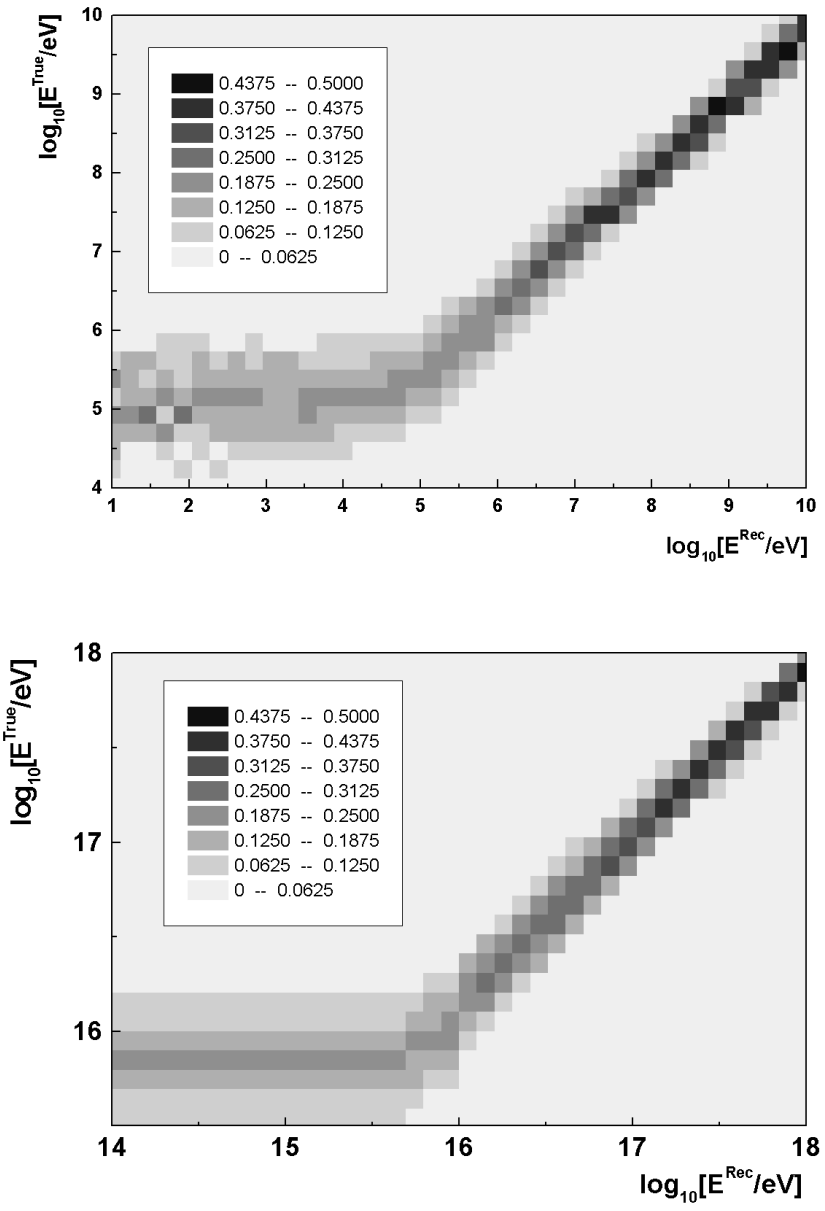

Figure G.6: The response matrix before the smoothing procedure (above) and the new smoothed response matrix (below).

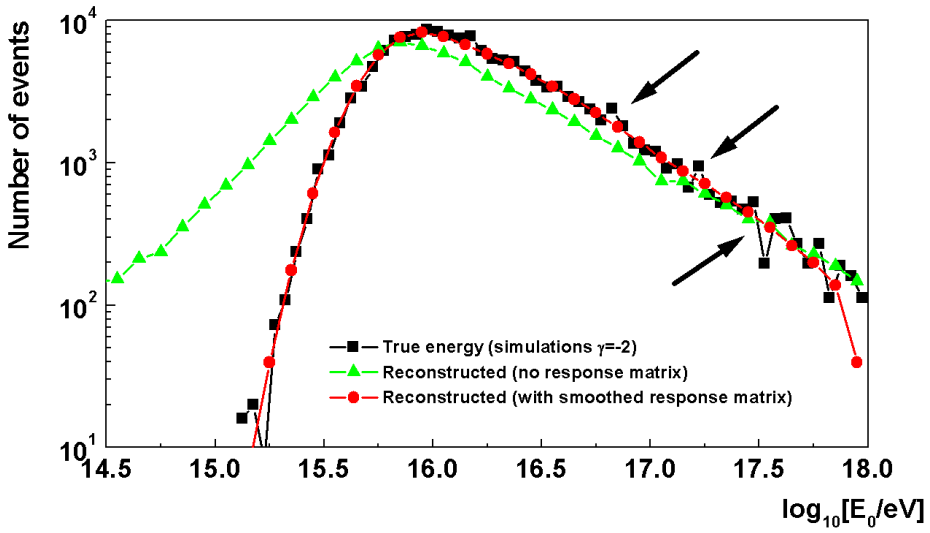

Figure G.7: Simulations: applying the smoothed response matrix on the reconstructed spectrum; the resulting corrected spectrum is no longer affected by the fluctuations.

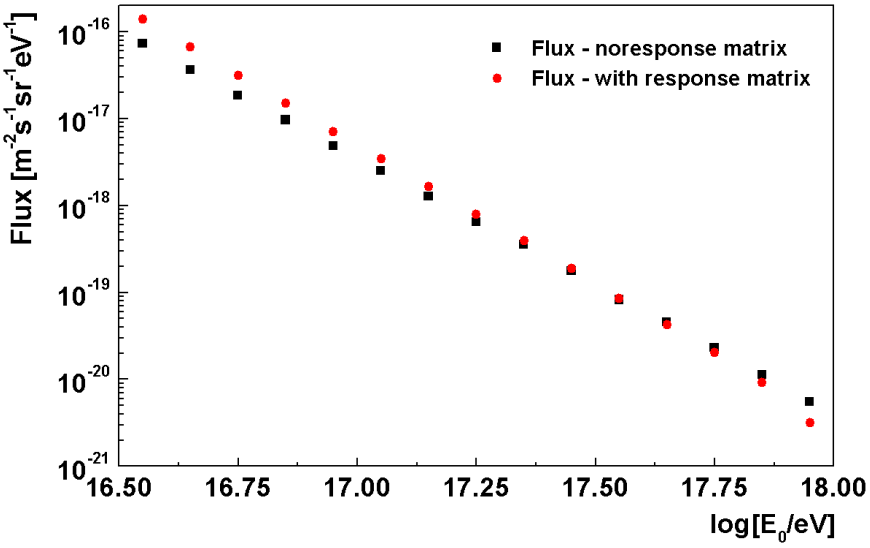

Figure G.8: Comparison between the energy flux obtained from the experimentally recorded S(500) (black squares) and the response matrix corrected flux (circles); a smoothed response matrix is employed.

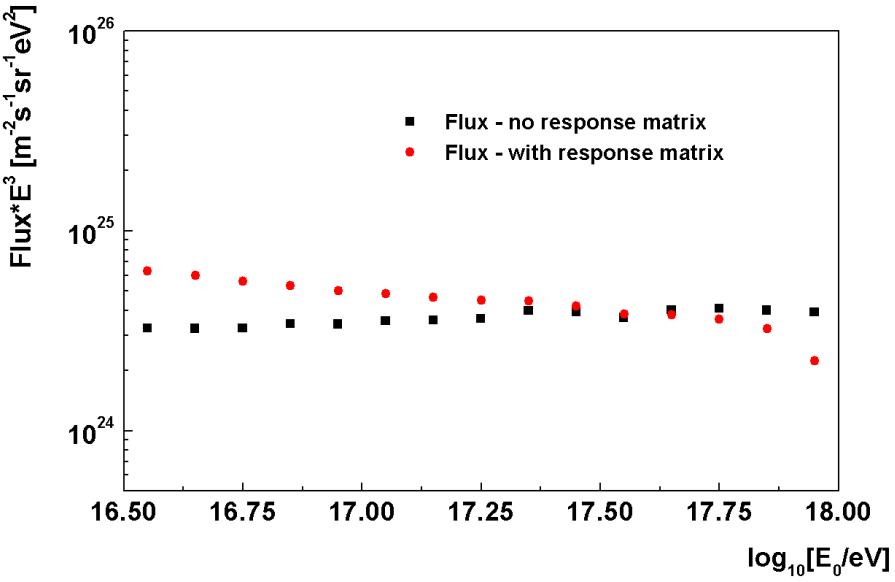

Figure G.9: This plot shows the same spectra in the previous plot (fig G.8) but multiplied with E^3.

that particular bin).

It is important to note that these results are only preliminary and there are several aspects of this correction technique that need further adjustments. For example, the sudden end of the simulated data sample at 10^{18} eV introduces undesired effects and therefore the correction is unreliable around this energy and above (see in figure G.7 the sudden drop of the corrected spectrum in the last energy bin).

List of Figures

List of Tables

ISSN 1869-9669